Technische Universität München

Max Planck-Institut für Biochemie

Abteilung für Molekulare Strukturbiologie

"Study of the archaeal motility system of *Halobacterium salinarum* by cryo-electron tomography"

Daniel Bollschweiler

Vollständiger Abdruck der von der Fakultät für Chemie der Technischen Universität München zur Erlangung des akademischen Grades eines Doktors der Naturwissenschaften genehmigten Dissertation.

Vorsitzender: Univ.-Prof. Dr. B. Reif

Prüfer der Dissertation:

1. Hon.-Prof. Dr. W. Baumeister

2. Univ.-Prof. Dr. S. Weinkauf

Die Dissertation wurde am 05.11.2015 bei der Technischen Universität München eingereicht und durch die Fakultät für Chemie am 08.12.2015 angenommen.

“REM AD TRIARIOS REDISSE”

- Roman proverb -

Table of contents

1. Summary 1
2. Introduction 3
2.1. *Halobacterium salinarum*: An archaeal model organism 3
2.1.1. Archaeal flagella 5
2.1.2. Gas vesicles 8
2.2. The challenges of high salt media and low dose tolerance in TEM 11
3. Materials and methods 16
3.1. Cell growth of *Halobacterium salinarum* 16
3.2. Cell cultures at lower NaCl concentrations 17
3.3. Swarm agar motility assays of *Halobacterium salinarum* 19
3.4. Vitrification of *Halobacterium salinarum* cells 19
3.5. Cryo-electron microscopic examination of *Halobacterium salinarum* 20
3.6. Focused ion beam milling of *Halobacterium salinarum* cells 20
3.7. IgY-labeling of halobacterial flagella 23
3.7.1. Production of polyclonal IgY antibodies against Fla protein 24
3.7.2. Fla-binding specificity of IgY under hypersaline conditions 26
3.8. Isolation of gas vesicles 28
3.8.1. Mass spectrometry of solubilized wild type gas vesicles 28
3.8.2. Vitrification of intact wild type vesicles 29
3.8.3. Vitrification of intact I34M point mutant gas vesicles 29
3.9. Transmission electron microscopy and dose tolerance of gas vesicles 30
3.10. Cryo-electron tomography 31
3.10.1. CET of isolated halobacterial gas vesicles 34
3.11. Operation of the Volta phase plate 36
3.12. Subtomogram analysis 38
4. Results 40
4.1. Cryo-electron tomographic study of *H. salinarum* polar caps 40
4.1.1. Preliminary cryo-EM studies 40
4.1.2. Swarm agar motility assays of *Halobacterium salinarum* 42
4.1.3. Salt concentration tolerance pretrials 43
4.1.4. Optimization of the cell vitrification process 49
4.1.5. Focused ion beam milling of vitrified cell samples 54
4.2. Localization of the flagellar growth site 57

4.3. Study of the gas vesicle substructure 60
4.3.1. Mass spectrometry of solubilized wild type gas vesicles 60
4.3.2. Optimization of parameters for gas vesicle vitrification 66
4.3.3. Electron dose tolerance of gas vesicles 69
4.3.4. Cryo-electron tomography of isolated gas vesicles 73
4.3.5. Tomographic reconstruction and analysis of the gas vesicle helicity 75
4.3.6. Subtomogram analysis of the gas vesicle structure 77
4.3.6.1. Constrained template matching 79
4.3.6.2. Subvolume extraction 81
4.3.6.3. Initial subvolume averaging 83
4.3.6.4. Fine alignment and classification 84
4.3.7. Docking models of GvpA 92
5. Discussion 97
5.1. Cryo-electron tomography of cells under hypersaline sample conditions 97
5.2. IgY labeling of the flagellar growth site 99
5.3. The structure of the gas vesicle and the molecular arrangement of GvpA 100
6. Acknowledgements 105
7. References 107

1. Summary

Halobacterium salinarum, a chemo- and phototrophic halophilic archaeon of the phylum *Euryarchaeota* and an archaeal model organism, is frequently found in marine environments that reach salinities approaching the saturation limit of sodium chloride. The organism is actively motile and its distinct motility apparatus comprises the archaeal flagellar complex, rooted in a polar cap structure, and proteinaceous gas vesicles. Coupled to chemotactic and phototactic sensors, the rotating flagella propel the cell towards beneficial growth factors, such as nutrient sources, warm temperatures and moderate sunlight, and away from adverse conditions, such as pockets of low salt concentrations or intense UV radiation. In parallel, the highly regulated production and disassembly of gas vesicles controls the cell's buoyancy and thus helps regulate the swimming depth within its oxygen-starved hypersaline habitat.

Archaeal flagella, as well as gas vesicles, have been a subject of research for several decades and many questions remain as of yet unanswered.

Archaeal and bacterial flagella share the same function and a similar morphology. Nevertheless, the archaeal flagellum differs considerably from its well-characterized bacterial equivalent. Genetically, it is entirely unrelated and instead exhibits sequence similarities to the bacterial type IV secretion system. Indeed, it has been proposed to designate the archaeal flagellum the "archaellum", in order to emphasize its status as a unique motility structure**.** Recent studies lead to a schematic assembly model of the different flagellin components for *Crenarchaeota*; however, the structural details of the archaeal flagellum, in particular the motor complex, have yet to be solved.

Gas vesicles are found in a handful of species throughout the two prokaryotic domains. They are entirely proteinaceous, with two identified structural proteins, GvpA and GvpC, in addition to twelve Gvp proteins involved in regulation and assembly. However, vesicle synthesis and degradation still eludes mechanistic understanding. Several *in-silico* structural model predictions for GvpA, the main structural protein, exist. They are aided by observations made in X-ray diffraction, atomic force microscopy (AFM), and solid-state nuclear magnetic resonance (NMR) studies. Nevertheless, no three-dimensional structure of molecular resolution is available at this time.

The aim of this work is to lay out an experimental approach to gain novel insights into the *in-situ* arrangement and molecular structure of the components of the archaeal motility system within the challenging hypersaline conditions of *H. salinarum*. Of particular interest are the flagellar anchoring complex, the flagellar basal bodies, and the main structure protein of the gas vesicles. Firstly, a focus was placed on the optimization of cell growth and sample preparation parameters for the

cryo-electron tomographic study of intact halobacterial cells. Furthermore, labeling assays with polyclonal IgY antibodies were designed, in order to potentially localize the flagellar growth site.

Only recent technological advances in the field of transmission electron microscopy (TEM) make it possible to tackle the considerable difficulties presented by the high intracellular salt concentrations of *H. salinarum*. The low signal-to-noise ratio of individual micrographs that would ordinarily ensue, was countered by thinning down vitrified cell samples via focused ion beam (FIB) milling, combined with the utilization of a direct electron detector and post-column energy filtering system for image recording. Finally, the application of a novel Volta phase plate – developed in-house – significantly boosts contrast formation at near focus level.

Isolated gas vesicles also possess a challenging characteristic in that they exhibit a distinctly reduced electron dose tolerance. To compensate for this trait, the combined use of state of the art equipment, such as direct electron detection, energy filtering, and the Volta phase plate, served as the prerequisite to record cryo-electron tomograms at doses about three times lower than biological samples typically allow for. In addition, the regular cylindrical regions of the gas vesicle envelope were analyzed by subtomogram averaging in order to resolve their building blocks on a molecular scale.

2. Introduction

2.1. *Halobacterium salinarum*: An archaeal model organism

Halobacterium salinarum is a rod-shaped halophilic extremophile measuring about 2 – 5 µm in length and 0.5 µm in diameter. Taxonomically, "Halobacterium" is a genus of the class *Halobacteria*: It belongs to the phylum *Euryarchaeota* within the domain of *Archaea*. *H. salinarum* is generally regarded as an archaeal model organism. Its strains are routinely and easily cultivable and have been subject of extensive study. Moreover, an array of molecular genetic tools have been developed and the halobacterial genome was first fully sequenced by Ng *et al*. in 2000 [1, 2]. The organism requires warm marine environments with salt concentrations in excess of 4 – 6 M NaCl to thrive – about seven to ten times that of regular sea water. Such concentrations are reached in salterns or hypersaline lakes such as the Dead Sea. In this oxygen-starved, extreme salinity very few other life forms are able to exist. *H. salinarum*, however, is well adapted and can grow to densities of over 10^8 cells/ml, staining its habitat purplish-red through its membrane-bound antioxidant bacterioruberin, as seen in *Figure 1* [1].

Figure 1. *Photo of a hypersaline lake in Namibia. Halobacteria, as shown in the light microscopy image (circle), thrive in this environment: The water is stained reddish-pink by the cells' purple membranes and the membraneous carotenoid bacterioruberin, an antioxidant radiation protectant. Photo by Karsten Kotte, University of Heidelberg.*

Halobacterium possesses three major metabolic pathways to maintain sufficient supplies of ATP under different environmental conditions. Chemotrophically, it is capable of aerobic and anaerobic respiration via the tricarboxylic acid (TCA) cycle. Ordinarily, oxygen acts as the final electron acceptor. Under oxygen deprivation the cell relies on energetically less favorable substitute electron acceptors such as nitrate, dimethyl sulfoxide or fumarate [3, 4]. Under light exposure, the phototrophic pathway predominates. The membrane-bound photo receptor bacteriorhodopsin, a light-driven, outward-facing proton pump creates an electrochemical potential by exporting H^+. The resulting proton gradient drives ATPases to produce ATP. Engaged under low light conditions in anaerobic environments, a third pathway enables substrate-level phosphorylation through the fermentation of L-arginine. Here, arginine is oxidized to citrulline via the arginine deiminase pathway [5]. In turn, citrulline reacts with inorganic phosphate to form ornithine and carbamoyl phosphate, catalyzed by ornithine transcarbamylase. Finally, the transferase carbamate kinase coordinates the hydrolysis of carbamoyl phosphate into NH_3 and CO_2 and phosphorylates ADP to ATP.

In order to survive in high salt halophiles generally employ one of two major adaption strategies: Many mesophilic halotolerant species rely on low-molecular organic compatible osmolytes, such as proline, ectoine, glycerol, arabitol or glycin betaine [6]. Generally, they are uncharged or zwitterionic and soluble in high concentrations, where they do not inhibit normal protein function while countering cellular osmotic stress. Nevertheless, these compounds must either be synthesized directly within the cell or have to be imported, which is energetically expensive. The second, more dedicated strategy is the formation of a modified proteome, adapted to correctly fold at very high intracellular salt concentrations. Halobacteria apply this “salt-in” strategy; their proteome comprises a high amount of acidic amino acids. Specifically, outward-facing moieties exhibit a notably increased number of aspartate and glutamate, and a reduced occurrence of the basic lysine. The result is an increased electrostatic surface potential of the folded proteins, amplifying their hydrophilicity [7]. This adaption mechanism prevents salting out of the proteins in extreme salt concentrations at the price of being *exclusively* adapted to these environments. At lower salt concentrations, halophilic proteins often cease to function or even denature. For example, at medium conditions under 2 M NaCl or with the removal of Mg^{2+}, which stabilizes the cells’ S-layer, lead to immediate lysis of halobacterial cells [8].

Notably, instead of compensating osmotic pressure directly with NaCl, *H. salinarum* maintains a very high intracellular KCl concentration. This is achieved through the active removal of Na^+ against the membrane potential via a bacteriorhodopsin-powered Na^+:H^+ antiport in combination with a K^+ uniport. In addition, a second retinal-containing protein, halorhodopsin, functions as a light-gated ion pump. It concurrently takes up K^+ and Cl^- ions, counterbalancing the external osmotic pressure of NaCl. Simultaneously, it sustains a considerable concentration gradient against the sparse extracellular K^+. Charging and preservation of this electrochemical gradient doubles as an emergency “potassium

battery" [9]: In the darkness, the flow of K^+ reverses. While K^+ is flowing out, Na^+ is now imported resulting in the concomitant efflux of H^+ via the Na^+:H^+ antiport. This ensures a steady proton gradient to drive the ATPase-mediated phosphorylation of ADP. In contrast to halotolerant organisms, the halobacterial life cycle and physiology requires and depends on high salt concentrations. *Halobacterium salinarum* is therefore characterized as extremely halophilic.

2.1.1. Archaeal flagella

Halobacteria, as well as other archaea, are actively motile by flagella. At first glance, archaeal and bacterial flagella are functionally and morphologically similar; both provide swimming motility to the cell through the rotation of these tail-like appendages. However, archaeal flagella differ distinctly from their more intensely studied bacterial counterparts in several key properties.

At a diameter of 10 – 15 nm the archaeal filaments are significantly thinner than those of bacteria, with a typical diameter of around 20 nm [10]. They exhibit a unique three-start helical symmetry and lack an inner flagellin translocation channel [11, 12]. Characteristically, between two and six different flagellin proteins constitute the main structural component of the archaeal flagellum, with very few exceptions [11]. Each of these building blocks has a highly conserved hydrophobic N-terminus, shared throughout the archaeal domain. Furthermore, they undergo two posttranslational modifications: Leader peptide cleavage and N-glycosylation. Flagellins are initially expressed as preproteins with a short, positively charged leader peptide that is cleaved off by a signal peptidase, termed the prepilin peptidase FlaK. The proteins then undergo N-linked glycosylation where, for *Halobacterium salinarum*, a linear, partially sulfated oligosaccharide of the type Asn-Glc1-4GlcA1-4GlcA1-(GlcA or 4Glc) is covalently attached. Interestingly, this glycosylation occurs extracellularly [13-15].

These findings suggest that biosynthesis of the archaeal flagellum must be decidedly different from that of the bacterial flagellar superstructure, which grows distally by routing a single type of flagellin through its inner 2 nm wide channel [16]. Genetically, the archaeal flagellum is unrelated to its bacterial equivalent, instead exhibiting homology with the bacterial type IV secretion system [11, 17]. However, the function of bacterial type IV pili is one of surface adhesion and translocation described as "twitching motility" [18]; pili are extended, adhere to a surface and retract, pulling the bacterium across. Archaea, on the other hand, produce rotatable flagella used for active swimming propulsion. For this, archaeal flagella rely on direct hydrolysis of ATP [19], whereas in bacteria flagellar rotation depends on the build-up of a proton gradient. *Figure 2* illustrates the currently proposed model of the archaeal flagellum by Albers *et al*. for *Crenarchaeota* [20]. Note that there are a few differences in the flagellar assembly between *Euryarchaeota* and *Crenarchaeota*. *Euryarchaeota* lack the scaffolding

protein FlaX, while *Crenarchaeota* do not seem to possess a submembranous polar cap structure found in some *Euryarchaeota*.

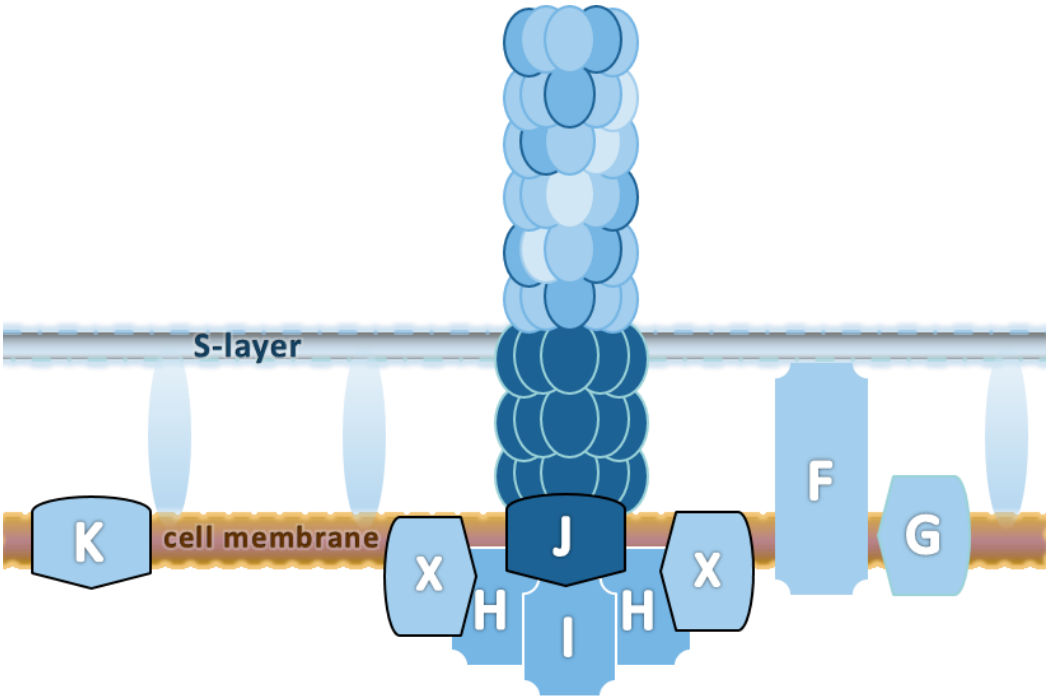

Figure 2. *Current model of the archaeal flagellum of Crenarchaeota. The FlaA and FlaB preproteins are cleaved by FlaK before they assemble into the filament (blue ellipsoids) through the motor complex. FlaX, a ring-forming scaffolding protein, does not exist in Euryarchaeota, such as H. salinarum. It allows for FlaH and FlaI to interact with the integral membrane protein FlaJ. FlaF and FlaG are thought to be involved in anchoring the flagellar complex. Modified from [20].*

During the early growth stages *Halobacterium salinarum* develops a flagellar bundle consisting of around five to ten individual flagella on one cell pole; towards the stationary phase most cells are bipolarly flagellated [21]. These bundles form a right-hand helix and comprise between five and ten flagella. A motor switch cycle coordinates changes in the synchronized rotational direction of the bundle, which maintains its helical shape without disentangling. Clockwise rotation propels the cell forward, while counter-clockwise movement puts it in reverse. Without any further external sensatory input the rotational direction switches approximately every 10 s [22]. In between movement phases the flagellar bundles remain motionless for a short time. During this pause state, the cell tumbles due to the effects of Brownian motion, randomizing its directional orientation. However, chemotactic and phototactic stimuli modify the motor switch cycle [23]. If positive stimuli are detected, such as orange light or nutrients, cycle switching is suppressed and movement continues without changing direction.

Negative stimuli shorten the switch cycle duration, favoring undirected movement. This movement pattern is described as a biased random walk.

The halobacterial flagellum consists of five different filament-forming flagellins. They are distributed on a larger locus of essential *fla*-associated genes and encoded in tandem amongst two operons, flaB1-3 and flaA1-2. All of them show extraordinary sequence similarity: They are between 193 – 196 amino acids in length at a calculated mass of 20.5 kDa, with the exception of three short hyper-variability regions per flagellin. Together, they form a long, helically arranged filament of 10 nm in diameter which is tethered to a short, curved hook-like structure, connecting the flagellum to the anchoring complex. The main filament component seems to primarily consist of A-type flagellins, whereas the hook and base region appears to be made up of the B-type, predominantly flaB2 [24]. Archaea seem to lack the distinct rings structures commonly observed on bacterial basal bodies [25]. Therefore, the molecular structure, assembly mechanism, and exact function of the anchoring complex as well as the roles and the identification of some of the individual anchoring protein components have yet to be solved. Notably, *Halobacterium salinarum* possesses a cytosolic polar cap structure, situated about 20 nm underneath the cytoplasmic membrane at the pole region [26]. Observation and isolation of this structure proved quite difficult, with only two groups having published successful attempts so far [26, 27]. The cap structure has been observed exclusively in a few other *Euryarchaeota*, namely *Natronomonas pharaonis*, and *Natrialba magadii*, both haloalkaliphilic extremophiles of the same genus *Halobacteriaceae* [27]. It spans across several hundred nanometers and may function as an inner membranous anchor region, rooting the proximal ends of the flagella and likely harboring the flagellar motor complex. It may therefore serve as the structural basis of the rotational synchronization of a bundle's individual flagella.

Through experimental observations, two of the unique features of archaeal flagella are to be examined more closely. The cryo-electron tomographic study of the pole regions of vitrified halobacterial cells could provide insights into the intracellular arrangement of the polar cap organelles and the distribution and structure of the flagellar basal bodies without drastically impairing morphological integrity. Additionally, antibody labeling assays with polyclonal fla-affine IgY should indicate a proximal or distal localization of the flagellar growth site, assisting in the understanding of the biosynthesis of archaeal flagella.

2.1.2. Gas vesicles

Gas vesicles are the second major component of the halobacterial motility apparatus. Generally, gas vesicles are air-filled compartments found across several species of cyanobacteria, some heterotrophic bacteria and halobacteria [28]. They provide buoyancy to the cell and enable it to vertically migrate to more favorable growth conditions. In transmission electron microscopy, young vesicles can be observed as small bicones of 10 – 20 nm in diameter. Mature vesicles grow to spindles or cylinders with conical tips with a diameter of 60 – 200 nm and a length of up to 1.5 µm. The gas-permeable vesicle envelope is entirely proteinaceous. Depending on species, between 8 – 14 Gvp proteins are involved in vesicle biogenesis. Early studies on gas vesicles have been primarily conducted on cyanobacteria, such as *Anabaena flos-aquae*, but Gvp proteins were soon found to share a remarkably high inter-species sequence homology [29-31].

In *Halobacterium salinarum* a total of 14 *gvp* genes contribute to the biosynthesis of gas vesicles (see *Figure 3*). They are separated in two directionally opposed clusters, *gvpDEFGHIJKLM* upstream and *gvpACNO* downstream. In addition, some halobacterial strains carry two complete sets of gvp genes on two separate chromosomes. For strain PHH1 these are termed p-vac, located on the endogenous plasmid pHH1, and c-vac, located on a mini chromosome. p-vac contains four promoters and produces spindle-shaped vesicles while c-vac expression, driven by two promoters, leads to a cylinder-shaped phenotype [28]. For strain NRC-1 a nearly identical distribution exists as gvp1, equivalent to p-vac, and gvp2, equivalent to c-vac. Here, the two regions are found on mini chromosomes pNRC100 and pNRC200, respectively.

Figure 3. *Schematic of the two halobacterial gene clusters, gvpDEFGHIJKLM, and gvpACNO, coding for gas vesicle synthesis. GvpA (red), as well as genes indicated in shades of blue are found throughout all gas vesicle-producing species. The two clusters have opposed transcription directions from a common origin, as indicated by the blue arrows. Modified from [28].*

The main structural component is GvpA, a small 8.3 kDa protein which forms the vesicle envelope. It arranges into characteristic helical ribs with a low pitch of 4.6 nm [28, 32]. The primary structure of GvpA is shown in *Figure 4* for the p-vac and c-vac protein, together with a secondary structure

prediction model by Strunk *et al.* [33]. A second structural protein, GvpC, provides support by attaching itself to the exterior surface of this wall [34, 35]. So far, further structural gas vesicle proteins have not been identified. The gas vesicle wall is freely permeable to gases, such as O_2, N_2, and CO_2, but also to the polar CO and to octafluorocyclobutane (C_4F_8) [36]. C_4F_8 has a molecular collision diameter of 6.3 Å. This is more than twice the size of a water molecule (2.75 Å), proving pores within the envelope are large enough to allow water to pass [37, 38]. However, water does not accumulate in the gas-filled vesicle interior. The current hypothesis is that the vesicle wall features an extremely hydrophobic interior surface, preventing nucleation of polar substances. Secondary structure predictions strongly imply a coil–α-helix–β-strand–β-strand–α-helix-coil folding motif with anti-parallel hydrophobic β-strands [33]. This is corroborated by infrared spectroscopic observations and solid-state NMR studies of intact collapsed gas vesicles from *Anabaena flos-aquae* [39, 40]. Moreover, the NMR data was used to compute a structural model in a simulated air–water interface. This model suggests an amyloid cross-β structure, in which antiparallel, inequivalent monomers interact to form the hydrophobic backbone of the helical ribs [40]. While the orientation of the two predicted α-helices is not taken into account, the β-strands are aligned at an angle of 36° relative to the cylinder axis. This appears to be in good agreement with previously conducted X-ray diffraction and atomic force microscopy (AFM) experiments [41, 42]. Finally, trypsin digestion of intact vesicles coupled with subsequent matrix assisted laser desorption ionization time-of-flight mass spectrometry (MALDI-TOF MS) of the cleaved peptides indicates the C-terminal α-helical region to face outward, whereas the β-strands were inaccessible to the enzyme [43]. However, so far the exact molecular structure and arrangement of GvpA within the vesicle envelope remains unresolved.

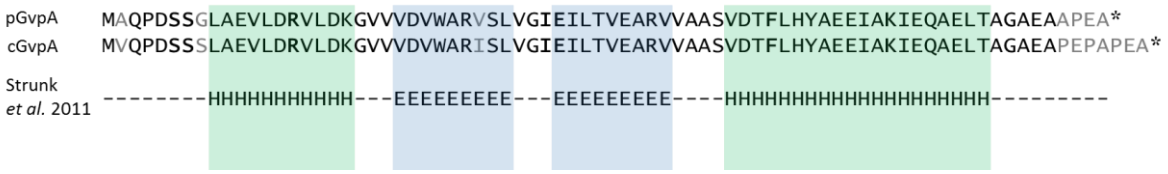

Figure 4. *Primary structures of halobacterial p-vac and c-vac GvpA. A secondary structure model by Strunk et al. predicts the formation of α-helices ("H", green label) and β-strands ("E", blue label) [33, 44]. The center region around these β-strands is highly conserved. Modified from [33].*

A high performance *de novo* computational model prediction of halobacterial GvpA by Strunk *et al.* suggests an anti-parallel alignment of the β-strands as well as a likely dimerization of GvpA [33]. Here, the inward-facing β-strands form a concave, strongly hydrophobic surface. For this structural model, point mutations of potential contact regions between monomers were tested. Any point mutation of

the N-terminal α_2-helical region prevented the assembly of gas vesicles entirely, indicating this region to be important for the successful assembly of the vesicle. Strunk *et al.* also reported that point mutations of the β-turn at amino acid positions 34 and 35 respectively resulted in particularly long and thin cylindrical vesicle phenotypes [33].

A second *in silico* model by Ezzeldin *et al.* predicts a similar amphiphilic topology, with anti-parallel hydrophobic β-strands on one side opposite to the hydrophilic α-helices [45]. Simulated AFM images from this model imply that the previously observed 36° tilt of β-strands may have been misinterpreted. Instead, the α-helices are tilted, with each N-terminal α_2-helix forming an interaction site between two anti-parallel neighboring monomers. The two referenced computational models are compared in *Figure 5*.

In general, no sequence homologues of GvpA outside gas vesicles have so far been found in nature [33]. This makes structural prediction models difficult to validate. Moreover, experimental structural analyses of the protein have been exceedingly difficult due its strong tendency to aggregate. 80 % formic acid is required to fully dissolve GvpA, preventing many biochemical standard assays, such as SDS-PAGE or enzymatic digestion experiments. In this context, cryo-electron tomography, coupled with subtomogram analysis, provides a unique opportunity to directly observe the structural organization of intact, isolated gas vesicles in life-like condition and cast light on the molecular arrangement of the vesicle envelope.

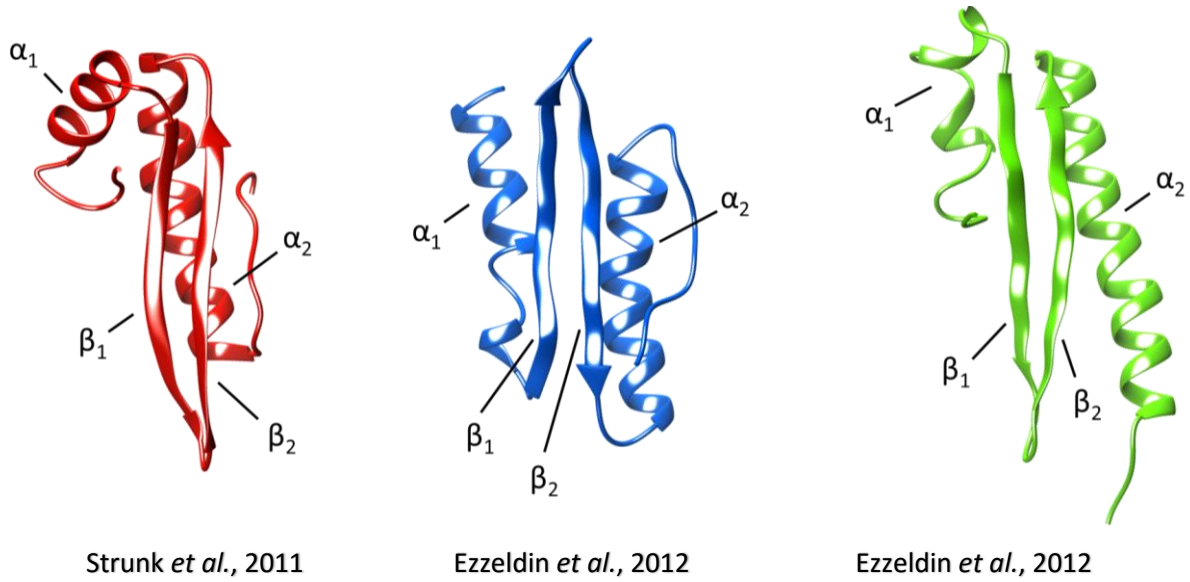

Figure 5. *De novo prediction models for the structure of GvpA. Left side: Strunk et al. proposed a central hydrophobic anti-parallel ß-strand (ß1 and ß2) shielded by two hydrophilic α-helices (α1 and α2) [33]. They also suggest a strong tendency for GvpA to dimerize, with two tilted ß-strands forming a concave*

inward-facing hydrophobic surface. Their model was derived from mcGvpA of Haloferax mediterranei, which is nearly sequence-identical to halobacterial GvpA. Middle and right side: The two top-ranking energy models found by Ezzeldin et al. for the folding of GvpA from Halobacterium salinarum [45]. Both models agree with the α-β-β-α secondary structure motif found in other studies and predict a very similar amphiphilic surface separation but differ in the arrangement of their quaternary structure, in which the β-strands are perpendicularly arranged to the helical pitch direction of the gas vesicle.

2.2. The challenges of high salt media and low dose tolerance in TEM

The generally encountered salt concentrations of several mol/l pose a serious challenge for transmission electron microscopic imaging of *H. salinarum* under cryo conditions. Firstly, the additional high numbers of negatively charged Na^+ (formed from ^{23}Na) and Cl^- ions (of the stable isotopes ^{35}Cl and ^{37}Cl) increase the amount of inelastic and elastic electron scattering. This decreases the signal-to-noise ratio (SNR) of the image. Since halobacteria replace Na^+ intracellularly by equimolar concentrations of heavier K^+ ions (mostly formed from the main isotope ^{39}K) this effect is further amplified. Secondly, saline medium densities range from 1.18 g/cm^3 for 3.0 M $NaCl_{aq}$ over 1.25 g/cm^3 for 4.3 M $NaCl_{aq}$ to 1.32 g/cm³ for 4.3 M KCl_{aq} (intracellularly). This is very close to the average protein density of 1.35 g/cm^3 and leads to a notable attenuation of contrast [46].

A negative staining procedure of biological material with a reagent of very high atomic density, such as uranyl acetate, could potentially counteract these effects. It would lead to higher amplitude contrast formation and an increased dose tolerance of the fixated specimen. However, this preparation method is not able to stain intracellular components of whole cells. The imaging of semi-attached polar caps by negative staining is potentially possibly, and has been conducted successfully by Kireev *et al*., but it requires the precursory lysis of the cell [27]. Any remaining cellular shells (“ghosts”) are morphologically compromised, preventing the observation of intracellular components in an *in-vivo*-like state. In contrast, imaging of intact halobacterial pole regions via cryo-electron tomography should provide better insights into the *in-situ* structural arrangement of this organelle and the proximal parts of the archaeal flagellum.

Imaging of gas vesicles presents a different adverse property. Vitrified vesicles exhibited an increased electron dose sensitivity (see 3.9), as their rib structure visibly decomposed at electron doses as low as 30 – 40 e/Å² during the recording of image series in the context of this work. With such a significantly limited total electron dose to be distributed over the entirety of a tomographic tilt series, the SNR of each individual tilt becomes accordingly low. This denotes a challenge for the investigation of the structure of gas vesicles, which are composed of 8.3 kDa proteins as building blocks.

A number of solutions exist to alleviate the challenges imposed by the effects of a high salt environment for full cell tomography and limited electron dose for the tomographic recording of isolated gas vesicles.

For the cells, it is initially imperative to remove as much salt from the medium as possible, without damaging their morphology. Due to the halophilic nature of these extremophiles, complete removal of NaCl is not an option, as this destroys the cells. Experiments are necessary to determine the minimum salt concentration for intact, motile *H. salinarum* cells (see 4.1.3). Furthermore, sample vitrification has to be optimized: The resulting layer of vitreous ice must not be too thick, to prevent excessive electron scattering, nor too thin, so that the encased cells would not be deformed by compression.

As the vitreous ice would necessarily have to encase whole, undeformed cells, a thickness of 500 nm or more is unavoidable. This is a daunting value, especially in combination with the hypersaline halobacterial cytoplasm. Imaging of intracellular components would only be possible through thinning the specimen. Therefore, focused ion beam (FIB) milling technology should be employed to cut wedge-shaped cavities into the sample (see 4.1.5).

For the tomographic recording of both, full cells and isolated gas vesicles, the utilization of an energy filter becomes indispensable to further increase contrast in high-salt conditions. Furthermore, two recent technological advancements substantially aid to boost SNR and contrast formation respectively:

A direct electron detector can be employed to further improve image quality. While complementary metal-oxide-semiconductor (CMOS) technology is not new, the development of highly radiation-resistant direct electron detectors that are adequately thin to drastically reduce backscattering events came to fruition only very recently. In contrast to older charge-coupled devices (CCD), a CMOS-based detector is able to read out the signal created by even a single electron directly. This renders the need for a scintillator, which converts the incoming electron into a number of photons, redundant (see *Figure 6*). Accordingly, direct electron detectors offer a more defined point spread function (PSF) and greatly increase the SNR. The latest generation of direct electron detection cameras, such as the Gatan *K2 Summit*, is able to record at very high framerates of up to 400 frames per second. The high temporal resolution allows for the computational alignment and averaging of individually recorded sub-frames, thus compensating for mechanical or radiation-induced drift of the object. This is particularly advantageous for the precise recording of the gas vesicle substructure, as a single GvpA dimer must measure less than or equal to 4.6 nm (see 2.1.2).

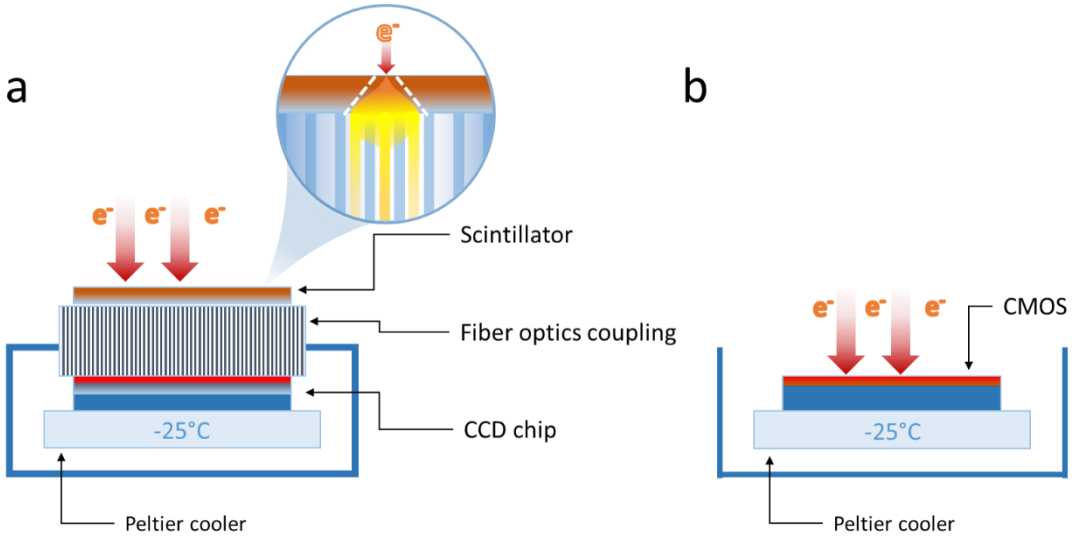

Figure 6. *Schemes of a CCD detector (a) and a CMOS-based direct electron detector (b). The CCD-based type needs to turn incoming electrons into a cloud of photons in a multi-stage conversion via a scintillator coupled to fiber optics. The delocalization causes the PSF to diffuse. The CMOS-based type is able to record the incoming electrons directly, without any intermediate signal conversion. Modified from FEI [47].*

Finally, a newly developed Volta phase plate (VPP) permits image recording of unstained cryo-samples very close to focus and with high contrast [48]. The VPP is a thin, continuous carbon film, situated at the back-focal plane of the objective lens. Here, the central diffraction beam induces a Volta potential. After an initial settling time this localized potential causes the phase of unscattered incident electrons to shift by approximately $\frac{\pi}{2}$ [48]. Consequently, phase contrast formation is boosted significantly for very low spatial frequencies: The CTF's sine is turned into a cosine function. Three contrast transfer function models at different defoci are displayed in *Figure 7* illustrating the effects of focus and the phase plate.

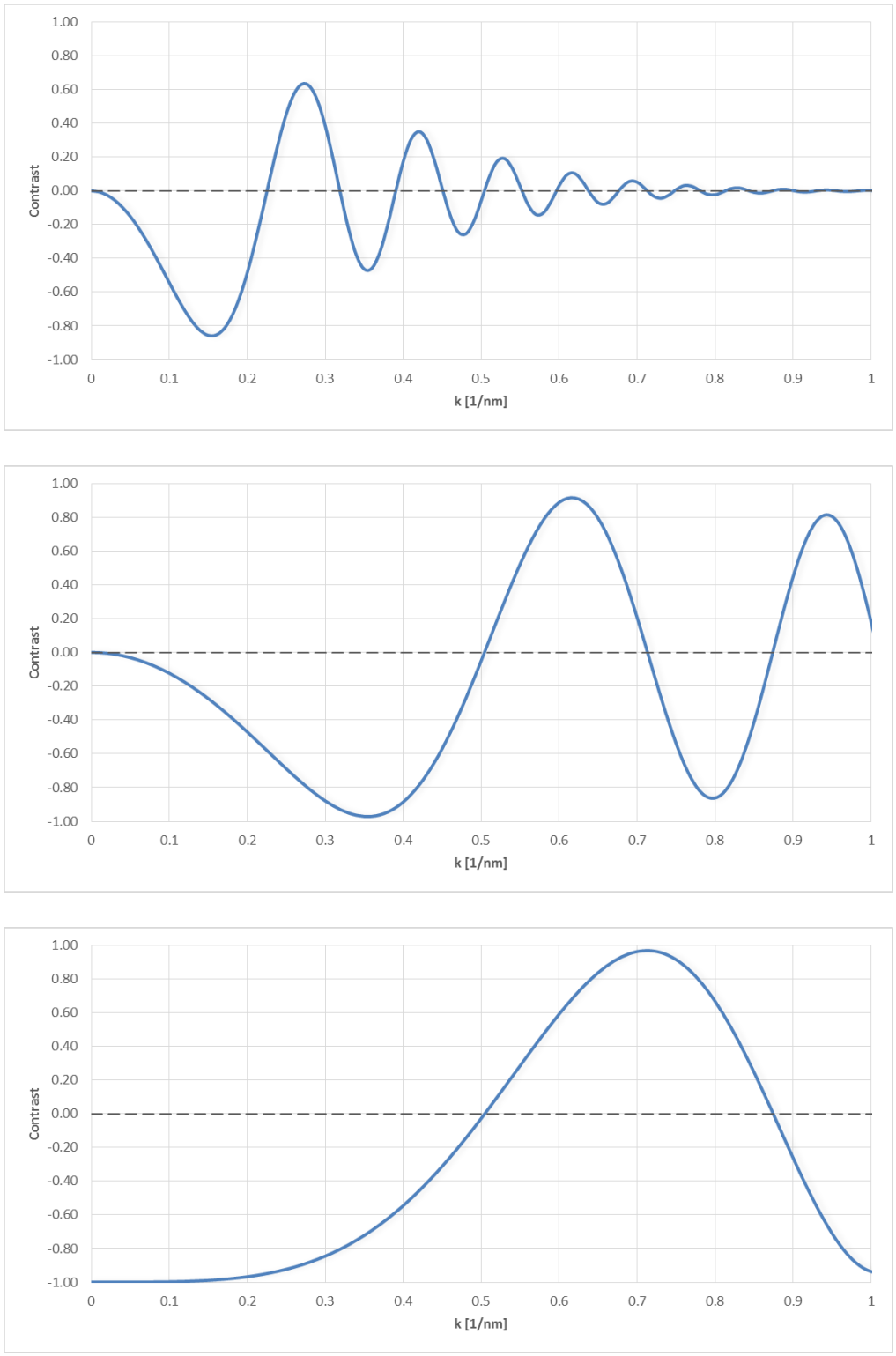

Figure 7. *Contrast transfer function of a 300 kV microscope at different defoci. Top: A defocus of -10 µm generates contrast at lower spatial frequencies* k*, but contrast inversions and attenuation increase rapidly for higher frequencies. Middle: A defocus of -2 µm shows low contrast for lower frequencies, but has a reduced attenuation of high frequencies. Bottom: The phase plate applies a phase shift of around* $\frac{\pi}{2}$*. Low spatial frequencies now start out at highest contrast values. The envelope function is significantly less pronounced due to the low defocus value (here: -1 µm).*

Given the hypersaline nature of halobacterial environments and samples for cryo-EM, particularly excessive underfocus values would be required to generate sufficient phase contrast. In turn, this would make a sufficiently precise CTF-correction of the micrographs very difficult. The VPP eliminates the need for recording at high defocus values entirely. Instead, a generic underfocus of ≈ 1 µm would ensure sufficient contrast while not risking parts of the specimen reaching large overfocus levels during tilting. This is particularly important if the induced phase shift is not exactly $\frac{\pi}{2}$, in which case contrast formation for very low frequencies and the 1st zero cut-off frequency are reduced [49].

Lastly, the VPP is also indispensable for the recording of gas vesicles. Vitrified gas vesicles of the I34M point mutant are very thin and regularly cylindrical (see 2.1.2); when oriented along the tilt axis of the microscope, the high-resolution tomographic recording of the nanometer-scale substructure becomes possible at very low defocus levels with the first CTF zero close to Nyquist frequency.

3. Materials and methods

3.1. Cell growth of *Halobacterium salinarum*

H. salinarum cells of strain S9 were kindly provided by Dieter Oesterhelt (Max Planck Institute of Biochemistry, Martinsried). Pre-cultures were attained by inoculating 1 ml of this strain in 100 ml full liquid culture medium (FLCM), consisting of 4.3 M NaCl, 81 mM $MgSO_4$ * $7H_2O$, 27 mM KCl, 10 mM 3(Na citrate) * $2H_2O$, 1 % w/v, *Oxoid*™ peptone [1] (pH 7.1). Freshly inoculated cells were incubated at 37 °C while shaking at 100 rpm in a baffled Erlenmeyer flask for 3 days. OD600 was measured to 0.9, indicating late exponential growth (see growth curve, *Figure 8*). Cultures raised for further experiments and microscopic studies were selected for motility first (see 3.3).

Pre-cultures were routinely used to create reserve cultures, by inoculating 10 ml of pre-culture in 1 l of FLCM at either 4.3 M NaCl or 3.5 M NaCl, depending on experimental requirements. Reserve cultures were incubated at 37 °C, shaking at 100 rpm in non-baffled Erlenmeyer flasks for 7 d and then stored in the shelf at room temperature.

Cells raised for the isolation of flagella (see 3.7.1) were inoculated from 1 ml reserve culture (4.3 M NaCl) in 50 ml FLCM (4.3 M NaCl). They were incubated at 37 °C while shaking at 100 rpm in a baffled Erlenmeyer flask for 4 d. Stationary phase was reached after this time, at OD600 values of 1.0 – 1.1.

Cultures intended for vitrification and transmission electron microscopic examination were inoculated from 1 ml reserve culture (3.5 M NaCl) in 50 ml FLCM (3.5 M NaCl). They were incubated at 37 °C while shaking at 100 rpm in a baffled Erlenmeyer flask for 4 d until they reached their stationary growth phase.

[1] Oxoid Limited, Basingstoke, United Kingdom

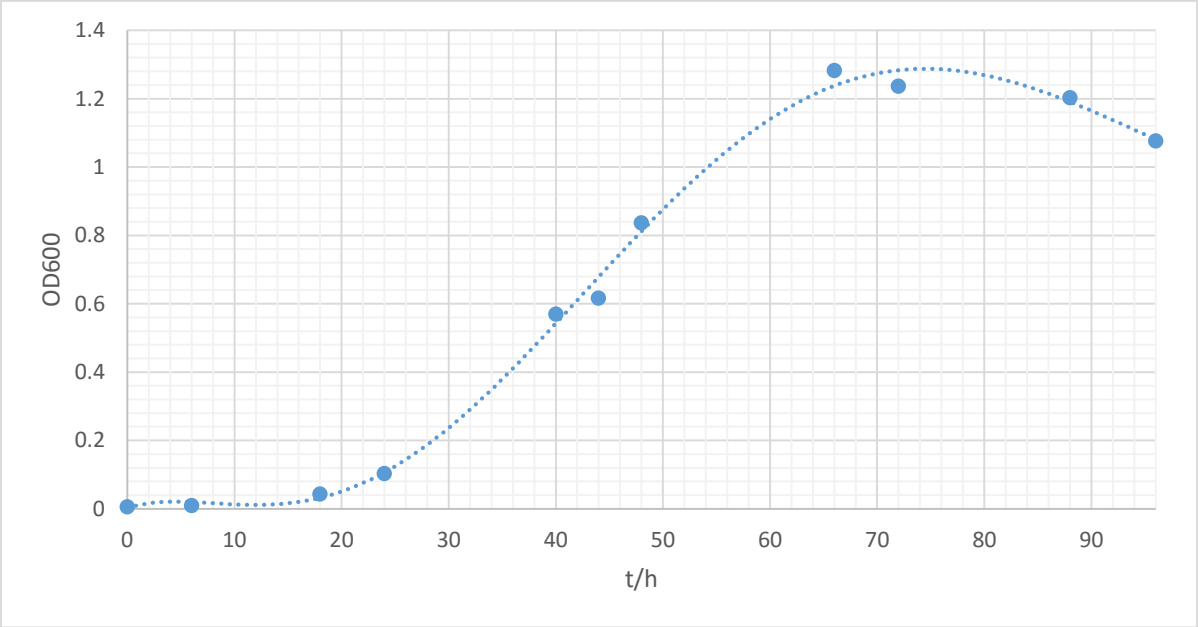

Figure 8. *Typical growth curve of H. salinarum in 4.3 M NaCl full liquid culture medium (FLCM). The lag phase usually encompasses roughly the first 24 h. Towards the end of the exponential growth phase (> 60 h) the cells become increasingly motile, as observed by light microscopic examination. During the stationary phase many cells remain motile but seem more susceptible to an additional decrease in NaCl concentration.*

3.2. Cell cultures at lower NaCl concentrations

For growth experiments at NaCl concentrations below 4.3 M, normally grown cells for inoculation were first dialyzed to dilute the salt. Cell dialysis was performed by injecting 12 ml of a cell culture into a *Slide-A-Lyzer*™ dialysis cassette[1]. The cells were then dialyzed against 1 l of full medium containing varying NaCl concentrations for 2 h. In addition, a reference had to be created in order to assess the dialysis kinetics. For this purpose, 12 ml of a 4.3 M NaCl solution in a dialysis cassette were dialyzed against 1 l of ddH_2O. Roughly every 7 min, 50 µl of sample were extracted from the cassette and diluted 1:5 with ddH_2O. In 50 µl of each diluted sample, the NaCl osmolality, which amounts to twice the molarity of undissolved NaCl, was determined with an *OSMOMAT® 030*[2] freezing point osmometer. The osmometer was previously zeroed in by 50 µl of pure ddH_2O. The resulting reference curve, adapted to NaCl molarity, is shown in *Figure 9*.

[1] Life Technologies GmbH, Darmstadt, Germany
[2] Gonotec GmbH, Berlin, Germany

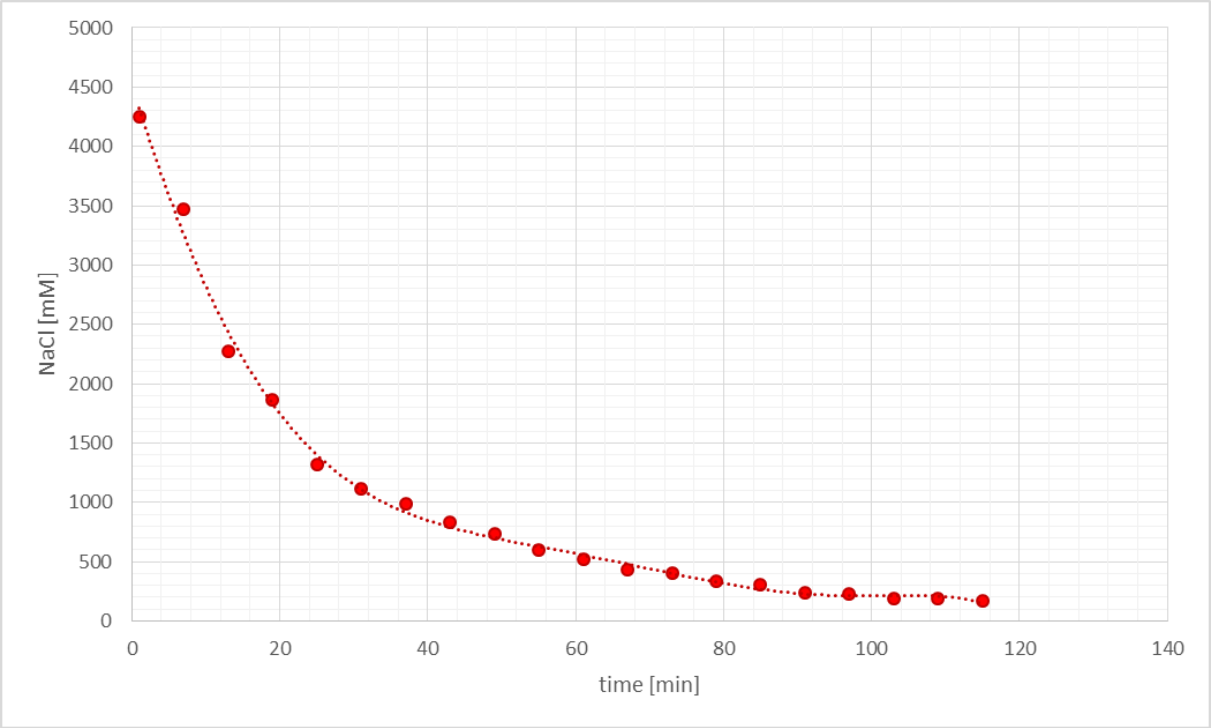

Figure 9. *Dialysis kinetics of an aqueous solution of 4.3 M NaCl dialyzed against pure water.*

For the recording of growth curves at different salt concentrations, 2 × 2 ml of each dialyzed culture were inoculated in 50 ml full medium containing the appropriate concentration of NaCl. In addition, two reference cultures of 2 ml pre-culture inoculated in 50 ml full medium at 4.3 M NaCl were raised simultaneously. All eight cultures were grown at 37 °C while shaking at 100 rpm in baffled 100 ml Erlenmeyer flasks. Cell growth for each culture was tracked by the measurement of OD600 values. Relative motility of these cultures in the late exponential phase was checked by light microscopy.

Cell samples intended for transmission electron microscopy under cryo conditions were prepared by extracting 1 ml of each culture after 71 h. Vitrification was performed manually as described in 3.4.

Cellular morphological integrity was ascertained by cryo-electron transmission microscopy of vitrified cells, using a *Tecnai Polara*[1] (see 3.5). Micrographs were recorded at a magnification of 18,000× (pixel size: 8.1 Å/pixel), with exposure times of 2 s per image at a defocus of -10 to -5 µm (depending on how much ice thickness and salt concentrations attenuated contrast formation) by a *K2 Summit* 4k × 4k direct electron detection camera[2] operating in dose fractionation mode in combination with a *Quantum* post column energy filter[4] operating in zero-loss mode.

[1] FEI, Eindhoven, The Netherlands
[2] Gatan Inc., Pleasanton, United States

3.3. Swarm agar motility assays of *Halobacterium salinarum*

Swarm agar plates were made by pouring a solution of 250 ml of swarm agar medium (0.3 % w/v agar, 4.3 M NaCl, 81 mM $MgSO_4$ * 7H2O, 27 mM KCl, 10 mM 3(Na citrate) * $2H_2O$, 1 % w/v, *Oxoid*™ peptone[1], pH 7.1) at around 60 °C into petri dishes of 6 cm in diameter. After incubation at room temperature and solidification of the swarm agar medium, 10 µl of previously prepared cell culture, grown to late log phase (see 3.1), were injected at the center of each agar plate. The plates were then incubated at 37 °C for 5 d.

Five such cultures of strain S9 were compared by measuring the diameter of the growing ring-shaped cell culture. Cells were picked from the edge of the most motile culture after 5 d and re-inoculated in 50 ml of FLCM. They were incubated at 37 °C while shaking at 100 rpm in a baffled Erlenmeyer flask for 3 d to a measured OD600 of 0.9 – 1.0.

3.4. Vitrification of *Halobacterium salinarum* cells

12 ml of a cell culture, grown in FLCM at 3.5 M NaCl to its late exponential phase (around 72 h), were carefully injected into a *Slide-A-Lyzer*™ cassette[2] and dialyzed against 1 l of an aqueous solution containing 3.0 M NaCl and 81 mM $MgSO_4$ for 2 h. For optimal distribution of the cells on the sample grid post-vitrification, the cells were concentrated by centrifuging 1 ml of the dialyzed suspension at 150 g for 30 min. The supernatant was carefully removed and the loose cell pellet re-suspended in 100 µl of 3.0 M NaCl and 81 mM $MgSO_4$. Before vitrification of the sample, intact morphology and motility of the cells were ascertained by inspection via light microscopy.

Quantifoil® Cu 200 R 2/1 holey carbon grids[3] were exposed to a glow discharge-induced plasma for 30 s to render them hydrophilic and remove potential contaminants. One grid at a time was fixated with tweezers and mounted inside a *Vitrobot*™ Mark IV[1] at room temperature and 100 % humidity. Afterwards, 4 µl of colloidal 10 nm-sized, BSA-coated fiducial gold markers and 4 µl of the concentrated cell suspension were applied. Blotting of excess liquid occurred from both sides. Immediately after, the sample grid was plunged into a 1:1 mixture of liquid ethane/propane at a temperature close to -180 °C. A blotting force setting of “5” and a blotting time of 5 s resulted in most cells encased by a 400 – 800 nm layer of vitreous ice. Ice thickness was measured in cryo-TEM by the intensity ratios of an unfiltered image to a zero-loss-filtered recording of the target region [50].

[1] Oxoid Limited, Basingstoke, United Kingdom
[2] Life Technologies GmbH, Darmstadt, Germany
[3] Quantifoil Micro Tools GmbH, Großlöbichau, Germany

3.5. Cryo-electron microscopic examination of *Halobacterium salinarum*

For initial observations, cells were grown in 3.5 M full liquid culture medium (FLCM) to an OD600 of 0.8 – 1.0. Afterwards, 12 ml of such a cell culture was injected into a *Slide-A-Lyzer*™ dialysis cassette[1] and dialyzed against 1 l of salt solutions containing between 1.0 – 2.5 M NaCl and 81 mM $MgSO_4$ for 2 h. 4 µl of a dialyzed cell suspension were applied to a *Quantifoil*® Cu 200 R 2/1 holey carbon grid[2], which had previously been plasma-cleaned for 30 s, carried 4 µl of dried-in BSA-coated 10 nm gold beads[3], and was fixated on inverted tweezers in a custom-made cryo-plunger. Excess liquid was blotted away manually and the grid plunged into liquid ethane, cooled by liquid nitrogen.

Using a 300 kV *Tecnai Polara*[4] (focal length f = 2.7 mm; spherical aberration coefficient Cs = 2.7 mm) equipped with an FEG, a post-column energy filter[5] and a 2x2k CCD detector[5] several hundred sample grids were screened. Tomograms were recorded whenever a flagellated halobacterial cell pole was opportunely positioned over a carbon hole, ideally perpendicular to the tilt axis. In addition, a series of non-flagellated cell pole tomograms were recorded. Recording parameters were as follows: Magnification factors between 18,000× and 22,500× (pixel sizes 8.1 and 6.0 Å/pixel, respectively); tilt angles -60° – +60° in 2° increments, underfocus 5 µm; total dose around 120 e/ Å². If conditions were unsuitable for tomography, due to thick ice or bad alignment of the cell, long exposure micrographs of 10 – 15 s (equating to a total dose of around 60 e/Å²) were collected instead.

3.6. Focused ion beam milling of *Halobacterium salinarum* cells

Since the electron-transparency of a sample is inversely proportional to its thickness, most eukaryotic and some prokaryotic cells are not directly suited for high resolution transmission electron microscopy under cryo conditions. In these cases, it is necessary to reduce their thickness by truncation of the material. Traditionally, this is done through cryo-sectioning. Here, the sample is cut into ultrathin slices by a microtome's diamond blade under cryo conditions. However, this introduces mechanical compression artefacts and thus reduces or destroys the pristine morphological integrity of the object. Focus ion beam (FIB) milling of biological material has since been introduced as a viable alternative [51].

A typical cryo-FIB setup consists of a Dual Beam FIB microscope (DB-FIB) equipped with a cryo system which enables the sample loading and milling at temperatures of around -180 °C. The DB-FIB combines

[1] Life Technologies GmbH, Darmstadt, Germany
[2] Quantifoil Micro Tools GmbH, Großlöbichau, Germany
[3] Aurion, Wageningen, The Netherlands
[4] FEI, Eindhoven, The Netherlands
[5] Gatan Inc., Pleasanton, United States

an independent scanning electron microscope (SEM) with the FIB component in one machine (see *Figure 10*). The SEM allows for high quality imaging without inducing significant sample damage. The working principle of the FIB is based on the ionization, acceleration and focusing of a liquid ion metal source (LIMS), typically gallium. The relatively heavy ions possess a high kinetic energy and collide with the target surface where they ablate the surface atoms. A rasterized Ga^+-beam therefore allows for the milling of material with a very high precision of several nanometers. Conductive surface coating of the specimen, for example with Pt, will reduce the local charging of the sample, which otherwise leads to distortions of the beam and the material.

For this work, a *Quanta*™ 3D FEG dual beam FIB-SEM microscope[1] [52] was used. The sample transfer was done by fixating the sample grids in autogrid cartridges and mounting them on a FIB shuttle. The shuttle was then transferred onto the FIB cryostage through a PP3000T cryo transfer system[2]. FIB milling was performed by cutting rectangular wedge patterns of 15 – 20 µm width into the specimen at a shallow angle of 4 – 6°. The ion beam parameters were set to: 30.0 kV beam energy, 1 µs dwell time and an initial current of 0.3 nA. The current was lowered incrementally to 0.03 nA for several subsequent fringe-polishing steps. The resulting wedge ideally contained several intact cells with truncated polar caps at its thin edge.

Accompanying SEM images were taken at a magnification factor of 10,000× with an acceleration voltage of 3 kV and a beam current of 20 pA. Two grids at a time were prepared in this way and between five and eight wedges were milled per grid. The grids were transferred into a grid box and stored in liquid nitrogen.

Cellular tomography on vitrified and FIB-milled samples was performed under cryo conditions (using liquid N_2 as coolant) inside a *Titan Krios*[3] with an objective lens focal length f = 3.5 mm and a spherical aberration coefficient Cs = 2.7 mm. The microscope was equipped with a 300 kV field emission gun and a *K2 Summit* 4k × 4k direct electron detection camera[4] operating in dose fractionation mode in combination with a *Quantum* post-column energy filter operated in zero-loss mode[3], as well as a heated phase plate holder [48]. Samples were previously prepared as described in 4.1.4 and 4.1.5 and mounted in an *Autoloader* sample loader magazine. Afterwards, they were and transferred onto the microscope's rotatable sample stage under cooling with liquid N_2. The Volta phase plate was aligned as described in 3.11.

[1] FEI, Eindhoven, The Netherlands
[2] Quorum Technologies, East Sussex, United Kingdom
[3] FEI, Eindhoven, The Netherlands
[4] Gatan Inc., Pleasanton, United States

Using *SerialEM*, long exposure micrographs of cells were taken at a defocus of -1 µm, at a magnification of 33,000× (pixel size: 4.21 Å/pixel), and a spot size of 9 [53]. Overview exposures at a magnification of 2,250× (pixel size: 6.08 Å/pixel) were also recorded, to be compared to non-FIB-milled samples under identical recording conditions.

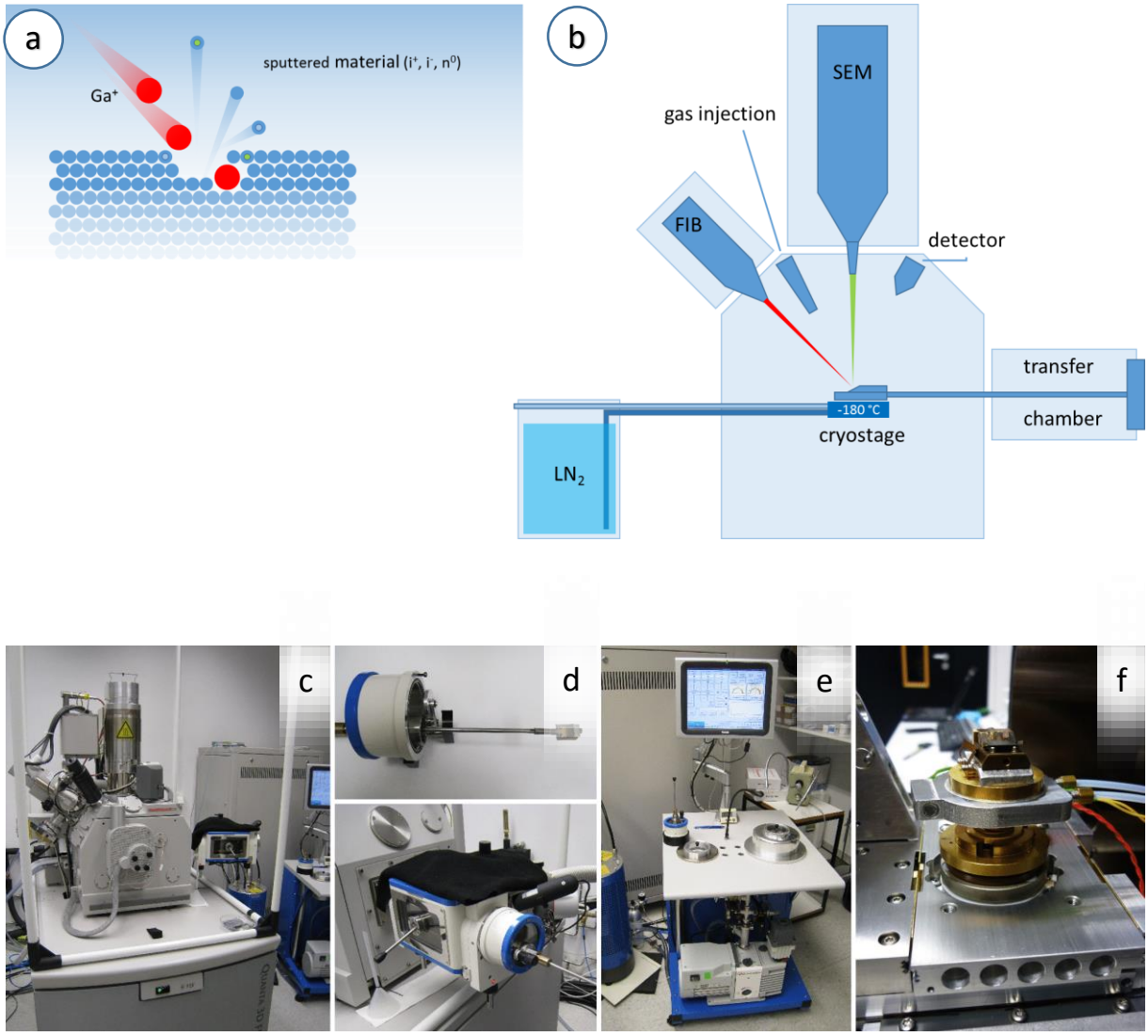

Figure 10. *Principle of focused ion beam milling (a). A beam of highly focused Ga^+ ions sputters the specimen molecules. A DB-FIB consists of two independent columns, one for an SEM and one for the FIB (b). Lower row: The DB-FIB instrument, with its two beam columns (c), the transfer chamber (d), the loading station (e) and the cryostage, where the shuttle is mounted inside the machine (f). Pictures by Miroslava Schaffer, used with permission.*

3.7. IgY-labeling of halobacterial flagella

Through the production and isolation of polyclonal Fla-specific IgY from chicken egg yolk (see 3.7.1), an antibody labeling assay was performed in the attempt to determine the flagellar growth region. IgY was deemed advantageous over its mammalian equivalent IgG due to the high yield of 40 – 80 mg of antibody per egg [54]. The produced antibody had to reliably bind under hypersaline conditions. Binding specificity and strength were ascertained via an enzyme-linked immunosorbent assay (ELISA, see 3.7.2). Additionally, halobacterial cells were incubated in full medium conditions with gold bead-conjugated IgY. The localization of the antibody-bound gold beads were observed via transmission electron microscopy.

The labeling experiment, which is summarized in *Figure 11*, required unconjugated IgY to bind to the archaeal flagella of living halobacterial cells with great specificity. Afterwards, the cells were incubated at 37 °C for a set amount of time, and then hot-labeled with Fluorescein isothiocyanate (FITC)-conjugated IgY. The growth region should contain a notably higher proportion of FITC-conjugate and thus emit a localizable fluorescent signal at the flagellar growth site.

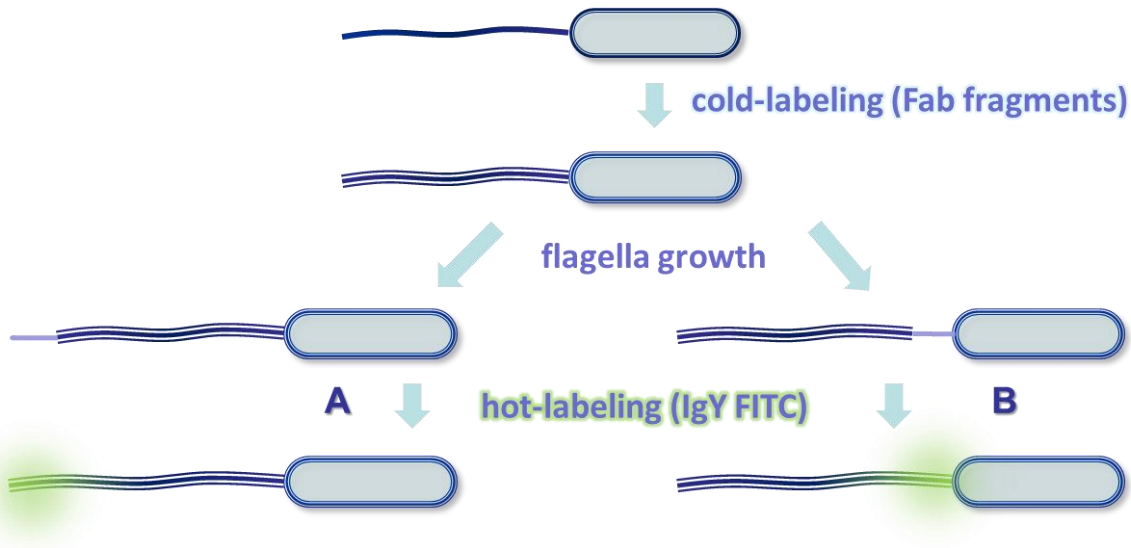

Figure 11. *Antibody-labeling assay for the localization of the flagellar growth site. The flagella of living cells are coated with Fla-specific, polyclonal IgY (cold-labeling). The flagella continue to grow and a second labeling assay, this time with FITC-conjugated IgY, binds predominantly to the fresh, unlabeled Fla protein at the growth site, distally (scenario A) or proximally (scenario B).*

3.7.1. Production of polyclonal IgY antibodies against Fla protein

In order to isolate and purify flagella to be used as the antigen in the immunization trials, 10 ml of a *H. salinarum* pre-culture were inoculated in 1 l of FLCM and grown at 37 °C, shaking at 100 rpm for 6 d. The cell suspension was subsequently centrifuged at 12,000 g for 30 min at 10 °C and the cell pellet discarded. The supernatant was ultracentrifuged at 100,000 g for 1:15 h at 4 °C and the resulting pellet, which consisted mainly of shed halobacterial flagella, was re-suspended in 2.5 ml elution buffer, consisting of 2 M NaCl, 50 mM Tris(hydroxymethyl)aminomethane (Tris) at pH 7.1.

500 µl of this raw flagella suspension were mixed with 100 µl of a lysis buffer with 0.1 % w/v Na-taurodeoxycholate, 2 M NaCl, 50 mM Tris at pH 7.1 and vortexed. 250 µl of lysis buffer with 3 % w/v Triton X-100 instead of Na-taurodeoxycholate were added. The solution was vortexed for 20 s and centrifuged at 12,000 g for 2 min. This step was repeated one more time. Afterwards, the lack of a pellet after centrifugation indicated complete solubilization of the sample. For further purification, 500 µl of the sample were injected onto a sepharose CL-4B column[1] (10/300, bed volume: 24 ml) for size exclusion chromatography via an *ÄKTApurifier 10/100*[1] fast protein liquid chromatography (FPLC) system. The column was equilibrated in lysis buffer with 0.1 % w/v Na-taurodeoxycholate. At a flow rate of 0.4 ml/min lysis buffer, early proteins peaks detected by light absorption at 280 nm were collected and combined (see *Figure 12*). 4 µl of purified flagella fractions were incubated on a plasma-cleaned (30 s) carbon-foil microscope grid for 60 s, blotted, and incubated on a 4 µl droplet of freshly mixed 2 % w/v uranyl acetate solution. Excess liquid was blotted away and the sample grid examined in an electron microscope (a CM200 TEM with a 200 kV field emission gun). An exemplary micrograph is shown in *Figure 13*.

[1] GE Healthcare Europe GmbH, Freiburg, Germany

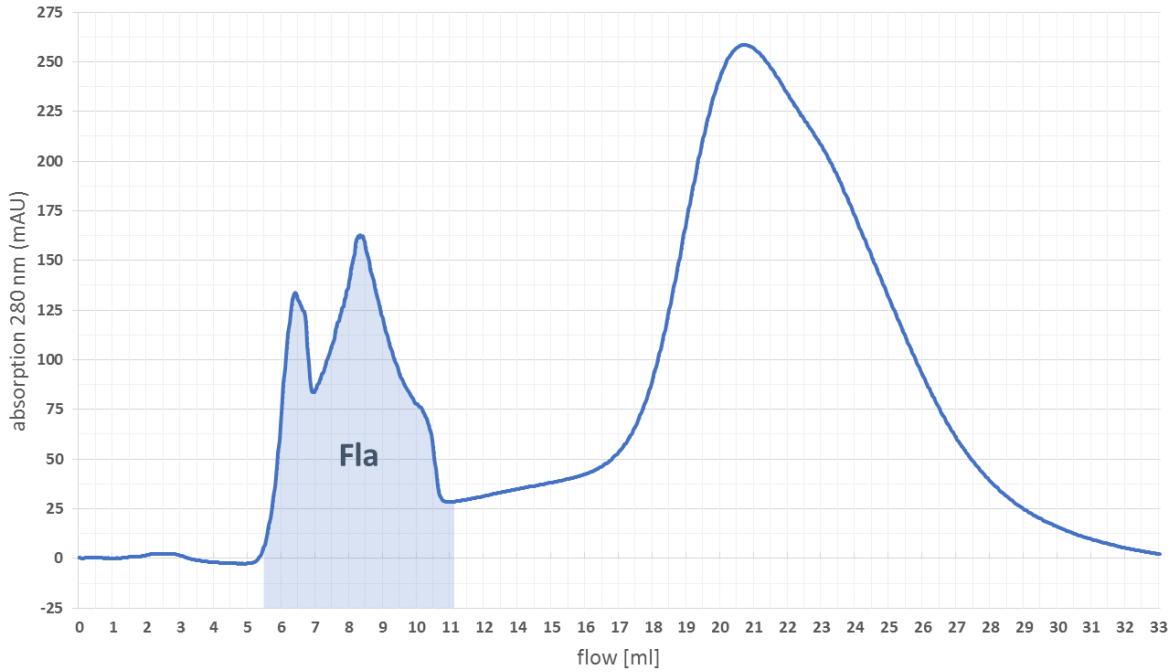

Figure 12. *Size exclusion chromatography of halobacterial flagella raw isolate. The highlighted peak fractions were collected and combined. Isolated flagella were negatively stained and examined under a transmission electron microscope (see below).*

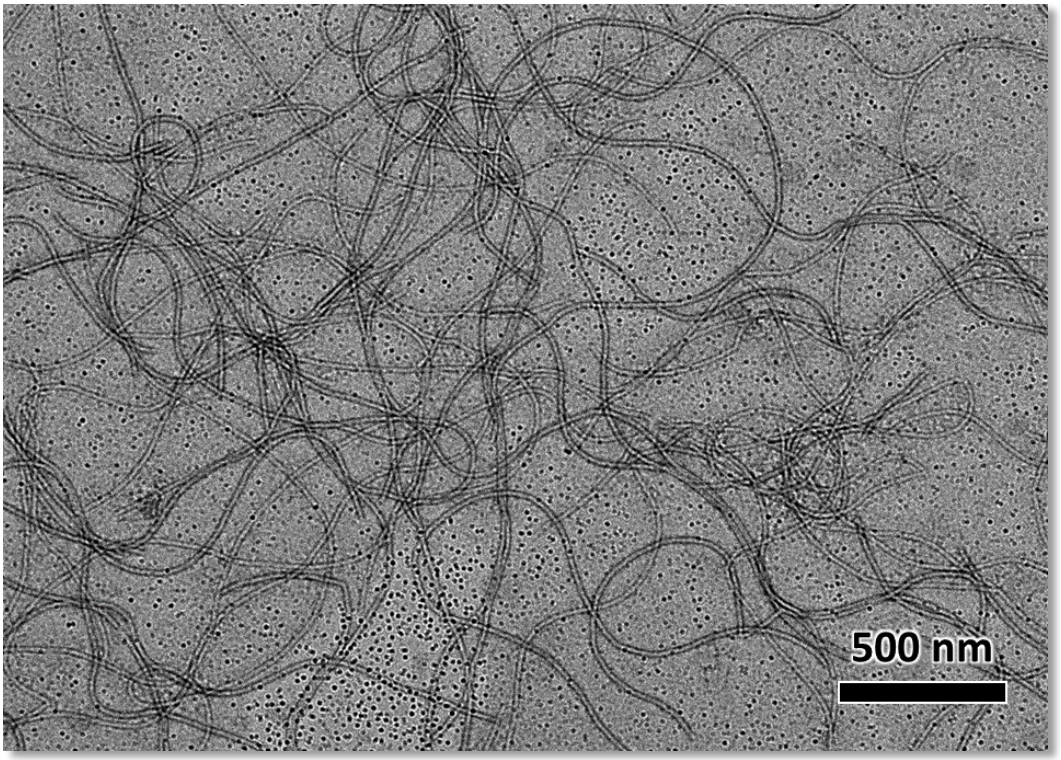

Figure 13. *Negative stain of isolated halobacterial flagella with 2 % uranyl acetate. The preparation served to raise Fla-specific polyclonal IgY antibodies through the immunization of chickens.*

For the immunization of chickens, 250 µl of the solution containing purified flagella fragments were mixed with 500 µl *TiterMax® Gold* adjuvant[1], forming a white, oily emulsion. Two chickens were injected with 300 µl of this emulsion, respectively. Two additional boost injections were conducted after one month and two months. For boosting, 100 µl of the flagella isolate were mixed with 100 µl of Freund's incomplete adjuvant[1]. The chickens started laying eggs after 11 d. A total of 54 eggs were collected and stored, separated by the hen of origin, at 4 °C.

For the purification of IgY antibodies the protocol of Pauly *et al.* was used [54]. The procedure was performed for both egg types separately. The chicken eggs were cracked, the yolk separated with a yolk spoon, and the egg white discarded. The yolk skin was carefully cut and the liquid egg yolk transferred into 50 ml *Falcon* tubes. Each egg held around 10 ml of yolk liquid, which was mixed with phosphate-buffered saline (PBS, 2 ml per 1 ml yolk) at pH 7.4 and polyethylene glycol 6000 (PEG, average M_n 6,000, 3.5 % w/v). The solutions were vortexed thoroughly and shaken at 60 rpm for 20 min. The mixture was then centrifuged at 13,000 g for 20 min at 4 °C. The supernatant was transferred into fresh *Falcon* tubes through a funnel with folded filter paper. PEG 6000 was added (8.5 % w/v) and the suspension was vortexed and shaken at 60 rpm for 20 min. The centrifugation was repeated as described above. This time, the supernatant was discarded and the pellet re-suspended in 1 ml PBS. PBS was added to a volume of 10 ml. To this, 1.2 g of PEG6000 (12 % w/v) were added and the mixture vortexed, shaken at 50 rpm for 10 min and centrifuged as previously described. The supernatant was discarded and the pellet re-suspended in 800 µl PBS. Each 800 µl portion was mixed with an additional 400 µl PBS and pipetted into a dialysis bag. Dialysis against a solution of 1600 ml 0.1 % w/v NaCl took place over night. The solution was then dialyzed against PBS for 3h and transferred into 2 ml *Eppendorf* tubes. The concentration of each fraction was calculated via absorption at 280 nm and an extinction coefficient of 1.33 for IgY [54]. The isolated antibodies were stored at -20 °C.

3.7.2. Fla-binding specificity of IgY under hypersaline conditions

An indirect enzyme-linked immunosorbent assay (ELISA) was performed to screen IgY specificity to Fla antigen at different concentrations. A 96-well polystyrene ELISA plate with a well volume of 360 µl was coated with 100 µl of isolated Fla antigen (200 µg/l in PBS, pH 7.4, wells A1 to A6 and E7 to E12) and milk powder (5 % w/v in PBS, pH 7.4, right half, columns 7 to 12). A ten-fold serial dilution of the antigen was done for rows B – D and F – H respectively. The plate was covered with *Parafilm* and incubated at room temperature for 2 h while gently shaking. The wells were then washed with PBS three times, blocked with 250 µl milk powder (2 % w/v in PBS, pH 7.5), covered with *Parafilm* and

[1] Sigma-Aldrich, Munich, Germany

incubated for 2 h at room temperature. After blocking, the plate was washed again three times with PBS. 100 µl of isolated IgY from the first chicken (3 mg/ml in 4.3 M NaCl, 81 mM MgSO4, columns 1 and 7, rows A – D) and 100 µl of IgY isolated from the second chicken (3 mg/ml in 4.3 M NaCl, 81 mM MgSO4, columns 1 and 7, rows E – H) were added. The antibody was diluted ten-fold in a column-wise dilution series for columns 2 – 6 and 8 – 12 respectively. The plate was washed three times with PBS containing 0.05 % polysorbate 20 (PBST) and then three times with PBS. 100 µl of a secondary rabbit anti-chicken IgY (0.3 µg/ml in PBST) conjugated to horseradish peroxidase (HRP) was added to each well and the plate was incubated for 30 min. Afterwards, the wells were was washed three times with PBST and three times with PBS. 100 µl of a *1-step ELISA Ultra TMB Substrate* solution[1] (containing 3,3',5,5'-tetramethylbenzidine) was added and the plate incubated for 15 min. After this time, oxidation of TMB through HRP was stopped by the addition of 100 µl H_2SO_4 (2 M).

Additionally, the localization of the purified IgY was observed via transmission electron microscopy of vitrified halobacterial cells under cryo conditions. 500 µl of the cell suspension were incubated with 100 µl of isolated IgY at 20mg/ml for 1 h. Afterwards, the cells were washed by adding 500 µl of peptone-free FLCM. The mixture was centrifuged at 6,000 g for 15 min at 10 °C, the supernatant carefully discarded and the small pellet re-suspended in 250 µl peptone-free FLCM. 100 µl of a donkey-anti-chicken secondary antibody conjugated with 12 nm gold beads (15mg/ml)[2] were added and the solution incubated for 1 h. 4 µl of the antibody-labeled cell suspension were then vitrified according to 4.1.4. The samples were screened in a 300 kV *Tecnai Polara* transmission electron microscope[3].

In a preliminary labeling experiment, live cells were directly coated with FITC-conjugated IgY to determine the extent of cross-reactivity in FLCM. For this purpose, 0.5 ml of 2 mg/ml IgY in borate buffer (0.1 M Na tetraborate, pH 8.5) were mixed with 100 µl FITC (20 mM in dimethylformamide) and incubated for 1 h. Unreacted FITC was removed via dialysis against 1 l of a solution containing 4.3 M NaCl and 81 mM $MgSO_4$ for 1 h. The conjugate was freshly prepared directly before use. 1 ml of a cell culture in its late exponential growth phase (OD600 0.8) was mixed with 100 µl of the IgY-FITC conjugate in an *Eppendorf* tube and incubated at room temperature for 30 min. The mixture centrifuged at 6,000 g for 20 min at 4 °C, the supernatant discarded and the cell pellet re-suspended in peptone-free FLCM. Immediately afterwards, the cells were examined under a fluorescence light microscope at a magnification of 63×. Fluorescence emission was induced by laser light at 488 nm.

[1] Thermo Fisher Scientific, Waltham, United States
[2] Abcam plc, Cambridge, United Kingdom
[3] FEI, Eindhoven, The Netherlands

3.8. Isolation of gas vesicles

Cell cultures intended for gas vesicle isolation were grown as described before (see 3.1). After reaching an OD600 of 0.8 these cultures were kept at room temperature for 12 – 15 h. Afterwards they were allowed to reach their stationary growth phase at 37 °C, at an OD600 of around 1.2 – 1.4. These cells were stored at room temperature for several weeks, during which gas vesicle-rich cells would float up into a densely-packed, milky white surface layer near the edge of the Erlenmeyer flask. The layer was gently scooped up using a glass pipette. Afterwards, the concentrated, gas vesicle-rich cells were washed with 10 ml ddH_2O per 1 ml cell concentrate. The resulting lysate was centrifuged at 100 g for 2 h at 4 °C, pelleting the cell debris and speeding up flotation of gas vesicles into a thin, turbid layer. This layer was carefully transferred into 1.5 ml *Eppendorf* tubes at 500 µl per tube. 500 µl of ddH_2O were added to each assay and the suspension centrifuged at 100 g for 1 h at 4 °C to remove further impurities. The washing step was repeated one more time to gain a concentrated suspension of isolated intact gas vesicles for mass spectrometry analysis as well as vitrification and cryo-electron tomography. For a second mass spectrometry sample, the washing step was repeated three times in total, which was thought to remove the externally adhering GvpC protein, as previously described by Strunk *et al*. [33]. The concentration of the gas vesicle isolates was measured via UV absorption at 280 nm, after ultrasonication of a small amount of sample. It amounted to around 10 mg/ml for samples which were washed two times and around 6 mg/ml for the four-times washed sample.

In addition to halobacterial wild type vesicles, isolated vesicles carrying a GvpA point mutation were kindly provided by our collaborator Felicitas Pfeifer (Technical University of Darmstadt). This GvpA point mutant, I34M, carries an isoleucine instead of a methionine in its predicted beta turn at amino acid position 34 and forms particularly long and thin cylindrical vesicles (see 2.1.2). I34M vesicles were heterologously expressed in the mesophilic halophile archaeon *Haloferax volcanii*, isolated and washed off GvpC as described by Strunk *et al*. [33].

3.8.1. Mass spectrometry of solubilized wild type gas vesicles

Due to the extremely hydrophobic nature of GvpA, complete solubilization of the protein is difficult [29, 30]. In order to facilitate this process, samples of isolated wild type gas vesicles (see previous chapter) were ultrasonicated using a *BioRuptor*[1] device, with ten 60 s cycles at 4 °C. The resulting suspension of gas vesicle debris was then mixed with formic acid to a final concentration of 6.5 M. This concentration was deemed appropriate in order to at least partially dissolve the very

[1] Diagenode s.a., Seraing, Beldium

hydrophobic, aggregative GvpA on one hand and not further increase the rate of potential formylation artefacts, which can occur in such environments [55].

Mass spectrometry analysis was performed using a liquid chromatography electron spray ionization mass spectrometry (LC-ESI-MS) setup, with a *micrOTOF*[1] time-of-flight (TOF) mass spectrometer. 50 µl of this mixture liquid chromatography mass spectrometry (LC-MS). Here, 50 µl of the solubilized gas vesicle sample were injected onto an *Aeris* widepore C4 column[2] (100 × 2.1 mm column size, 3.6 µm particle size). At a flow rate of 250 µl/ml of an initial gradient of 50 % buffer A (0.05 % trifluoroacetic acid in H_2O) and 50 % buffer B (0.05 % trifluoroacetic acid in acetonitrile), which was steadily increased to 90 % buffer B within 15 min, eluting protein was detected by UV absorption at 214 nm. The sample was subsequently nebulized, desolvated and ionized, after which it entered the mass spectrometer. UV-absorption protein peaks were correlated to their corresponding mass spectra. The recorded mass spectrometric raw data was deconvoluted via an entropy measure-based algorithm as described by Reinhold and Reinhold [56].

3.8.2. Vitrification of intact wild type vesicles

A *Quantifoil*® Mo 200 R 2/1 holey carbon grid[3] was fixed with tweezers and mounted inside a *Vitrobot*™ Mark III[4]. The Mark III is very similar in design to the Mark IV, but features a blotting offset control parameter, which describes the position of the grid in between the blotting pads, instead of the arbitrary blotting strength scale of its successor model. Generally, 4 µl of a dense suspension of isolated wild type vesicles were applied and incubated at room temperature and 70 % humidity for 20 s. Afterwards, 4 µl of a tenfold concentrated 10 nm-sized BSA-coated colloidal gold were added. The grid carrying the sample suspension was then blotted from both sides for 3 s, with a blotting offset of -3 mm. It was subsequently plunged into a cryogenic coolant of 1:1 liquid ethane/propane at around -180 °C to induce vitrification. Further vitrification settings were tested for optimization (see results, 4.3.2).

3.8.3. Vitrification of intact I34M point mutant gas vesicles

For the vitrification of point mutant vesicles, different parameters had to be chosen, as the total available material was scarcer and the solution less concentrated. Here, a *Vitrobot*™ Mark IV[2] was set

[1] BRUKER DALTONIK GmbH Life Sciences & Chemical Analysis, Bremen, Germany
[2] Phenomenex LTD, Aschaffenburg, Germany
[3] Quantifoil Micro Tools GmbH, Großlöbichau, Germany
[4] FEI, Eindhoven, The Netherlands

to 70 % humidity at room temperature. Here, too, different settings were tested (see 4.3.2). Exemplarily, 4 µl of the vesicle suspension were mixed with 3 µl colloidal 10 nm gold. 4 µl of this mixture were then applied on a *Quantifoil*® Mo 200 R 2/1 holey carbon grid[1], fixated on tweezers inside the *Vitrobot* chamber. After an incubation time of 5 s, the grid was blotted from both sides at a blotting force of "3" for 4 s and immediately plunged into liquid ethane at a temperature of approximately -180 °C.

3.9. Transmission electron microscopy and dose tolerance of gas vesicles

Electron microscopy was performed under liquid N_2 cooling, using a *Titan Krios*[1] microscope (objective lens focal length 3.5 mm; spherical aberration coefficient, Cs = 2.7 mm) with a 300 kV field emission gun. The microscope was further equipped with a *K2 Summit* 4k × 4k direct electron detection camera[2] operating in dose fractionation mode, a *Quantum* post-column energy filter operated in zero-loss mode[3] and a heated phase plate holder for the Volta phase plate [48].

Sample grids prepared according to 3.8.2 and 3.8.3 were put on a metal frame cartridge, fixated with a clip ring and mounted in an *Autoloader* sample loader magazine. They were then and transferred onto the microscope's sample stage under cooling with liquid N_2. This stage is mechanically adjustable and capable of rotating between -70° and +70°. The Volta phase plate was aligned as described in 3.11. At a primary magnification of 64,000× (pixel size: 2.25 Å/pixel, spot size: 7), wild-type and point mutant vesicles were exposed to a series of 5 s exposures, with 14 e/Å² each. This lead to the creation of dose series recordings in order to evaluate the radiation resistance of gas vesicles for cryo-electron tomography. Power spectra of the single micrographs within a series were generated using the *MATLAB*[3]-based *TOM Toolbox* software package [57]. An exemplary point mutant dose series is evaluated in chapter 4.3.4.

[1] Quantifoil Micro Tools GmbH, Großlöbichau, Germany
[2] Gatan Inc., Pleasanton, United States
[3] MATLAB and Statistics Toolbox Release 2014a, The MathWorks, Inc., Natick, United States

3.10. Cryo-electron tomography

Cryo-electron tomography (CET) allows for the three-dimensional reconstruction of a sample from a series of two-dimensional projections. To achieve this, the specimen is mounted on a microscope sample stage which can be rotated around an axis perpendicular to the electron beam. A number of micrographs are recorded at different tilt angles. The projection-slice theorem predicates that this tilt series of two dimensional projections inherently holds the *a priori* unknown three dimensional information of the imaged object [58]: A Fourier-transform of a single projection corresponds to a two-dimensional slice through the center of the three-dimensional Fourier-transform of the object, as shown in *Figure 14*.

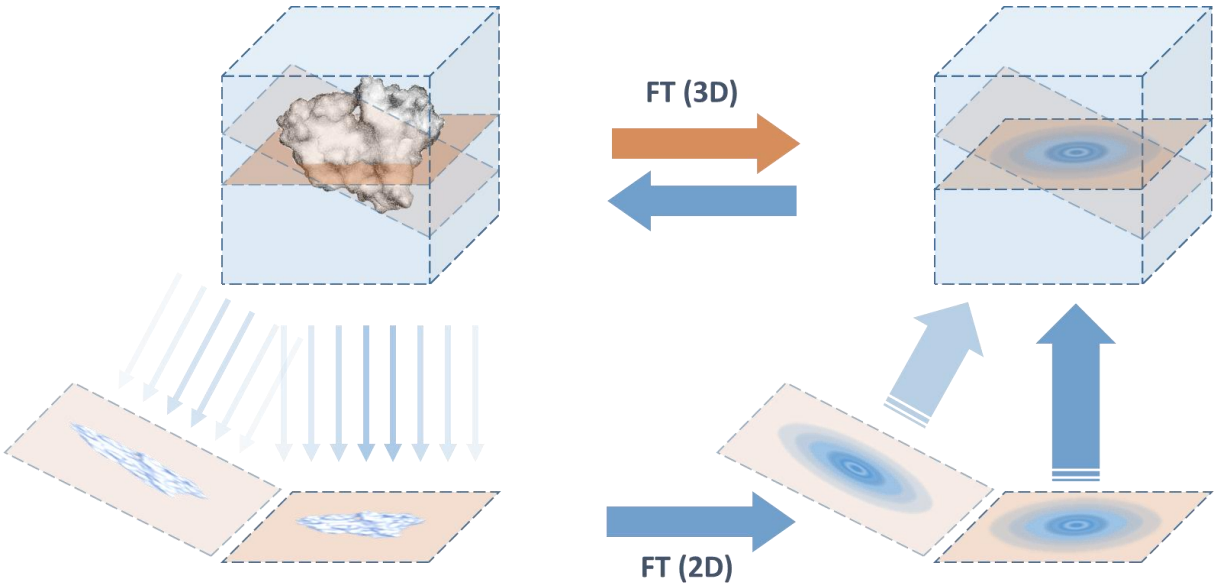

Figure 14. *The projection-slice theorem states that the Fourier-transform of an object's two-dimensional projection is equivalent to a slice through the Fourier-transform of the object. In tomography, a number of rotated projections can be used to reconstruct the original three-dimensional object through their Fourier-transforms.*

This means an unknown three-dimensional object can be reconstructed from the inverse Fourier-transform of its two-dimensional, Fourier-transformed projection slices, so long as their relative tilt angles and positions are known.

In CET, projections of an object of interest within a vitrified sample are recorded at different tilt angles with identical recording conditions. This tilt series is then computationally aligned and back-projected to reconstruct the three-dimensional volume information (see *Figure 15*). In order to facilitate accurate positional alignment of the different projections in the tilt series, fiducial markers such as inert, uniformly-sized gold beads are added to the sample prior to vitrification of the sample.

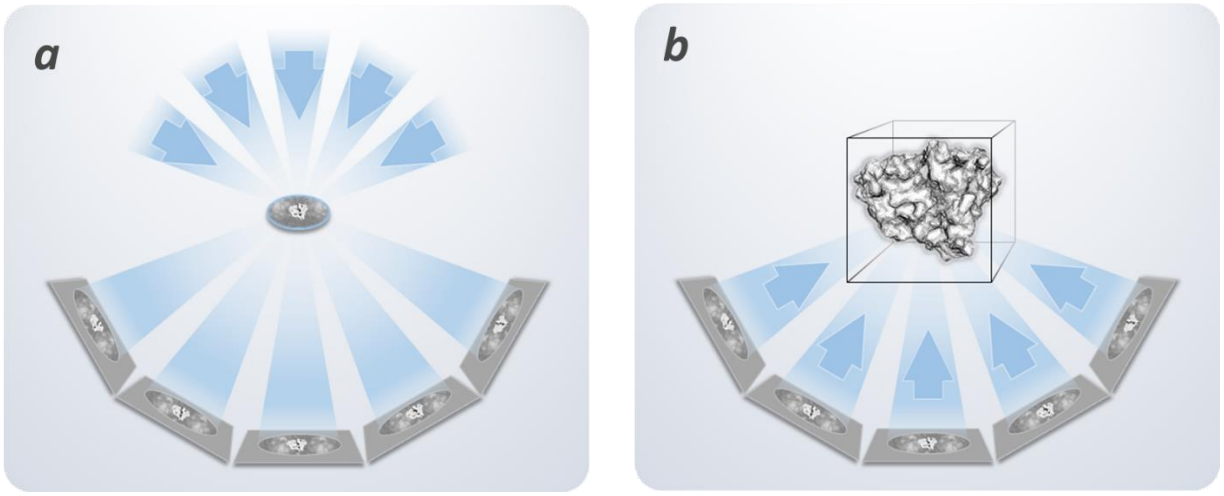

Figure 15. *The basic principle of tomography: A projections series of an object at different tilt angles is recorded (a). In CET, the sample and not the beam is rotated. The resulting tilt series is aligned in-silico and back-projected to form the original, three-dimensional object (b).*

Conventionally, the Crowther Criterion [59] is applied to define the highest isotropic resolution attainable in tomography:

$$d = \frac{\pi D}{N}$$

A spatial distance d is still resolvable if a cylindrical object of diameter D is compartmentalized by at least N projections taken at constant angular spacing over the full tilt range of 180°. The noise decreases at a factor of $1/\sqrt{N}$. Thus, the quality of the reconstruction increases with higher angular range and smaller angular increments. Tilting a slab-like sample, however, increases the projected sample thickness along the beam direction. Tilting by 90° would require the electrons to traverse the sample entirely longitudinally. In combination with the mechanical limitations of the specimen holder this renders the recording of the object at full angular range unfeasible. Since electron dose is a crucial constraint for biological specimens, a tilt scheme of -60° to +60° in 2° tilt increments is ordinarily used as a trade-off between information coverage and sample damage.

The omission of the remaining 60° results in a wedge-shaped information gap in Fourier space, a "missing wedge" around the beam axis (see *Figure 16*). This causes reconstructed objects to distort in this direction, effectively decreasing the resolution along the Z-axis. As a consequence, the missing wedge effect must be taken into account for subtomogram analysis (see 3.12).

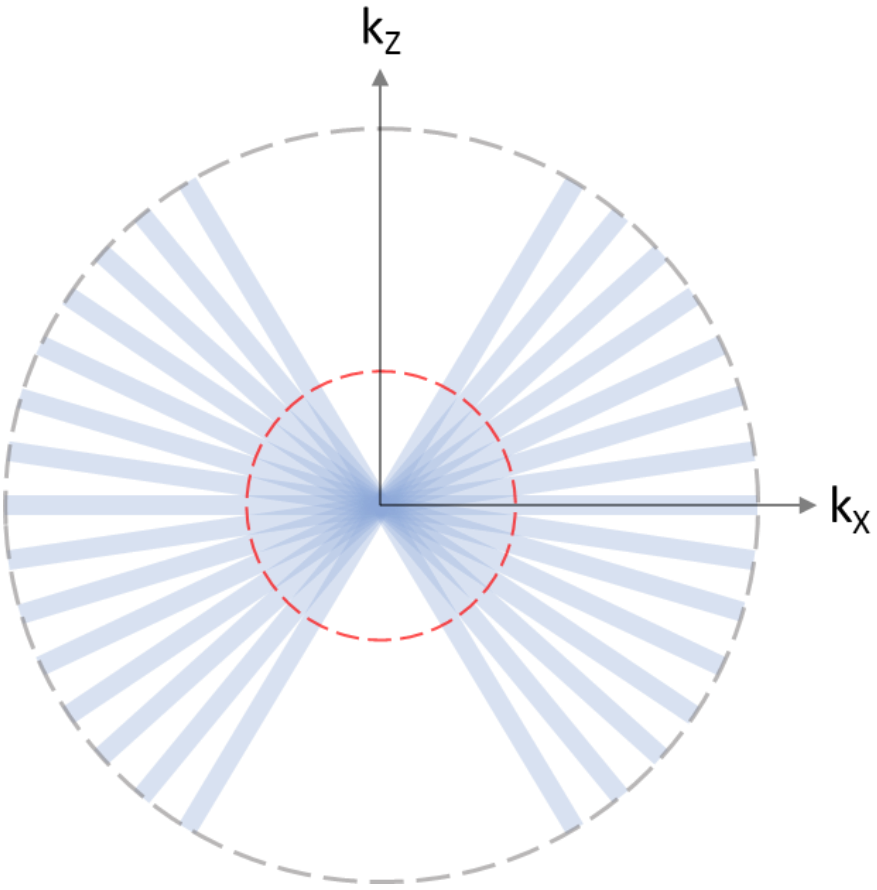

Figure 16. *Schematic presentation of a tomographic tilt series (blue slices) in Fourier space. Each slice represents one projection at a different tilt angle, with the 0° projection oriented along k_X. Clearly visible is the non-sampled missing wedge along k_Z. The grey circle represents the limit of information transfer, while the red circle indicates the limit of continuously sampled spatial information (Crowther limit). Note how low frequency information of the projection slices begins to overlap. This artificially enhances low frequency contributions and needs to be taken into account during the reconstruction. Typically, these frequencies are attenuated by a weighting function in a so-called weighted backprojection.*

In practice, electron dose exposure for the specimen of choice is almost exclusively used for the recording of the tilt series. In this frequently applied low-dose scheme any beam operations, such as beam alignments, defocus and drift measurements (tracking), are performed on a dedicated trial position that lies along the tilt axis of the sample stage within a few µm from the recording site. An example of a typical low dose recording scheme is shown in *Figure 17*.

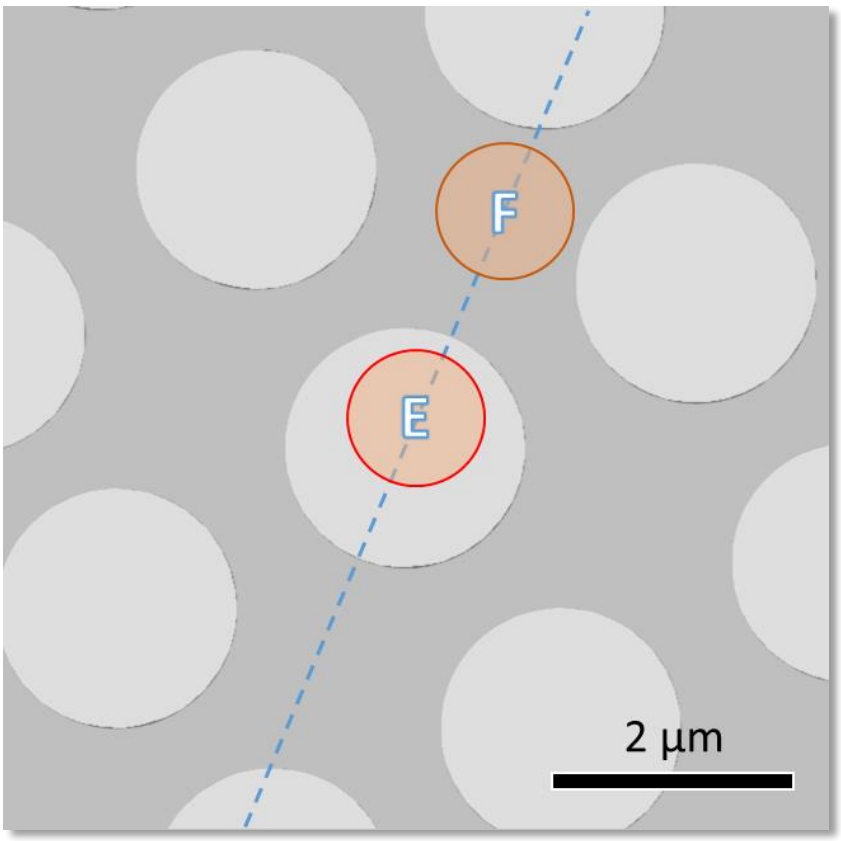

Figure 17. *Schematic illustration of a typical low-dose recording setup for cryo-electron tomography. The target of interest is at the recording, or exposure site (E). Before recording, a beam shift is applied to a nearby trial, or focus spot (F) along the tilt axis (blue line). Here, focus measurements and image cross-correlation to counter mechanical drift are performed. The beam then shifts back and records the current image of the tilt series with the determined parameters. The two sites should be further apart than the total beam diameter at working magnification.*

3.10.1. CET of isolated halobacterial gas vesicles

SerialEM was used for tomographic recording [53]. For each tomogram a tilt series from -60° to +60° was recorded in 2° tilt increments at a magnification factor of 64,000×, which resulted in a pixel size of 2.25 Å/pixel. The total electron dose per tomogram never exceeded 40 e/Å², as halobacterial gas vesicles proved to be particularly sensitive to radiation damage (see 3.9). The integrity of the vesicle structure was ascertained by comparing the diffraction pattern of the vesicle helix (layer lines) within the power spectrum of each tilt series' first and the last micrograph (see recorded electron dose series, chapter 4.3.3). Tilt series with detectable degradation of higher order diffraction patters were discarded.

Generally, a defocus was applied which showed the first zero of the power spectrum discernibly approaching Nyquist frequency. This was frequently validated by observing the power spectra of individual 3 s trial exposure micrographs on the focus spot. Subframe alignment was performed post-recording via *DigitalMicrograph*[1], to compensate for beam-induced shifts during exposure.

Each subframe-aligned tilt series was processed in IMOD[2] [60]. Individual micrographs of a tilt series were aligned by tracking the sample-embedded 10 nm gold beads (see 3.8.2 and 3.8.3) as fiducial markers. The final alignment step used the linear interpolation option of IMOD to reduce high frequency noise. The tomographic volume data was reconstructed through weighted backprojection of the unbinned, low pass-filtered (high frequency filter cutoff, 0.35; sigma, 0.05) tilt series.

[1] Gatan Inc., Pleasanton, United States
[2] http://bio3d.colorado.edu/imod/

3.11. Operation of the Volta phase plate

The Volta phase plate is a sheet of thin carbon film situated at the back focal plane of the objective lens. It causes a phase retardation of central diffraction beam electrons close to $\frac{\pi}{2}$ through the induction of a negative Volta potential on the film (see 2.2). In order to function properly, it therefore requires to be aligned on-plane with the crossover of the central diffraction beam. Misalignment leads to deviation from the optimal phase shift of $\frac{\pi}{2}$ and an increased cut-on frequency, causing the phase plate to underperform [48]. It also requires applied beam shifts to correctly converge in the objective lens' back-focal plane (see *Figure 18*). This is essential during tomography, as the beam is shifted between the recording and trial site. Incorrectly adjusted beam pivot points create an additional, displaced Volta potential on the carbon film. This will distort the CTF and introduces non-uniform, anisotropic contrast formation [49].

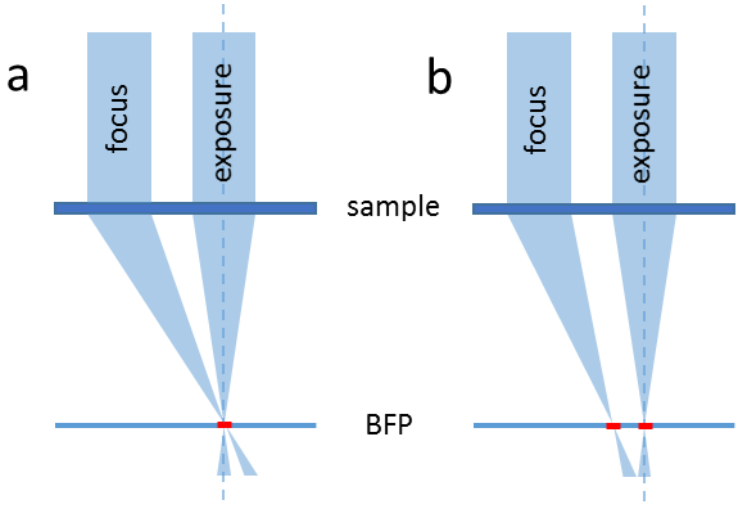

Figure 18. *Well-aligned beam pivot points (a) exhibit a common, central crossover in the back-focal plane of the objective lens. Misadjusted pivots points (b) lead to the creation of two crossovers, one of which causes the emergence of a second Volta potential that interferes with contrast formation. Modified from [49].*

To ascertain the on-plane condition of the Volta phase plate within a *Titan Krios* transmission electron microscope (see 3.9, and 4.3.4 respectively), the pattern projected by the phase plate's carbon film onto the image plane is observed. While fine-adjusting the C2 and C3 lens currents in "Fine focus back-focal plane" mode of the *TEM User Interface* (TUI) software, this granular pattern, called a Ronchigram, appears heavily blurred right as the moving beam crossover converges on the back-focal plane [49]. *Figure 19* illustrates the on-plane alignment of the Volta phase plate.

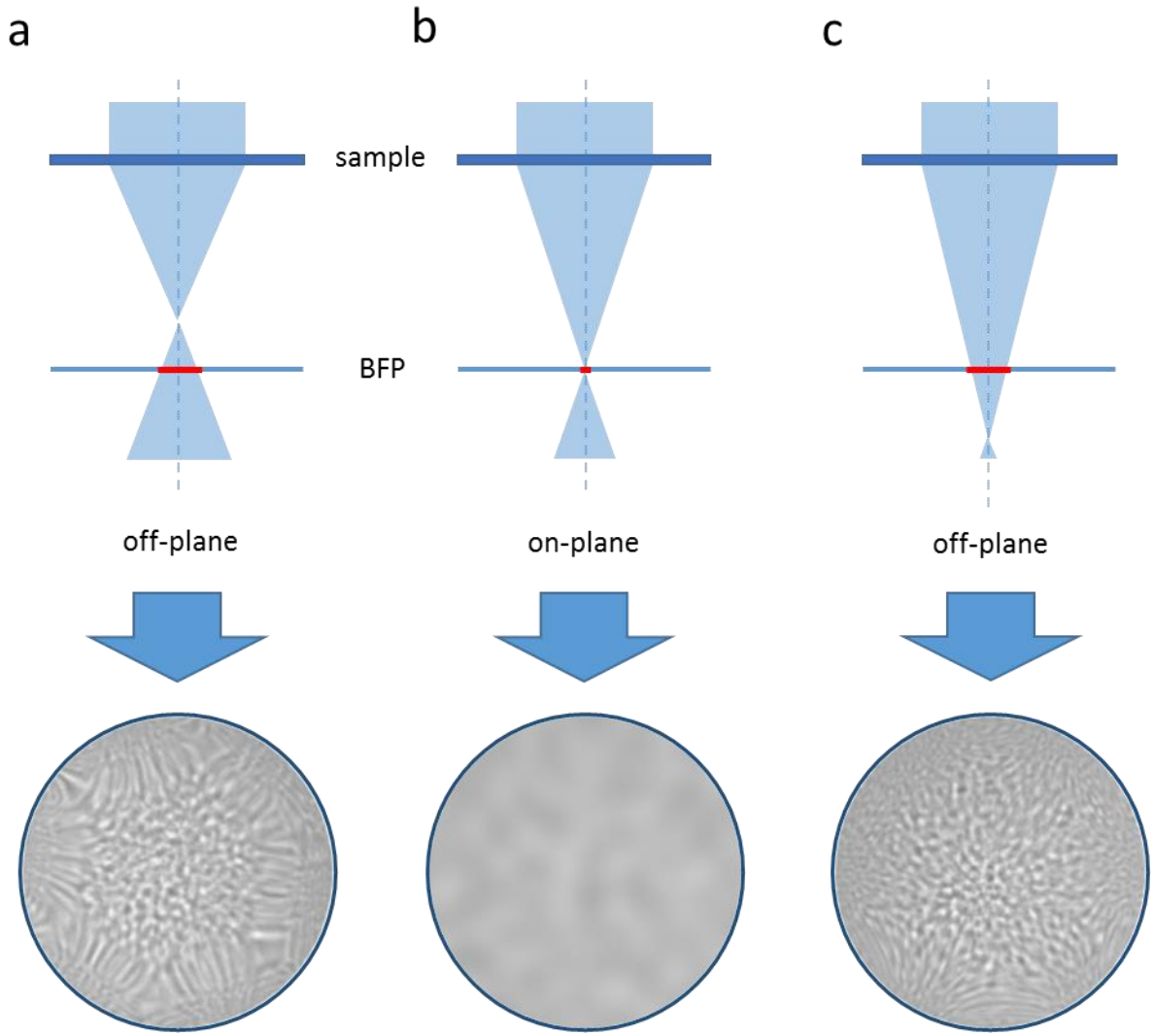

Figure 19. *Phase plate alignment of the on-plane condition. The beam crossover needs to lie on the same level as the Volta phase plate, situated at the back-focal plane (BFP). Shown here are misaligned crossovers (a and c) and the correct alignment (b). The respective Ronchigrams are depicted illustratively. Modified from [49].*

3.12. Subtomogram analysis

A single cryo-electron tomogram normally does not hold directly accessible high-resolution details due to the missing wedge and its low SNR from the minimal total electron dose expended for recording. However, if the tomogram, or a set of tomograms at identical recording conditions, contain numerous copies of the same object of interest these distinct densities can be identified and extracted *in-silico* as subvolumes from the overall three-dimensional reconstruction. The resulting stack of similar subtomograms with equivalent structures ("particles") in different orientations can now be aligned and averaged, which greatly enhances SNR and diminishes the effect of the missing wedge.

Subtomogram analysis therefore enables the three-dimensional high resolution imaging of macromolecular complexes directly from tomographic reconstructions. The process is iterative, as illustrated in *Figure 20*. Each cycle can be divided into four consecutive steps: Particle localization, extraction, alignment and classification.

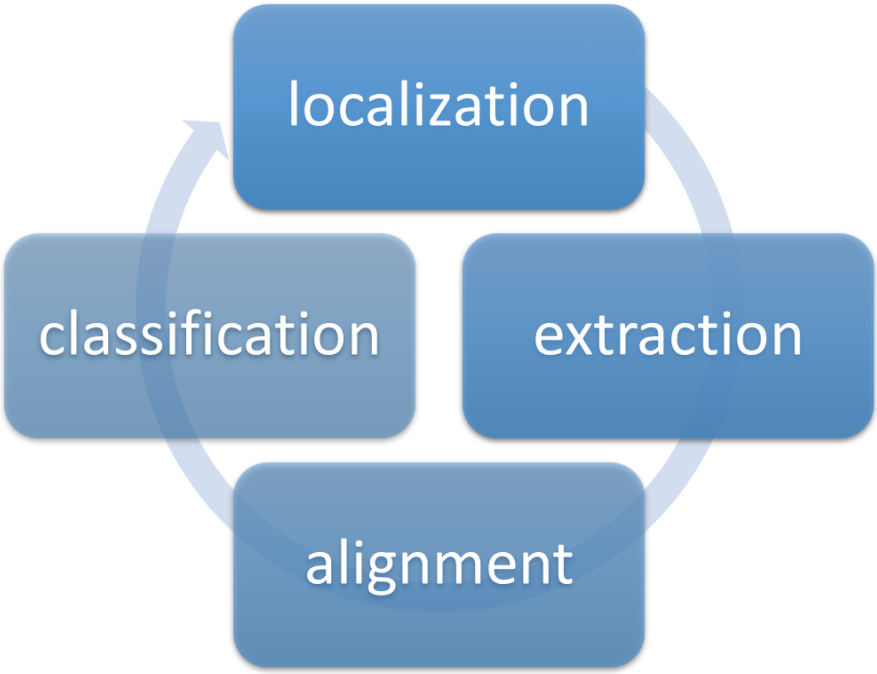

Figure 20. *Subtomogram analysis program flow. Clock-wise, from the top: Localization provides a map of subvolumes with high similarity to a common reference structure within the tomogram volume(s). Extraction of subvolumes along the coordinates determined in the previous step generates a stack of particles. Alignment of these particles by translation and rotation results in a structure with higher SNR after averaging. Classification of the aligned particles sorts the particle stack into different classes, according to their high resolution structural differences. The refined structure serves as the template for the next iteration.*

Localization of structurally similar features is performed via a pattern recognition algorithm that cross-correlates a reference template in different rotational orientations against the remaining volume [61]. This process produces a three-dimensional cross-correlation function (CCF). Its maxima indicate the positions of volumes with the highest similarity to the reference structure. The accuracy of the function increases with the SNR of the template.

Extraction of particles occurs by cutting out subvolumes from the center voxels of the maxima along the correlation coefficient map. This generates a stack of subvolumes with high similarity to the target of interest. Ideally, the object is recognized with high statistical significance, delineating true hits from false positives and negatives. Due to noise, however, this difference is much less defined and a matter of optimal thresholding.

Alignment is done in iterative cross-correlation of the particles against a common reference structure. Shift and rotation are taken into account to optimize the cross-correlation score. However, rotation has to be constrained to the experimentally sampled regions in order to prevent each particle's missing wedge (see 3.1) to become the dominant alignment feature [62].

Classification helps to resolve the structural heterogeneity of the specimen. Due to the low SNR, ordinary cross-correlation is not sufficient to determine high resolution structural differences of similar volumes, such a conformational changes in macromolecules. One solution to identify and account for such differences is a multi-reference refinement. This process iteratively cross-correlates all extracted particles against two or more reference structures. These are derived from the averaging of a random subset of particles from the same stack. Each individual particle is assigned to the reference with the highest cross-correlation score. The resulting classes are averaged to serve as the references for the next refinement iteration. With the cessation of particle migration the process ends [63]. Consequently, classification separates the particle set into groups with qualitatively similar structural features.

The aligned and averaged subvolume of a class serves as a refined template with higher SNR for the next cycle of the subtomogram averaging routine. This iteratively improves the resolution of the target of interest until it converges due to the various resolution-limiting factors, such as electron dose-induced minor structural damage. Subtomogram averaging thus constitutes a powerful method to obtain *in-situ* high-resolution structural information of large macromolecular complexes and their respective conformational states. For the subtomogram analysis of the gas vesicle structure, the routine had to be modified to address the very low SNR of the very small, individual GvpA monomers. This is specified in detail in the corresponding results chapter (see 4.3.6). Data processing was done in *TOM Toolbox* and a control test was performed via *Relion 1.4* [57, 64].

4. Results

4.1. Cryo-electron tomographic study of *H. salinarum* polar caps

The tomographic study of whole halobacterial cells was divided into two parts. Firstly, a series of preliminary observations was conducted on partially lysed vitrified *H. salinarum* cells. These examinations confirmed the location and frequent occurrence of the polar cap disk structure exclusively in less damaged cells and helped to assess the importance of high cell integrity for its structural resolution. The presence of an intact polar cap in flagellated cells was deemed essential for the recording of the complete intracellular motility system of *H. salinarum*. Secondly, after these initial observations, efforts were made to optimize both sample and recording conditions, in order to allow for more reproducible and comparable observations of the intact polar cap structure inside morphologically uncompromised cells.

4.1.1. Preliminary cryo-EM studies

Cryo-EM was performed as described in 3.5. The intracellular polar cap structure, as first observed by Kupper *et al*. (see 2.1.1), was initially not visible in single, short exposure micrographs [26]. Furthermore, it could only be discernibly recognized in cells that were morphologically still more or less intact. Compression of the cell poles through lysis or due to thin ice severely reduced the chance of observing this structure.

About 10 % of all reconstructed tomograms and long exposure micrographs met such conditions and showed a polar cap (see *Figure 21*). Some cell poles, however, were not flagellated despite the late growth stage at the point of vitrification. This prevented the opportunity to image the flagellar basal bodies and called for the conduction of motility assays in order to raise the relative number of motile – and thus flagellated – cells.

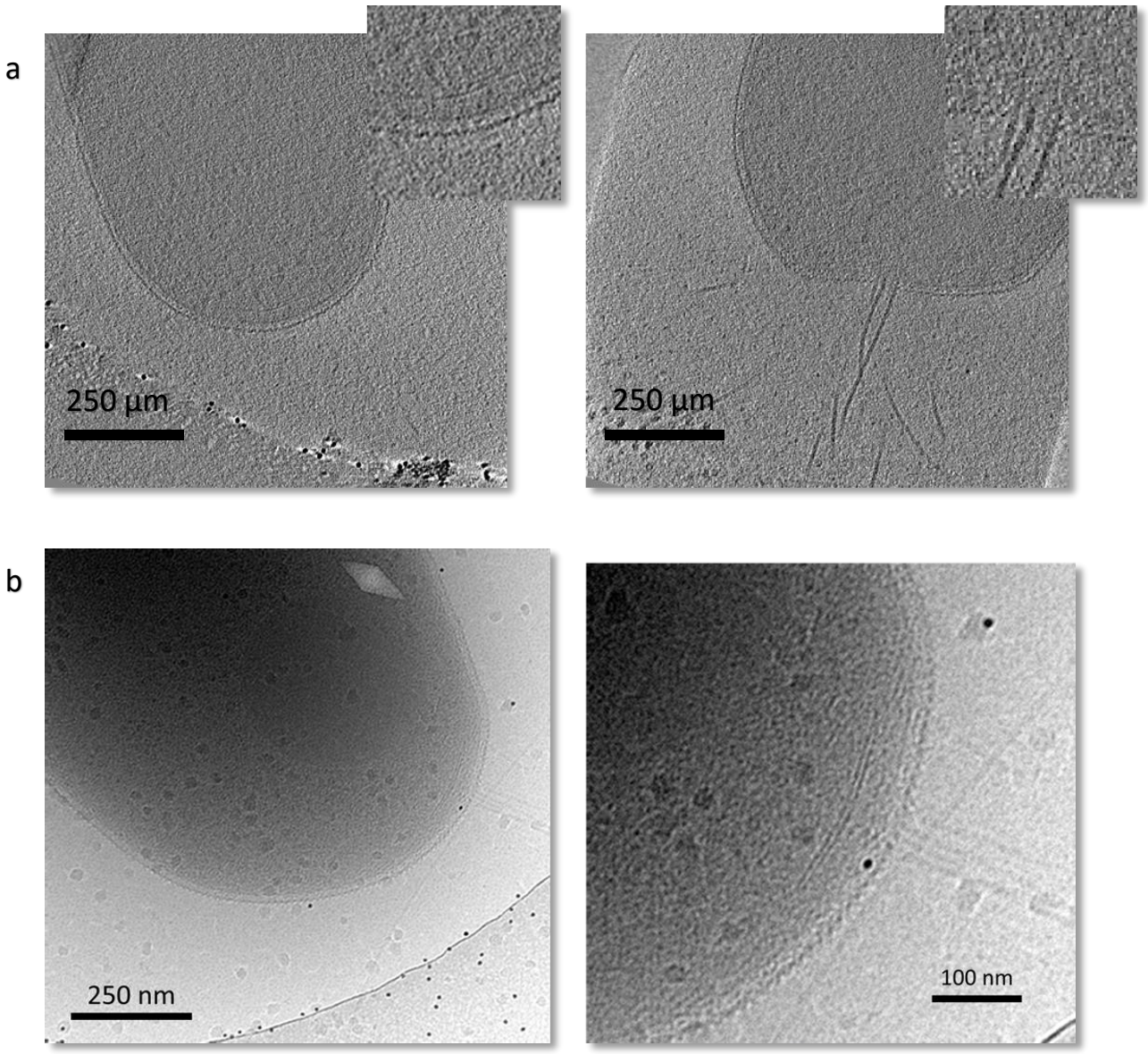

Figure 21. *Preliminary cryo-EM observations of damaged halobacterial cells at "low" salt conditions (2.0 M NaCl). Tomographic reconstructions of the cell poles (a) reveal the intracellular cap structure. Cell morphology is generally heavily compromised, and only about 10 % of cells showed a reliably identifiable cap structure.*

4.1.2. Swarm agar motility assays of *Halobacterium salinarum*

In order to ensure consistent flagellation of the vast majority of *H. salinarum* cells during the late exponential growth stage, motility assays were conducted to successively select for the most motile specimens for several generations.

The swarm agar motility assay described in 3.3 was repeated for ten successive generations. Each generation was split on a set of five swarm agar plates. Each time, the most motile cells were picked from the edge of the ring culture with the widest diameter. Additionally, cell movement in recorded video segments of individual cells was tracked to quantify and compare the motility of different swarm agar generations. A notable increase in motility was detected compared to their original S9 ancestry, by measurement of the ring diameters. Moreover, the cells contained a very high number of bipolarly flagellated cells towards their late exponential growth stage, as observed in cryo-EM samples (see *Figure 22*). The fifth and tenth generation strains (*SW#5* and *SW#10*), between which there was no additional observable increase in motility, were used throughout all further cell experiments.

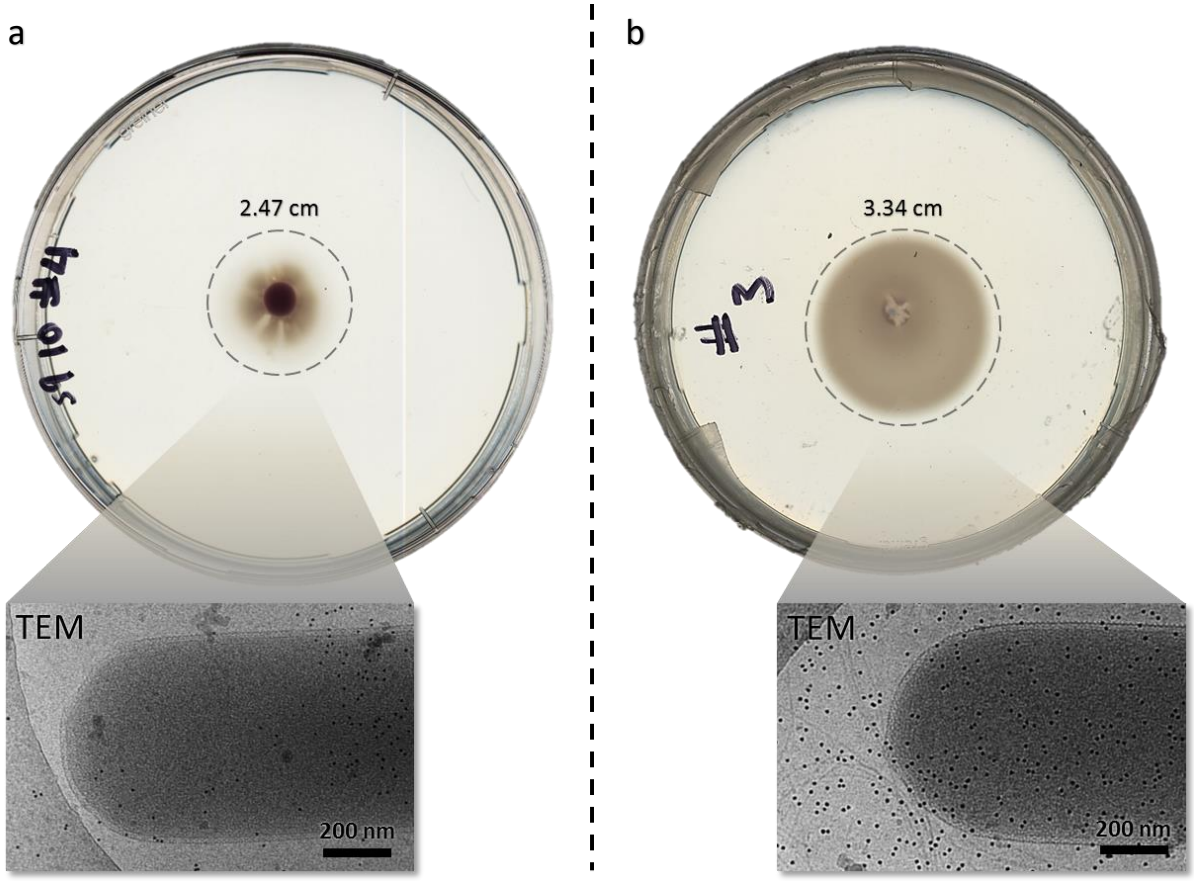

Figure 22. *Swarm agar motility assay of H. salinarum strain S9 (a) and SW#5 (b) after around 9 d of growth. To select for the highest motility, cells would be picked at the edge of the disk-shaped colony (indicated by circles) and inoculated to raise the next generation.*

4.1.3. Salt concentration tolerance pretrials

Cell integrity presented a major prerequisite for a more conclusive study of the intracellular motility apparatus of *H. salinarum* (see 4.1.1). This implicitly necessitated cryo-EM studies to be performed at very high salt concentrations and in ice that was sufficiently thick to avoid cell compression. These factors combined posed a considerable challenge. First and foremost, it was imperative to lower the surrounding NaCl concentration of the medium as much as the cells could tolerate. For this task, a number of growth experiments under different salt concentrations were conducted.

Cell cultures grown in FLCM at 4.3 M NaCl and 81 mM $MgSO_4$ to late logarithmic phase were dialyzed against ddH_2O. Samples of 50 µl were taken at regular time intervals. For each sample, the concentration of NaCl was measured osmometrically against a set of standard solutions containing differing NaCl concentrations from 0 – 4.3 M NaCl and 81 mM $MgSO_4$ (see 3.2). Additionally, cell morphology was examined under a light microscope. The total number of cells, as well as the relative amount of intact, semi-lysed and lysed cells were determined by counting the respective cell types within a series of light microscopy images of samples taken at different dialysis times. *Figure 23* illustrates the drastic increase in lysed cells as the concentration of NaCl decreased over time.

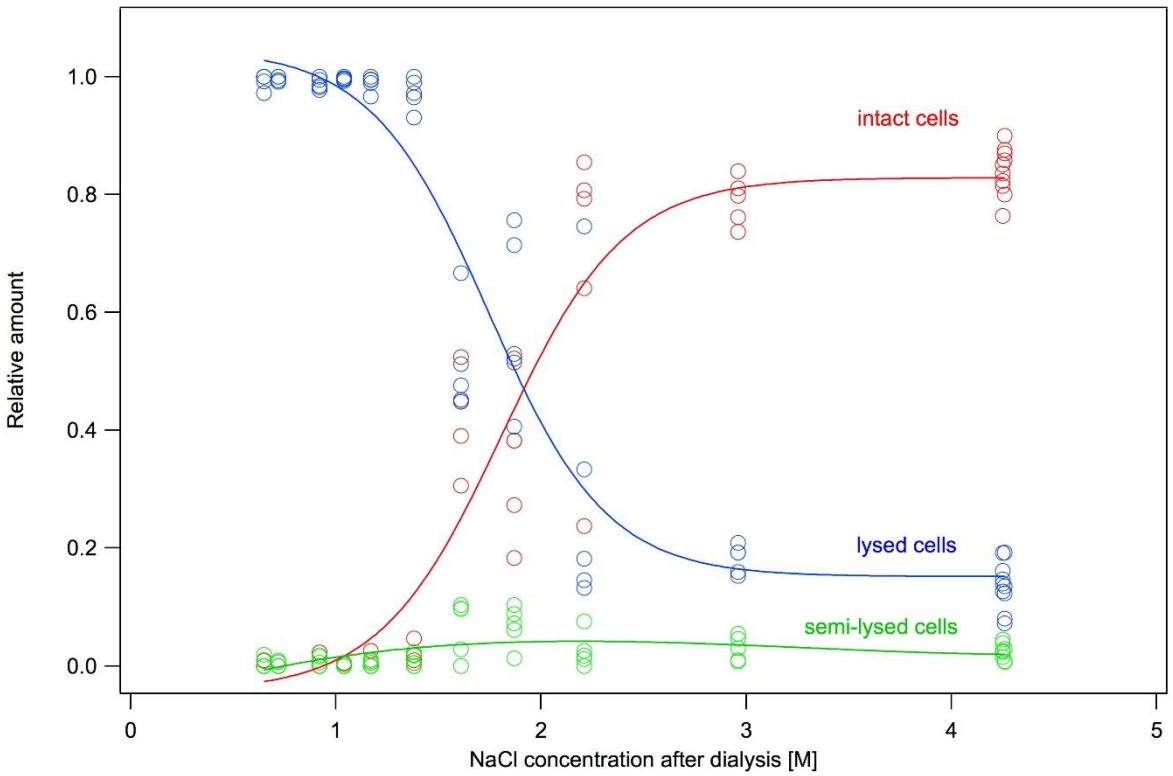

Figure 23. *Ratio of intact (red), damaged (green) and completely lysed (blue) cells against a decreasing NaCl gradient over the duration of the dialysis.*

By light microscopy, cells seemed mostly intact up to a minimal NaCl concentration of around 2.5 M. Concentrations below 2.0 M NaCl induced lysis of the majority of cells, which also showed severely decreased motility. Furthermore, even slightly decreasing the concentration of 81 mM $MgSO_4$, by controlled dilution with full culture media free of $MgSO_4$, vastly increased cell lysis. Mg^{2+} ions stabilize the integrity of the halobacterial S-layer [65, 66].

For a more extensive characterization of cell exposure to lower NaCl concentrations, three reserve were dialyzed against full medium containing 4.3 M NaCl, 3.5 M NaCl, 3.0 M NaCl, and 2.5 M NaCl respectively (see 3.2). Samples for each assay were taken after 72 h, which corresponded to the late exponential phase of the 4.3 M NaCl reference culture. The extracted samples were examined via light microscopy and, after vitrification (see 3.4), by cryo-electron microscopy.

The results of growth and cell integrity at different salt concentrations are summarized in *Figure 24 – Figure 27.* The growth rate of *H. salinarum* in 3.5 M NaCl FLCM seemed to be on par with that of cells raised at 4.3 M NaCl. Furthermore, cell integrity at 3.5 M NaCl was virtually indistinguishable from that of the reference cultures in both light microscopic, as well as transmission electron microscopic observations. Cells in medium with 3.0 M NaCl grew at an insignificantly slower rate, but light microscopic examination revealed a substantial amount of cells to show structural damage. While most of the cells had not lysed, their morphology was impaired. This was confirmed by transmission electron microscopy. At 2.5 M NaCl no cultures were able to reach OD600 values beyond 0.25, considerably lower than the typical levels of 0.9 – 1.2 of the 4.3 M NaCl reference. The majority of cells had lysed and the few remaining rod-shaped cells were notably deformed.

It was therefore decided to raise cell cultures intended for TEM experiments in 3.5 M NaCl FLCM by default and decrease salt concentrations to 3.0 M NaCl via dialysis immediately before vitrification. This approach resulted in mostly completely intact cells for cryo-TEM studies.

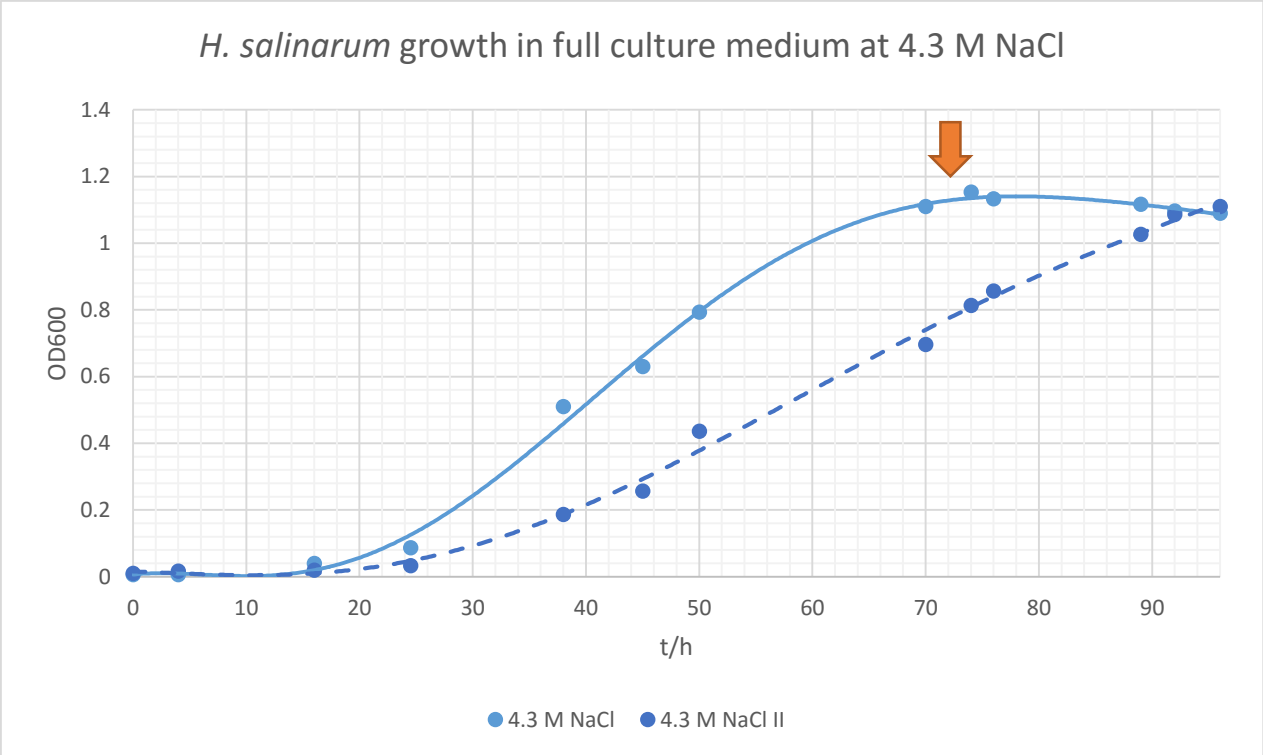

LM

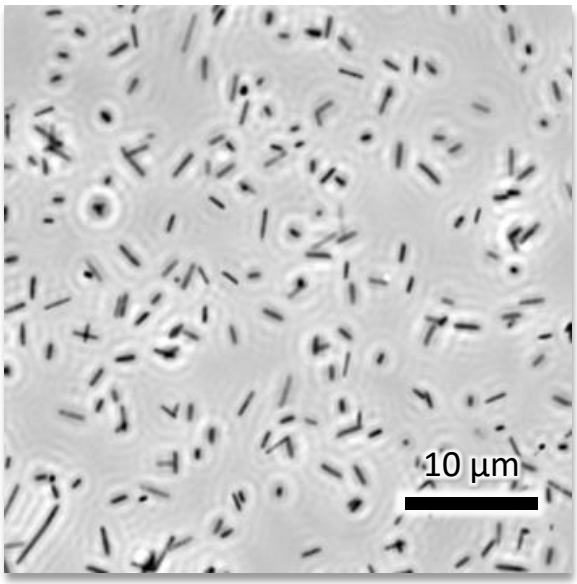

- cells seem intact
- around 80 – 90 % motile

TEM

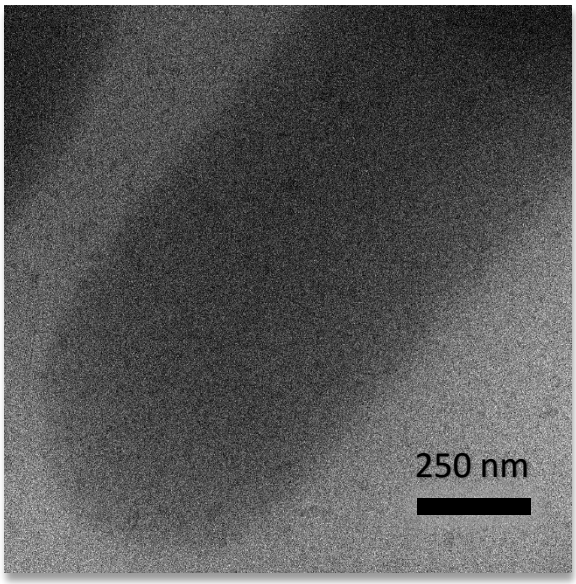

- very low contrast (direct detector)
- intracellular imaging not feasible
- cells are morphologically intact

Figure 24. *H. salinarum* growth at 4.3 M NaCl FLCM and morphological observations under light and electron transmission microscopy. The orange arrow indicates the time of sample extraction for subsequent LM and TEM examination.

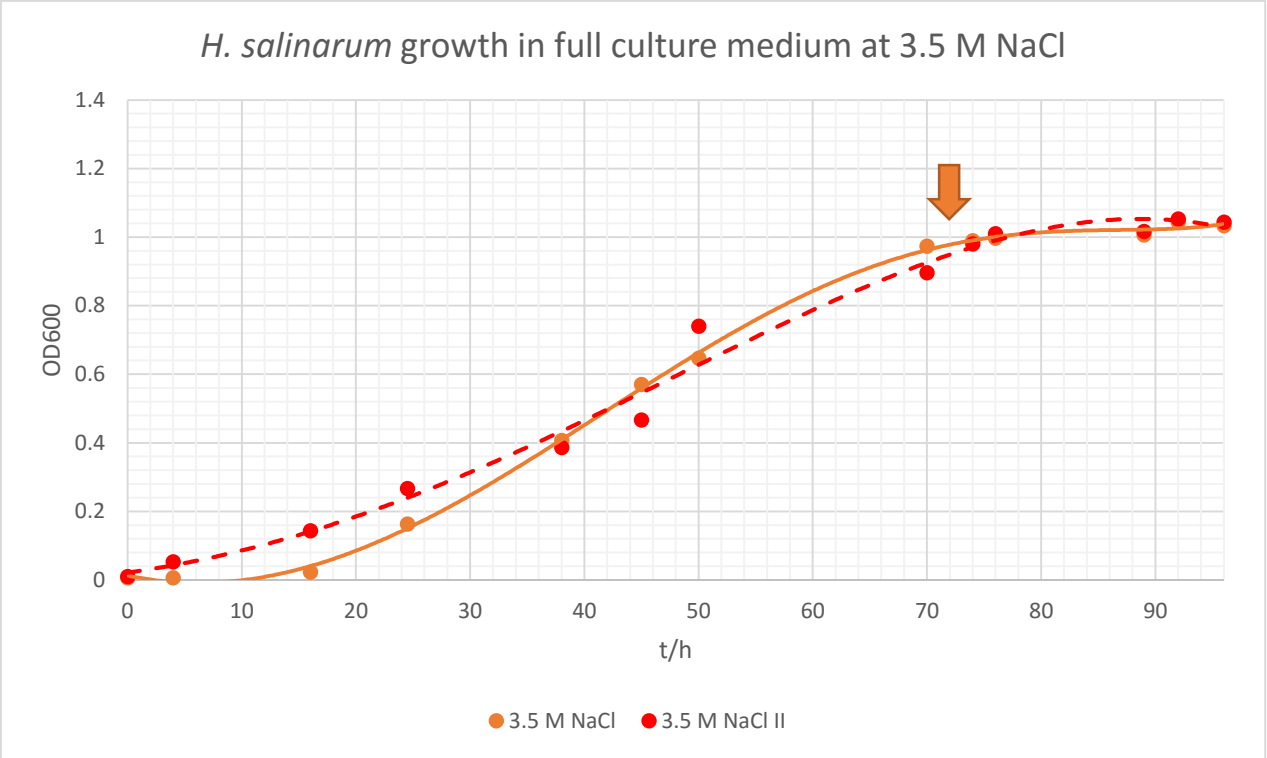

LM

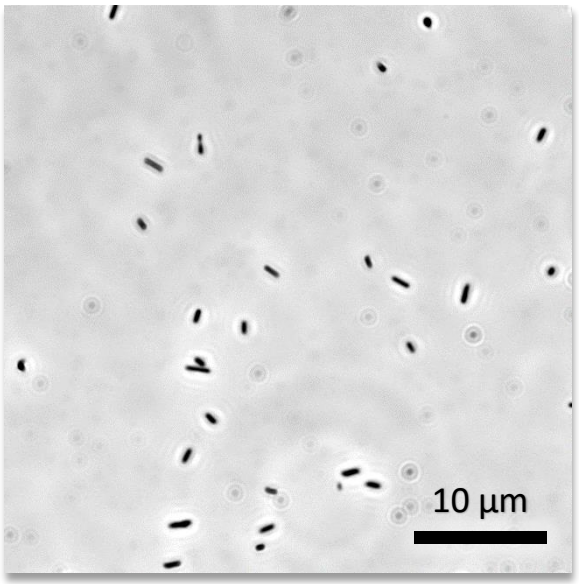

- cells seem intact
- around 80 – 90 % motile

TEM

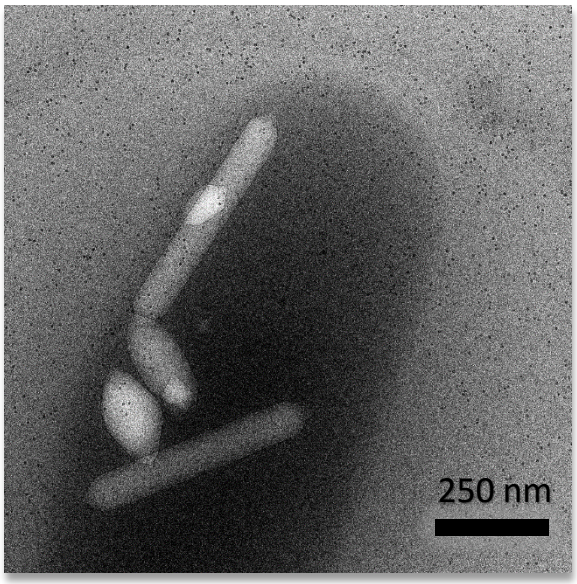

- low contrast (direct detector)
- intracellular imaging very difficult: only smaller cells and at very low SNR
- cells are morphologically intact

Figure 25. *H. salinarum* growth at 3.5 M NaCl FLCM and morphological observations under light and electron transmission microscopy. The orange arrow indicates the time of sample extraction for subsequent LM and TEM examination.

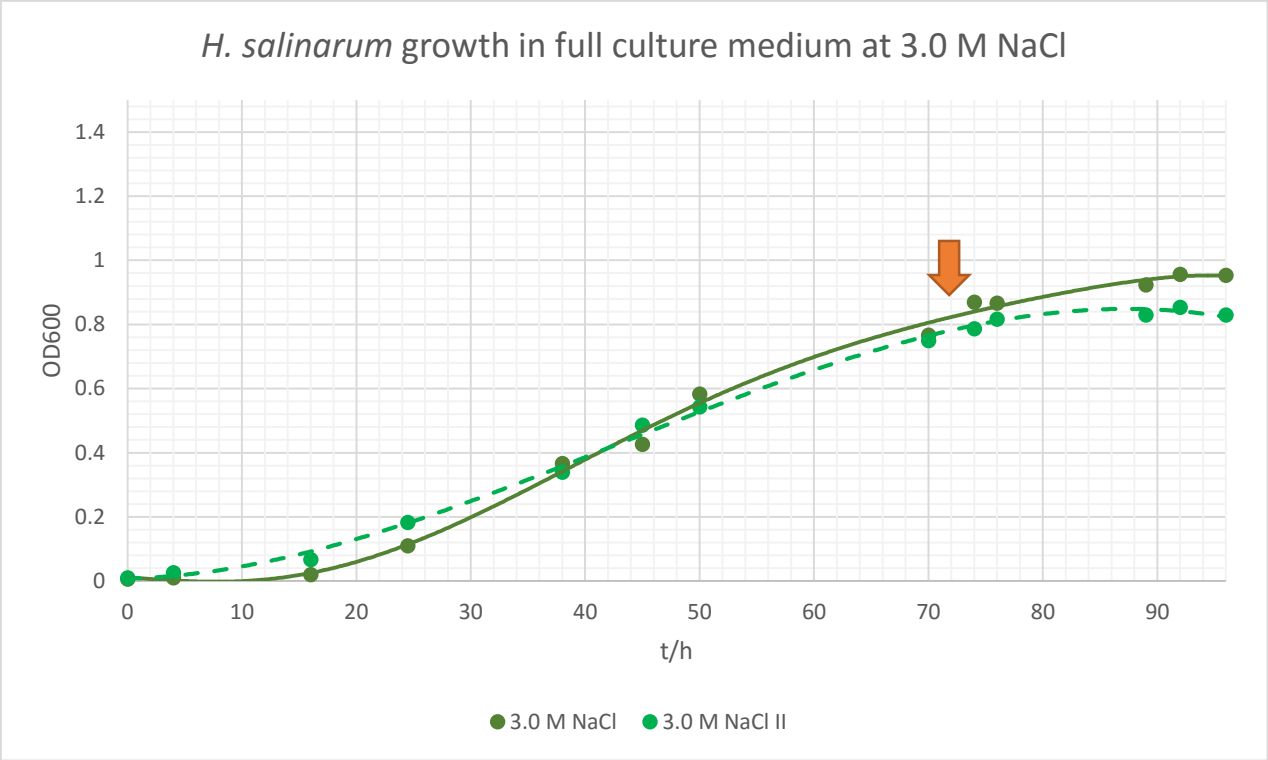

LM

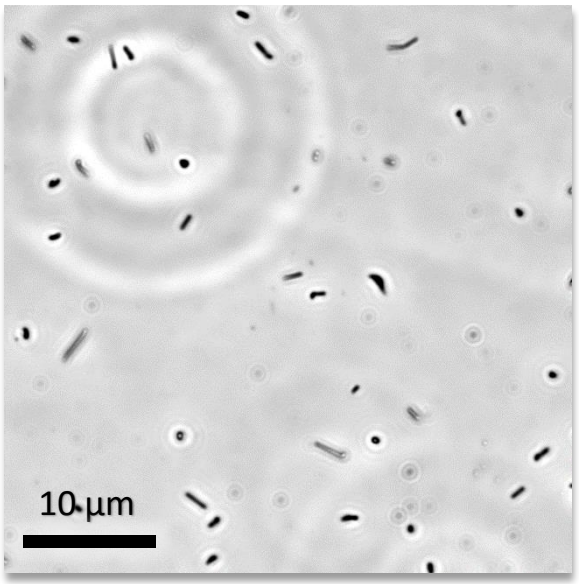

- < 10 % of cells show aberrant morphology
- < 30 % actively motile cells

TEM

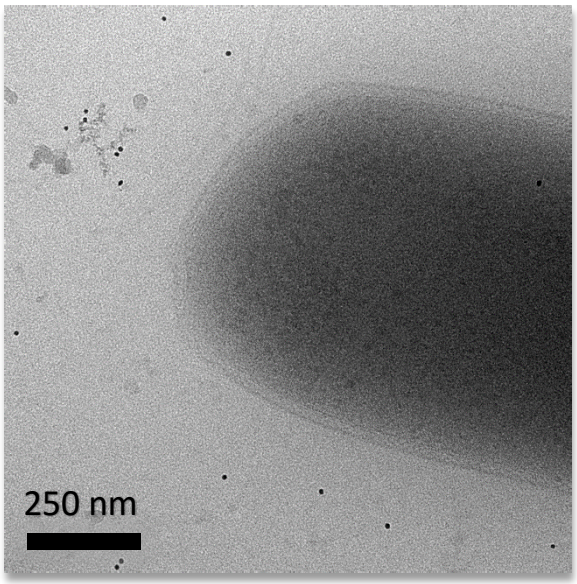

- low intracellular contrast
- intracellular imaging difficult: intact cells were still very dense
- many cells show morphological damage

Figure 26. *H. salinarum* growth at 3.0 M NaCl FLCM and morphological observations under light and electron transmission microscopy. The orange arrow indicates the time of sample extraction for subsequent LM and TEM examination.

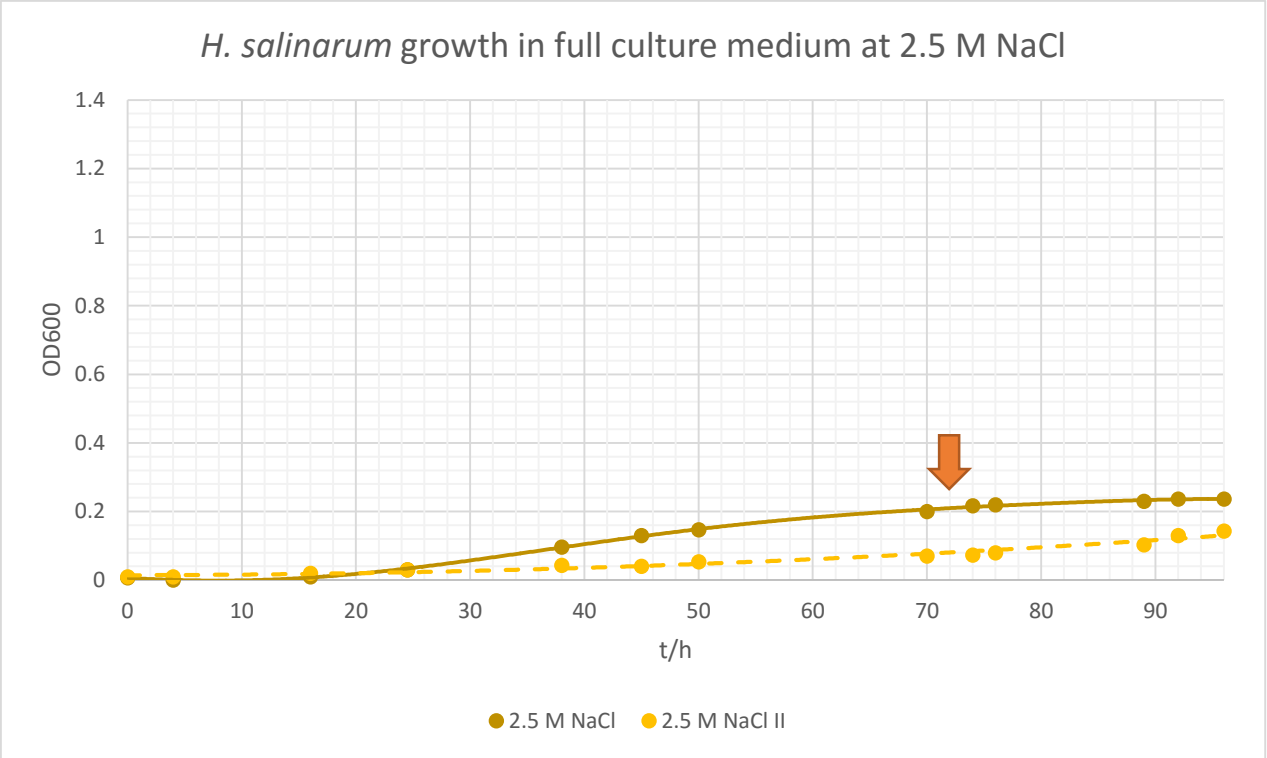

LM

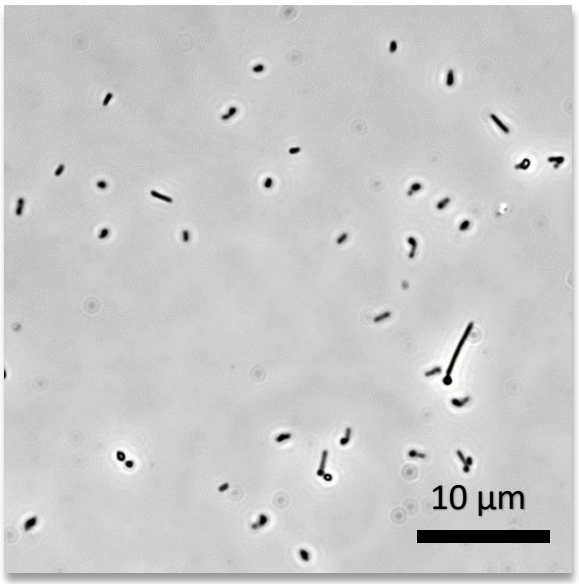

- > 80 % of cells show aberrant morphology
- < 10 % actively motile cells

TEM

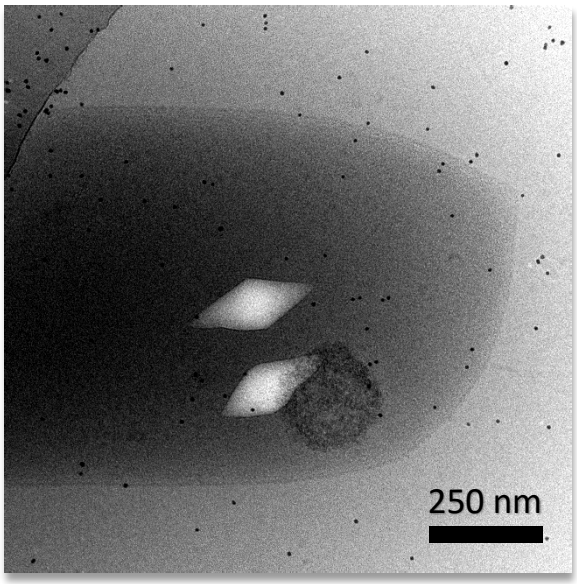

- improved contrast
- intracellular imaging of intact structures impossible due to cell lysis
- all cells show morphological damage

Figure 27. *H. salinarum* growth at 2.5 M NaCl FLCM and morphological observations under light and electron transmission microscopy. The orange arrow indicates the time of sample extraction for subsequent LM and TEM examination.

4.1.4. Optimization of the cell vitrification process

Optimally, a vitrified sample for the tomographic study of the motility system at the cell poles should contain a single consistent, homogenous layer of intact, flagellated cells. Cell density should be around one to three cells per carbon hole and overall ice thickness should just barely exceed the average cell diameter of 500 nm. To determine parameters that would reproducibly provide these conditions, a series of vitrification experiments was conducted. Cells grown in 3.5 M FLCM at different time lengths and various post-extraction incubation periods at room temperature were dialyzed to around 3.0 M NaCl medium salt concentration and vitrified manually and via the *Vitrobot*™ Mark IV[1]. For manual vitrification the blotting technique (from the side of the applied cell suspension or the backside) and duration were varied. *Vitrobot*-assisted vitrification additionally controlled different temperature and humidity settings. At least four sample grids for each setting were produced and subsequently screened via cryo-electron microscopy. Results are shown in *Table 1* and *Table 2*.

Table 1. Manual vitrification of H. salinarum cell suspensions in 3 M NaCl via cryo plunger at different parameters. Observed conditions detrimental to further processing are highlighted in red.

	sample 1 **4 grids**	**sample 2** **4 grids**	**sample 3** **8 grids**	**sample 4** **4 grids**
cell growth time at extraction	72 h	72 h	72 h	72 h
room-temperature incubation of cells	< 10 min	1 h	< 1 min	< 1 min
dialysis bath temperature	RT	RT	37 °C	37 °C
blotting technique	from front (cell side)	from front (cell side)	from front (cell side)	from front (cell side)
blotting duration	~ 3 s	~ 3 s	~ 3 s	~ 5 s
observations	**very few cells, varying ice thickness**	**very few cells, varying ice thickness**	**very few cells, varying ice thickness**	**very few cells, varying ice thickness**

[1] FEI, Eindhoven, The Netherlands

	sample 5 **4 grids**	**sample 6** **4 grids**	**sample 7** **6 grids**	**sample 8** **4 grids**
cell growth time at extraction	72 h	72 h	72 h	72 h
room-temperature incubation of cells	< 10 min	1 h	< 1 min	< 1 min
dialysis bath temperature	RT	RT	37 °C	37 °C
blotting technique	from back of grid	from back of grid	from back of grid	from back of grid
blotting duration	~ 3 s	~ 3 s	~ 3 s	~ 5 s
observations	thick layer of cells, **varying ice thickness**, mostly **too thin**	2 of 4 grids with good cell layer, **varying ice thickness**	**few cells** on the grids, very thick, **uneven ice**	**few cells** on the grids, mostly thick, **uneven ice**

	sample 9 **8 grids**	**sample 10** **8 grids**	**sample 11** **4 grids**	**sample 12** **4 grids**
cell growth time at extraction	50 h	92 h	72 h	72 h
room-temperature incubation of cells	< 10 min	< 10 min	1 h	1 h
dialysis bath temperature	RT	RT	RT	RT
blotting technique	from back of grid	from back of grid	from back of grid	from back of grid
blotting duration	~ 3 s	~ 3 s	~ 1 s	> 10 s
observations	healthy but **compressed cells**, mostly unflagellated, thin ice	many lysed, flagellated cells, adequate density, **thin but uneven ice**	**very thick ice**, no cells visible	no cells, carbon surface damage

Choosing the late exponential phase for extraction (after around 72 h), yielded healthy, flagellated cells. Dialyzed, vitrified cells extracted after 50 h seemed to be intact throughout but mostly lacked flagellation. Cells extracted after 92 h seemed less robust against the induced stress by dialysis and were mostly severely damaged after vitrification. An incubation period of 1 h at room temperature seemed to be beneficial to cell integrity for dialysis. Heating of the dialysis bath to 37 °C, the growth temperature of the cell cultures, did not improve the cells' structural integrity.

Manual vitrification of the hypersaline samples needed to be performed by blotting from the back, as blotting from the front would otherwise remove most of the cells. Nevertheless, the inherently imprecise manual vitrification procedure generally resulted in a very thin and uneven layer of amorphous ice and lead to compression of the cell bodies. As a consequence, results were highly irreproducible, and improving this process proved to be time-consuming. Utilization of the *Vitrobot* for the plunge-freezing of samples allowed for a more systematic approach and delivered slightly more consistent and uniform vitreous samples. All test samples were grown for 72 h, incubated for 1 h and dialyzed against 3.0 M NaCl at room temperature. Blotting was performed from both sides. The results are compiled in *Table 2*.

Table 2. *Vitrobot-assisted vitrification of H. salinarum cells at different parameters. Marked in green are the vitrification conditions that resulted in a good cell distribution with appropriately thick ice.*

	sample 1 **4 grids**	**sample 2** **4 grids**	**sample 3** **4 grids**	**sample 4** **4 grids**
***Vitrobot* chamber temperature**	RT	RT	RT	RT
***Vitrobot* chamber humidity**	0 %	0 %	0 %	0 %
blotting strength	"3"	"5"	"10"	"15"
blotting duration	3 s	3 s	3 s	3 s
observations	good cell distribution, ice very thick	good cell distribution, ice too thick	cells mostly on carbon, overall thick ice	mostly damaged cells on carbon, thick ice

	sample 5 **4 grids**	**sample 6** **12 grids**	**sample 7** **6 grids**	**sample 8** **4 grids**
***Vitrobot* chamber temperature**	RT	RT	RT	RT
***Vitrobot* chamber humidity**	100 %	100 %	100 %	100 %
blotting strength	"3"	"5"	"10"	"15"
blotting duration	3 s	3 s	3 s	3 s
observations	very thick ice, most cells not observable	good cell distribution, thick ice	many broken cells, aggregation, thick ice	very few cells in carbon holes, mostly broken, thick ice

	sample 9 **8 grids**	**sample 10** **8 grids**	**sample 11** **4 grids**	**sample 12** **4 grids**
***Vitrobot* chamber temperature**	RT	RT	RT	RT
***Vitrobot* chamber humidity**	100 %	100 %	100 %	100 %
blotting strength	"5"	"5"	"5"	"5"
blotting duration	5 s	7 s	9 s	11 s
observations	very good cell distribution, ice medium thick (no cell compression)	good cell distribution, some cells compressed, overall thin ice	many cells compressed, thin ice	very few cells remaining, very thin ice, carbon holes without ice

While sample 9 seemed promising, and yielded grids of comparable quality (see *Figure 28*), later cell vitrification results remained largely inconsistent in terms of cell density distribution and local ice thickness. The outcome varied even for numerous samples processed from the same culture. For a higher throughput of reliably good samples, further optimizations were required but could not be met due to time constraints.

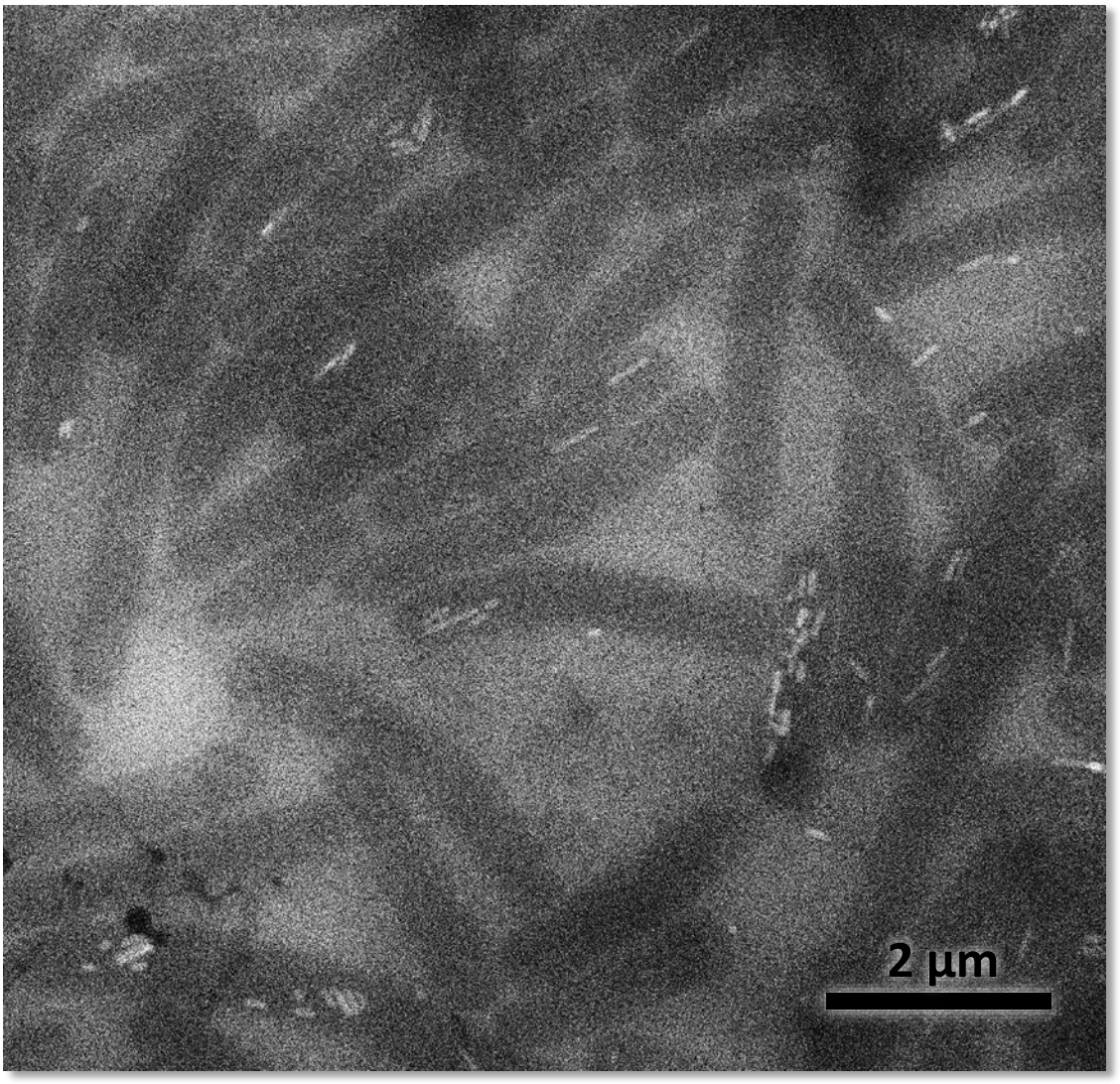

Figure 28. *Vitrified cells at 3.0 M NaCl FLCM after attempts to optimize the vitrification process. The use of a Vitrobot lead to higher consistency for creating thicker and slightly more homogenous ice compared to manual blotting. This was important to prevent cell compression. The low SNR now required post-vitrification thinning. The rate of reproducibility of samples with optimal cell distribution and an ice thickness of just over 500 nm remained altogether low.*

4.1.5. Focused ion beam milling of vitrified cell samples

As the average cell diameter of 500 nm did not allow much thinner ice for vitrified samples without severe deformation of the cells, sectioning of the specimen became a necessity (see *Figure 29*). For this purpose, focused ion beam (FIB) milling was chosen over traditional cryo-sectioning to avert mechanical compression artifacts. Due to the small size of the prokaryotes the targeting of individual cells was infeasible. Instead, a 15 – 20 µm wide wedge pattern was milled into the sample at a low angle. Under optimal conditions, a vitreous cell samples prepared in the previous step (see 4.1.4) had an average cell distribution of one to two cells per carbon hole. The wedge covered 5 – 6 carbon holes and thus presented opportunity for the recording of any favorably oriented cells along the thin edge of the milled region.

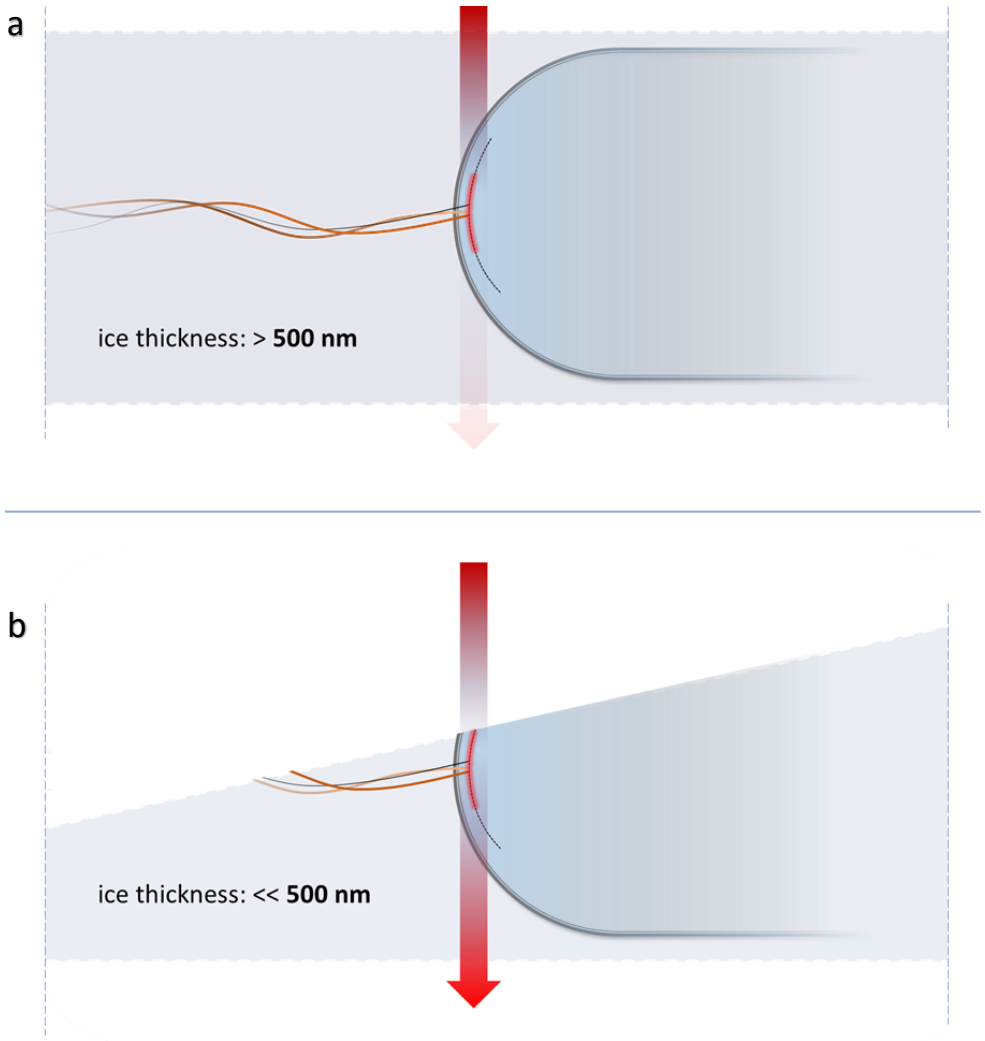

Figure 29. *FIB milling of vitrified halobacterial cells illustrated. The high salt concentrations combined with the overall thick ice of the vitreous sample significantly reduce contrast in particular within the cells (a). In order to permit the imaging of uncompressed intracellular components with sufficient contrast, the samples required thinning. A wedge pattern is milled into the sample, exposing cells close to the thin edge as potential targets for tomography (b).*

Previously vitrified whole-cell samples were mounted on autogrid cartridges, inserted into a FIB shuttle, while kept below -180 °C throughout, and mounted on the cryostage of the DB-FIB (see 3.6). A wide wedge was milled into the specimen, spanning over several carbon holes (see *Figure 30*).

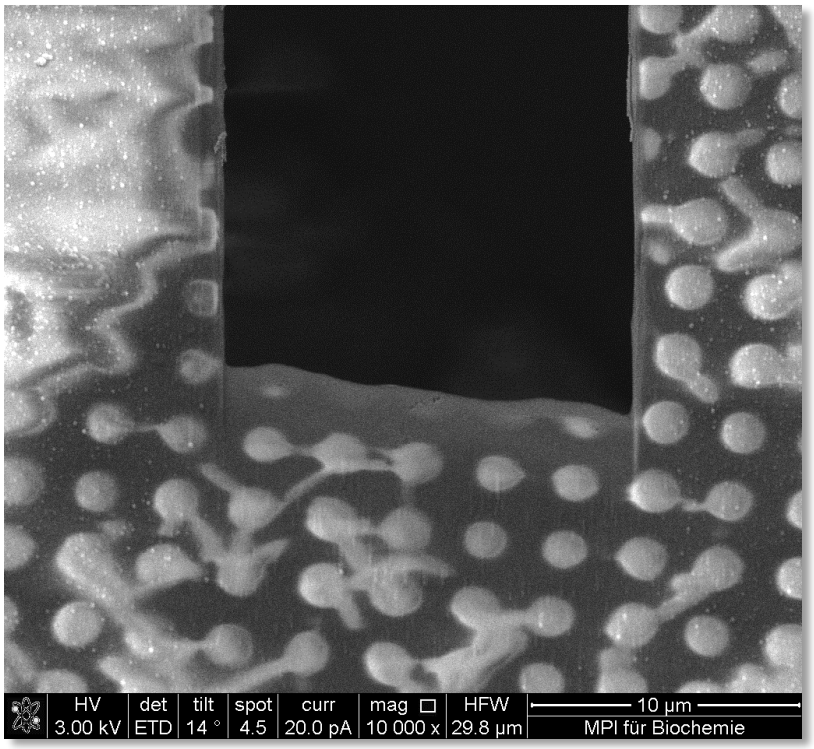

Figure 30. *Focus ion beam-milled wedge through frozen halobacterial cells as seen in the SEM. A wide wedge was milled through the sample, covering several of the 2 µm carbon holes. Some cells protruded through the surface and showed in the SEM. Mostly, the wedges are cut without such visual cues.*

Quality validations of the prepared samples could only be done via TEM. During transfer in and out of the FIB, samples sometimes accumulated light surface contamination due to temporary exposure to humidity, insufficient cooling or other, unknown factors. In combination with the inconsistent sample properties resulting from the vitrification process (see 4.1.4), this significantly reduced the number of samples available for subsequent cryo-electron tomography, leaving only eight out of a total number of 60 milled grids. Tomography-suitable targets, i.e. any cell poles encased in sufficiently thin ice along the edge of the FIB-milled wedge of the sample, could not be found in either of the eight remaining grids. As *Figure 31* demonstrates, the samples were contaminated or did not contain the proper motif. Further optimizations were necessary to increase the throughput of higher quality samples. These had to be deferred in favor of other subprojects.

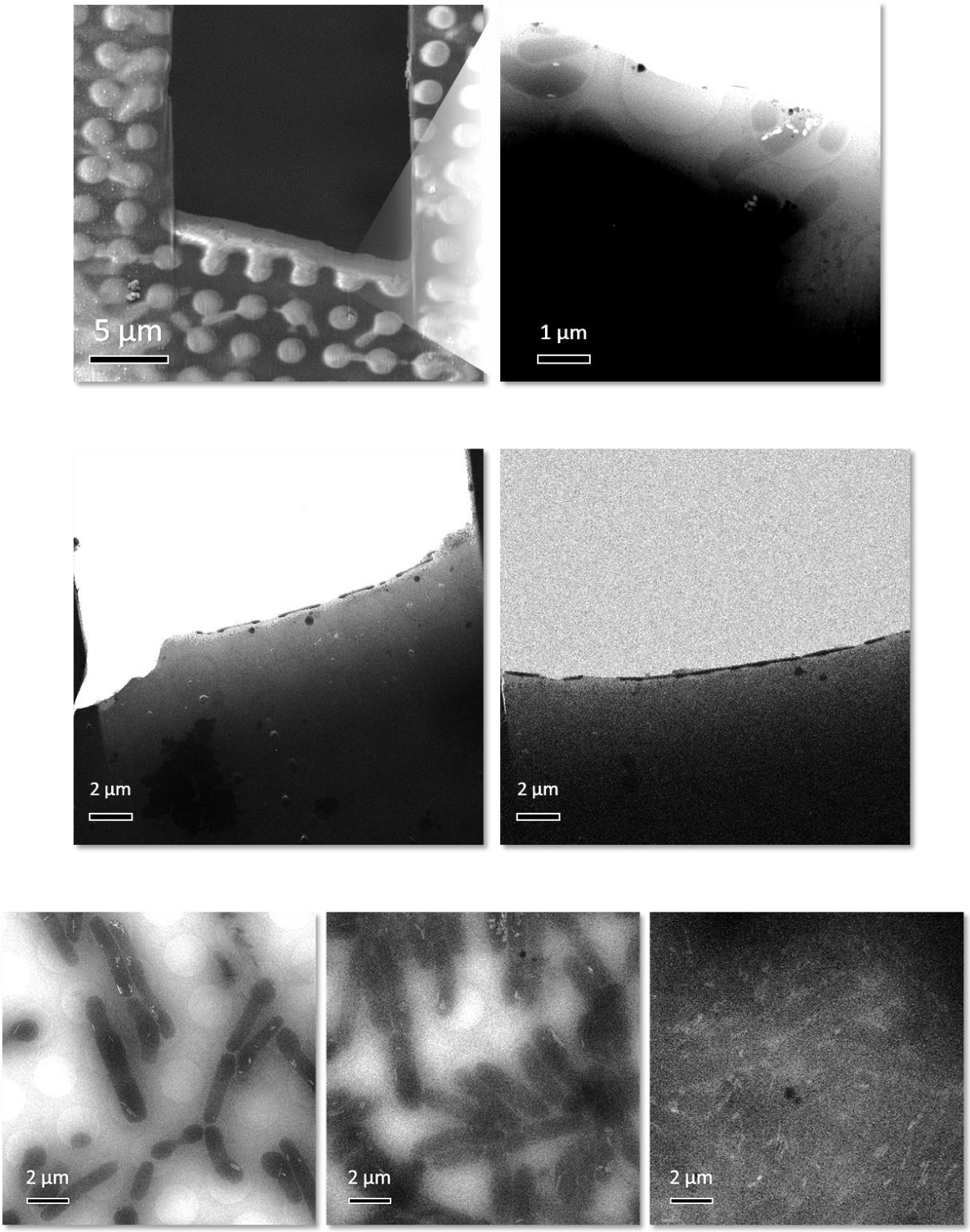

Figure 31. *Upper left side: SEM picture of a FIB-milled wedge. Upper right side: The same wedge under cryo-EM examination. No intact cell pole regions were properly aligned to be suitable for tomography. Middle row: Two wedges that did not contain any cells. The left wedge also exhibits severe surface contamination. Bottom row: Inhomogeneous cell distribution on three different grids from the same preparation, each carrying 4 µl of the vitrified cell culture.*

4.2. Localization of the flagellar growth site

Attempts to localize the flagellar growth site required the production of Fla-specific antibodies (see 3.7). To obtain those, chickens were immunized against previously isolated flagella. They produced IgY, which accumulated in the egg yolk in high concentration. They were biochemically purified. To assess the binding specificity of the concentrated IgY to a suspension of isolated flagella, an ELISA was performed (see 3.7.2 and *Figure 32*).

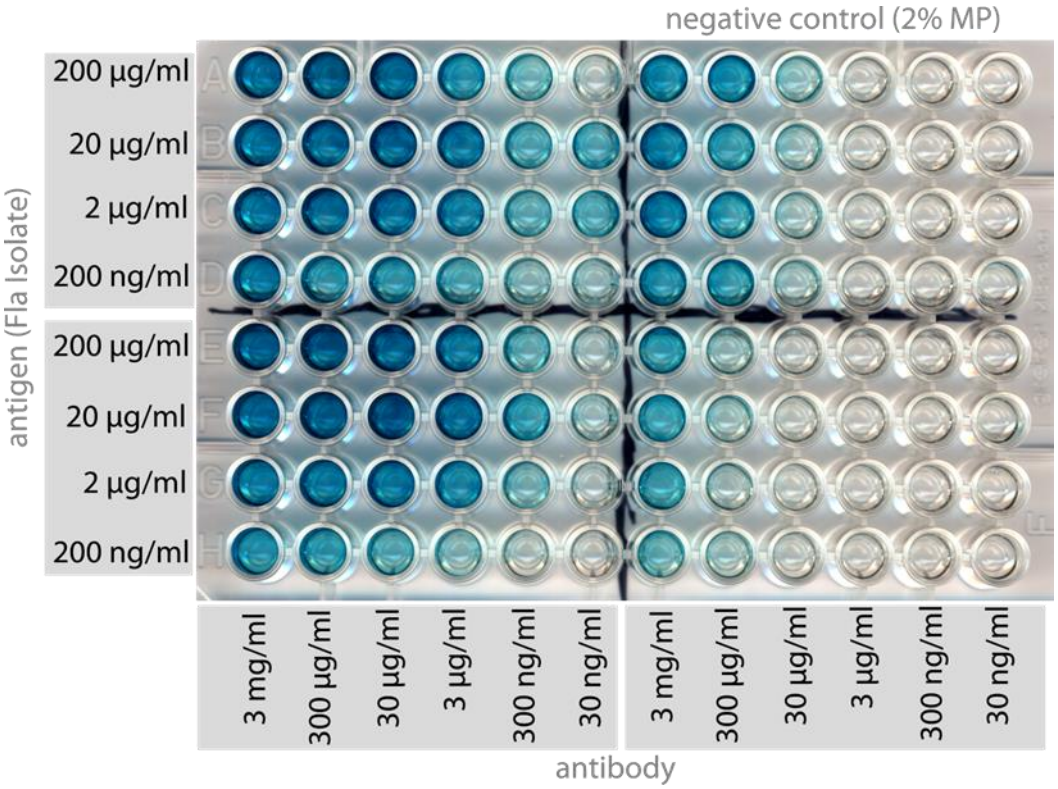

Figure 32. *ELISA for the determination of Fla-binding specificity of previously isolated IgY antibodies. The left columns (1 – 6) show bound IgY in a series of ten-fold dilutions from 3 mg/ml to 30 ng/ml. Rows A – D bound IgY isolated from one chicken, while rows E – H bound IgY from the second chicken. The wells were previously coated with antigen, isolated flagella (see 3.7.1), in a ten-fold line-wise dilution series ranging from 200 µg/ml to 200 ng/ml. The right columns (6 – 12) were coated with milk powder and show unspecific cross-reactions of IgY at equimolar concentrations.*

In transmission electron microscopic observations of IgY-incubated flagella with gold-coated anti-IgY secondary antibodies (see 3.7.2), gold beads were most frequently found in the direct vicinity of flagella, as well as lysed intracellular debris, as demonstrated in *Figure 33*. However, the overall distribution of gold labels was sparse, despite the very high concentrations of IgY and secondary labeling antibody.

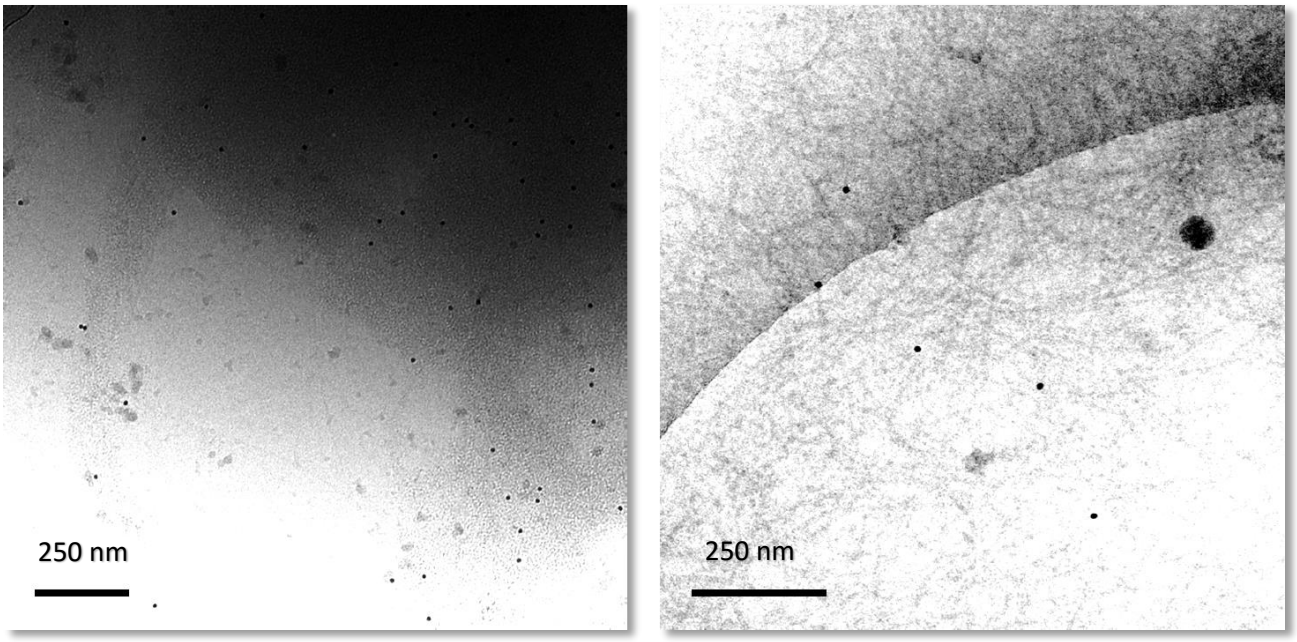

Figure 33. *Detection of IgY via a gold-conjugated donkey-anti-chicken secondary antibody under cryo-electron microscopy. The 12 nm gold beads (visible as black dots) are mostly located near flagella and lysed, intracellular components.*

The antibody bound to the cells, as determined by the localized fluorescence signal emitted by FITC (see *Figure 34*). However, the signal extended to the cell body, drowning out any signal potentially stemming from flagella-bound IgY. The cells were also mostly completely immobilized, due to the encumbrance by the accumulation of surface-bound IgY.

This outcome rendered further labeling assays futile, as a precise localization of the growth site would require a significantly higher specificity for Fla-distinctive epitopes.

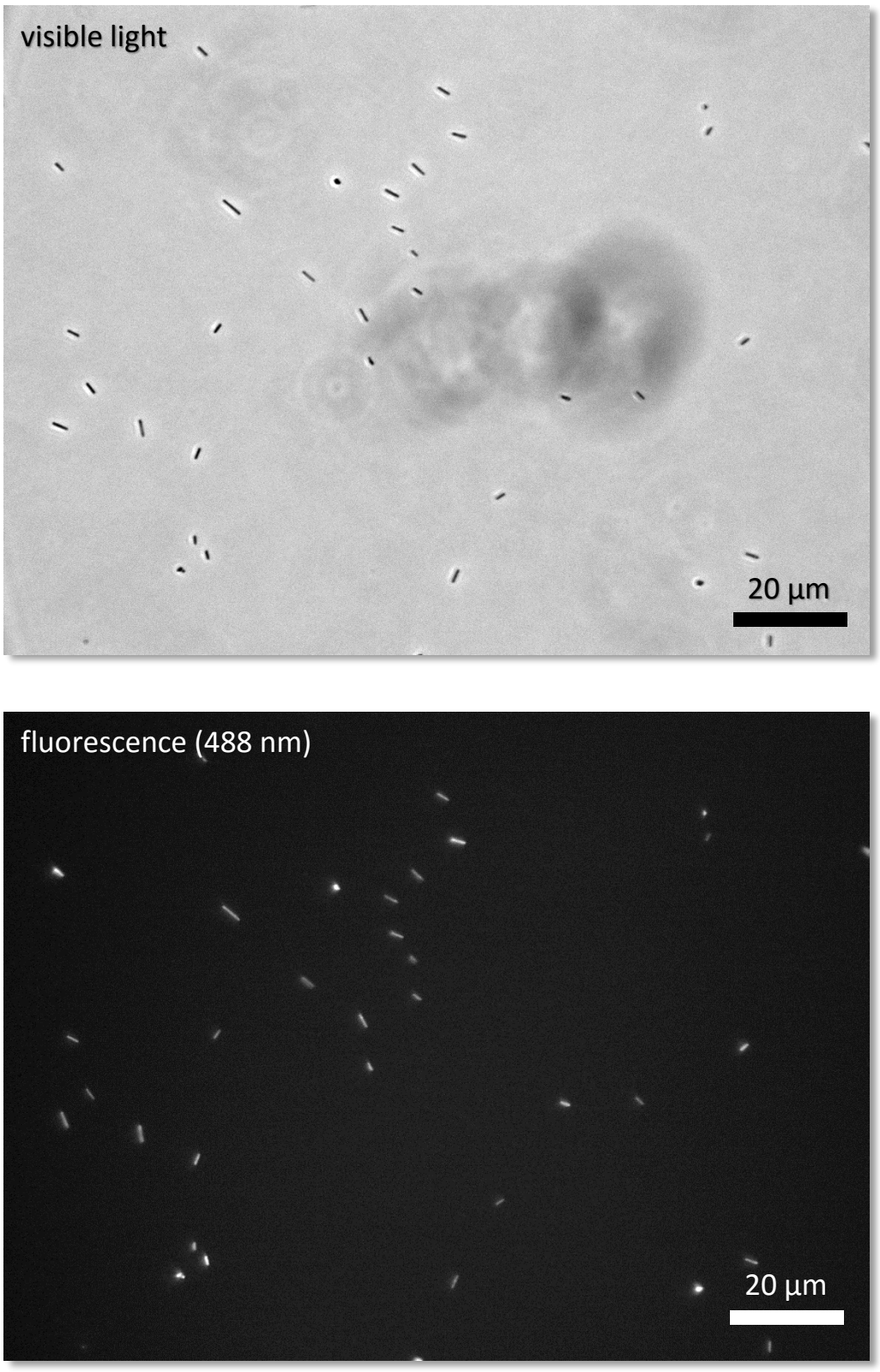

Figure 34. *IgY-FITC-conjugated antibody labeling of Halobacterium salinarum cells in native, hypersaline conditions. The antibody binds to the cells, as seen by the localized fluorescence signal under laser light of 488 nm (below). However, it completely immobilizes the cells and seems to exhibit significant cross-reactivity to epitopes on the surface of the cell body.*

4.3. Study of the gas vesicle substructure

4.3.1. Mass spectrometry of solubilized wild type gas vesicles

Two halobacterial wild type gas vesicle isolates were analyzed via LC-ESI-MS (see 3.8.1). One was washed with H_2O twice, the other was washed four times before solubilization. Only the first sample sufficiently solubilized in the formic acid, as the UV absorption spectrum of the second sample did not reveal notable protein peaks following the solvent front. Mass spectrometry confirmed the presence of a distinct 8,240 Da mass in both samples (see 2.1.2). With a mass difference of 132 Da, this corresponds well to the 8,372 Da GvpA2 [1] without its N-terminal methionine (149 Da), which is hydrolyzed (18 Da) cotranslationally [67]. For the first sample, the corresponding UV absorption peak was also well defined and notably big, compared to other absorption peaks, making it the main constituent in spite of the assumed partial solubilization of the protein. The presence of GvpA2 in both samples is therefore very likely. A second peak, measuring 42,527 Da, was detected only in the first sample, which was washed only two times. This exceeds the mass of a Met-cleaved GvpC2[2] by 266 Da. *Figure 35* shows a comparison between the detected masses and their respectively expected Gvp proteins.

Detected mass: 8,240 Da

Comparison: GvpA2[1] (8,372 Da – Met + H_2O = 8,241 Da; Δm ≈ +1 Da):

MAQPDSSSLA EVLDRVLDKG VVVDVWARIS LVGIEILTVE ARVVAASVDT
FLHYAEEIAK IEQAELTAGA EAPEPAPEA

Detected mass: 42,527 Da

Comparison: GvpC2[2] (42,392 Da – Met + H_2O = 42,261 Da; Δm ≈ +266 Da)

MSVTDKRDEM STARDKFAES QQEFESYADE FAADITAKQD DVSDLVDAIT
DFQAEMTNTT DAFHTYGDEF AAEVDHLRAD IDAQRDVIRE MQDAFEAYAD
IFATDIADKQ DIGNLLAAIE ALRTEMNSTH GAFEAYADDF AADVAALRDI
SDLVAAIDDF QEEFIAVQDA FDNYAGDFDA EIDQLHAAIA DQHDSFDATA
DAFAEYRDEF YRIEVEALLE AINDFQQDIG DFRAEFETTE DAFVAFARDF
YGHEITAEEG AAEAEAEPVE ADADVEAEAE VSPDEAGGES AGTEEEETEP
AEVETAAPEV EGSPADTADE AEDTEAEEET EEEAPEDMVQ CRVCGEYYQA
ITEPHLQTHD MTIQEYRDEY GEDVPLRPDD KT

Figure 35. *Detected masses in two samples analyzed by LC-MS compared to their potentially corresponding Gvp proteins with their masses and amino acid sequences.*

[1] http://www.uniprot.org/uniprot/P08959
[2] http://www.uniprot.org/uniprot/P24574 (locus VNG_6031G)

While post-translational modifications and/or formylation within the relatively harsh solvation conditions of 6.5 M formic acid could likely account for the additional mass, no unambiguous conclusions could be drawn. In the second sample, no mass peaks potentially corresponding to any GvpC variants were identified. The absence of GvpC in detectable quantities after four washing steps is in agreement with the gas vesicle purification protocol established by Strunk *et al*. [33]. Other putative structural proteins, such as GvpJ and GvpM, were not found in either sample. This does not categorically exclude their potential presence within the envelope, but suggests their stoichiometric contribution as building blocks is significantly lower than that of GvpA and GvpC.

The summed intensities of all mass spectral peaks (total ion current, TIC), the 214 nm UV absorption peaks, and their corresponding, deconvoluted mass spectra are shown exemplarily for both sample types in *Figure 36* (*A*, *B* and *C*) and *Figure 37*, respectively.

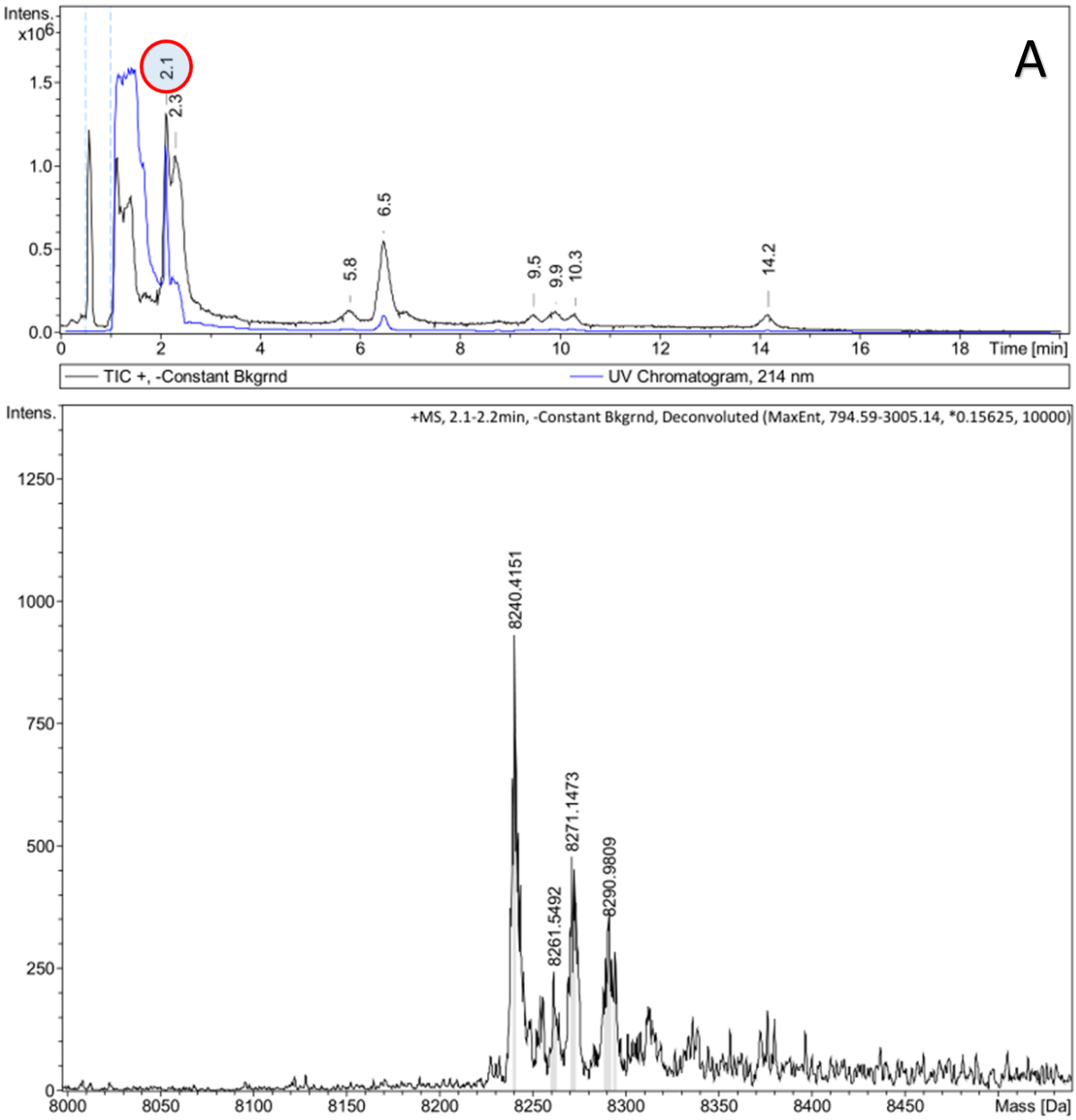

Figure 36 A. *LC-MS analysis of gas vesicles, which were washed two times and solubilized in 6.5 M formic acid, showing the UV absorption at 214 nm (blue graph, top) and the total ion current (TIC, black graph, top). An 8,240 Da mass was detected early on (around 2.1 min, as indicated by the highlighting circle) by both UV absorption and TIC measurements, right after the initial formic acid solvent front (between 1 – 2 min). Mass spectra of the unmarked TIC peaks at 5.8, 6.5, 9.5, 9.9, 10.3 and 14.2 min did not contain any masses unambiguously correlated to known Gvp proteins and are thus not presented here.*

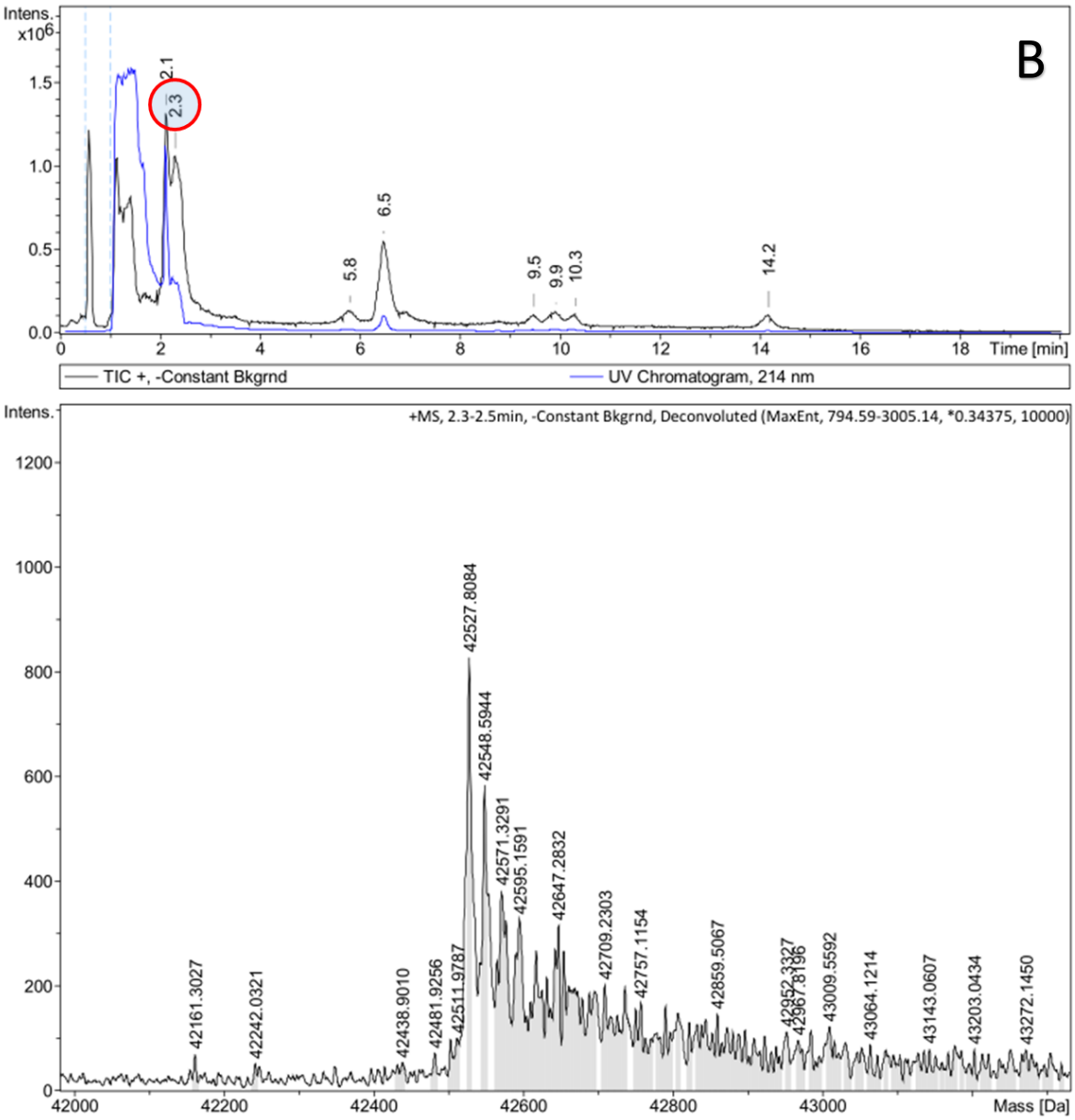

Figure 36 B. *LC-MS analysis of gas vesicles, which were washed two times and solubilized in 6.5 M formic acid. A second protein peak, significantly less prominent In the UV absorption, eluted at 2.3 min (highlighting circle), right after the primary peak. Mass spectrometry revealed a 42.5 kDa mass. Its wide range of mass distributions suggests a variety of protein modifications and prevents precise identification.*

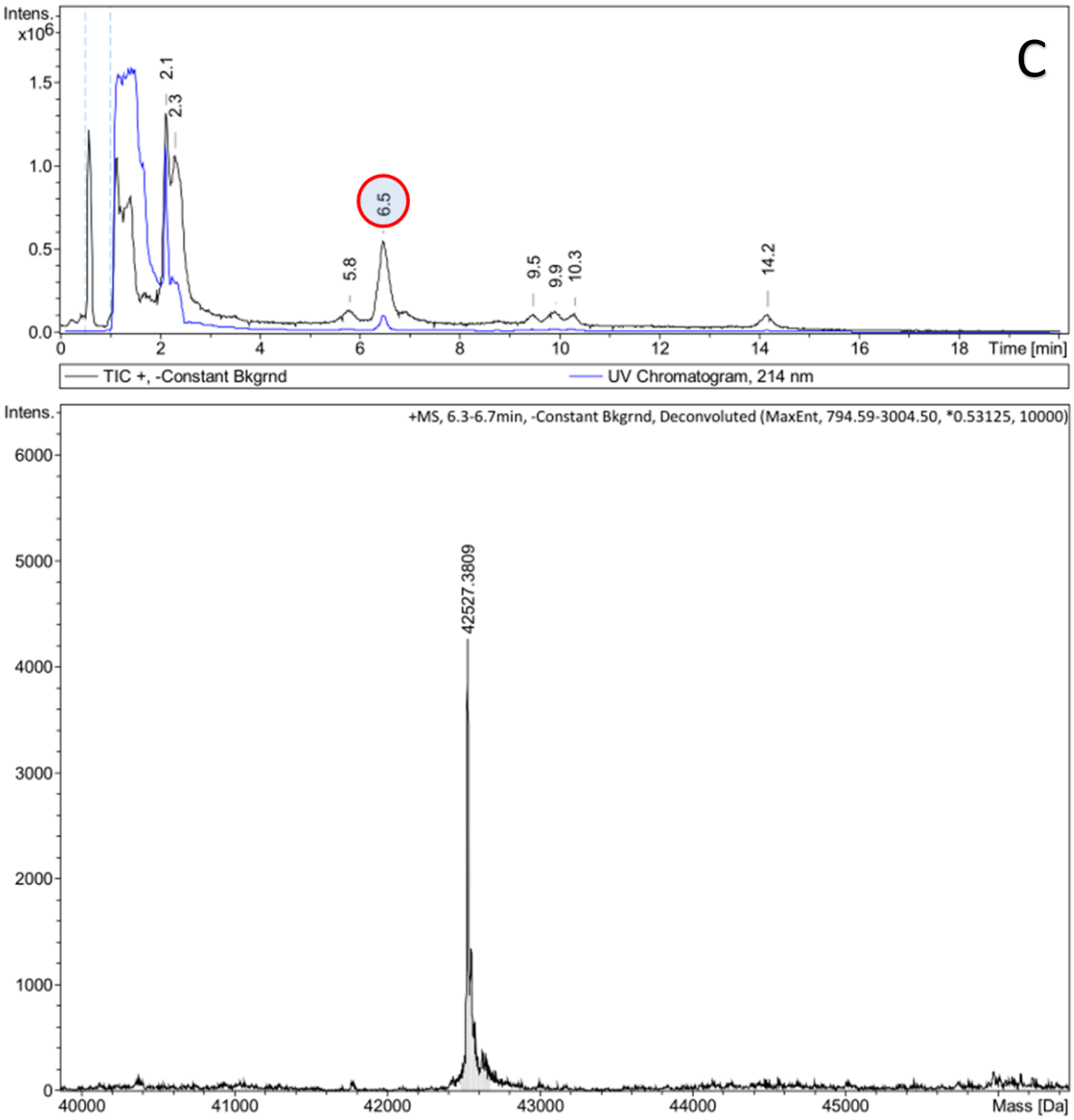

Figure 36 C. *LC-MS analysis of gas vesicles, which were washed two times and solubilized in 6.5 M formic acid. Similar to the previous peak at 2.3 min, a mass detected of 42.5 kDa was detected but without any notable mass deviations.*

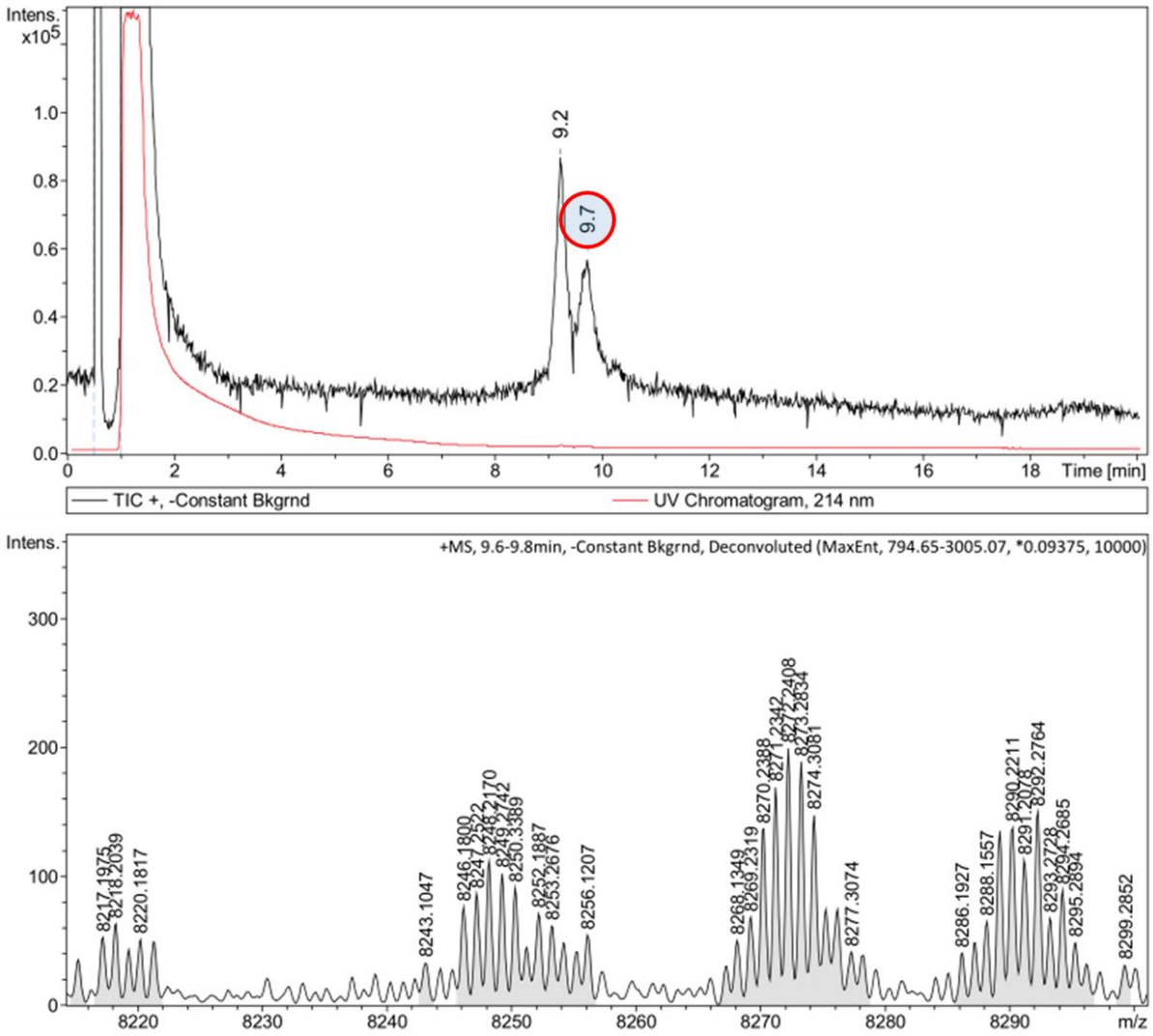

Figure 37. *LC-MS analysis of gas vesicles, which were washed four times and solubilized in 6.5 M formic acid. After a very strong initial solvent front peak, two main TIC peaks occurred at 9.2 and 9.7 min, respectively. Both had a very low UV absorption and the 9.2 min peak did not contain any identifiable mass ratios. The 9.7 min peak (highlighting circle) contained masses of 8.25 kDa, 8.27 kDa, and 8.29 kDa with discernible isotope distributions. Mass spectral lines within the unmarked TIC peak at 9.2 min are omitted here, as they did not contain protein masses that could be linked to Gvp proteins.*

4.3.2. Optimization of parameters for gas vesicle vitrification

The vitrified gas vesicles should be encased by a thin layer of ice, but without inducing compression. For this purpose, several vitrification parameters were tested using the *Vitrobot* Mark IV for the point mutant vesicles and the *Vitrobot* Mark III for the wild type vesicles, depending on availability (see 3.8.2 and 3.8.3). Detailed vitrification protocols are described in chapters 3.8.2 and 3.8.3. Blotting offset and blotting strength respectively, as well as blotting time were changed between different sets of samples. At least two grids per set were produced and screened in a 300 kV *Tecnai Polara* TEM.

Tables *3* and *4* summarize the results of systematically adjusted vitrification conditions. A low blotting offset for the *Vitrobot* Mark III generally lead to a thin, homogenous vitreous ice layer. Surprisingly, positive offset values were very harsh and partially blotted the gas vesicles off the grid surface. This effect was greatly amplified in combination with a longer blotting duration. A shorter blotting time of around 3 s with a blotting offset of -3 mm was found to produce satisfactory results. The *Vitrobot* Mark IV yielded relatively thick vitreous ice sheets at lower blotting strength settings. A blotting strength value of “5” with a slightly increased blotting time of 4 s produced good sample conditions. In contrast to the full cell vitrification of halobacteria, vitreous gas vesicle samples could be obtained with highly reproducible particle distributions and homogenous ice thickness. These conditions were therefore used throughout all following investigations for the structural determination of vitrified gas vesicles.

Table 3. Vitrification of halobacterial wild type gas vesicles using a Vitrobot Mark III and different blotting parameters. The parameters with the most suitable results are marked in green.

	sample 1 **2 grids**	**sample 2** **4 grids**	**sample 3** **4 grids**	**sample 4** **4 grids**
***Vitrobot* chamber temperature**	RT	RT	RT	RT
***Vitrobot* chamber humidity**	70 %	70 %	70 %	70 %
blotting offset	-5 mm	-3 mm	no offset	+3 mm
blotting duration	4 s	4 s	4 s	4 s
observations	very thin ice, very few vesicles	thin ice, good distribution of vesicles	very thin ice, very few gas vesicles	no gas vesicles on the grid

	sample 5 **12 grids**	**sample 6** **2 grids**	**sample 7** **4 grids**	**sample 8** **2 grids**
***Vitrobot* chamber temperature**	RT	RT	RT	RT
***Vitrobot* chamber humidity**	70 %	70 %	70 %	70 %
blotting offset	-3 mm	-3 mm	no offset	no offset
blotting duration	3 s	5 s	3 s	5 s
observations	thin homogenous ice layer, many vesicles	thin, sparse ice layer, many vesicles	thin homogenous ice layer, many vesicles on carbon	very thin ice, most vesicles on carbon

Table 4. Vitrification of halobacterial I34M point mutant gas vesicles using a Vitrobot Mark IV and different blotting parameters. The parameters with the most suitable results are marked in green.

	sample 1 **4 grids**	**sample 2** **4 grids**	**sample 3** **4 grids**	**sample 4** **4 grids**
***Vitrobot* chamber temperature**	RT	RT	RT	RT
***Vitrobot* chamber humidity**	70 %	70 %	70 %	70 %
blotting strength	"3"	"5"	"10"	"15"
blotting duration	3 s	3 s	3 s	3 s
observations	thick homogenous ice, many vesicles	thick homogenous ice, many vesicles	thin ice, partially compressed vesicles	thin ice, very few vesicles

	sample 5 **4 grids**	**sample 6** **4 grids**	**sample 7** **4 grids**	**sample 8** **4 grids**
***Vitrobot* chamber temperature**	RT	RT	RT	RT
***Vitrobot* chamber humidity**	70 %	70 %	70 %	70 %
blotting strength	"5"	"5"	"5"	"5"
blotting duration	2 s	4 s	5 s	6 s
observations	thick homogenous ice layer, many vesicles	homogenous ice layer, many vesicles	homogenous ice layer, reduced vesicle numbers	thin ice layer, reduced vesicle numbers

4.3.3. Electron dose tolerance of gas vesicles

Gas vesicles have been previously reported to be particularly sensitive to electron radiation by Offner *et al.* [68]. This could be corroborated in early tomography studies of isolated gas vesicles in the context of this work. In these recording series, the regular 4.6 nm rib structure of the vesicle seemed to have almost entirely dissolved after a total exposure to around 100 e/Å², a dose typical for cryo-electron tomography [69]. To better quantify the extent of the induced damage at different exposure levels of the specimen to the electron beam, dose series of 14 e/A² per exposure were recorded (see 3.9). Additionally, the power spectrum of each micrograph was examined to evaluate the diffraction pattern, specifically the layer lines caused by the regular helical repeats of 4.6 nm. The results are shown in *Figure 38*. Here, the attenuation of the third-order diffraction pattern of these layer at electron doses as low as 40 e/Å² indicated the beginning of considerable structural damage. While preservation of the third order diffraction intensities limited information to a resolution of $\frac{4.6\ \mathrm{nm}}{3} \approx 1.5$ nm, the averaging of subtomograms in combination with a structural classification method would be able to resolve the additional structural heterogeneity. At a dose over 50 e/Å² the vesicle rib structure was visibly destroyed, exhibiting a bloated, significantly smoothened surface structure. Therefore, the total electron dose for recording was kept below 40 e/Å², with an average dose of 30 – 35 e/Å² per tilt series. Based on these observations, this was deemed an appropriate compromise between a sufficiently high SNR per tilt for high resolution imaging and the incurrence of structural damage on a moderate or greater scale.

total dose	**detail of vesicle ribs**	**Fourier-transform (*log* of FFT²)**
14 e/Å²	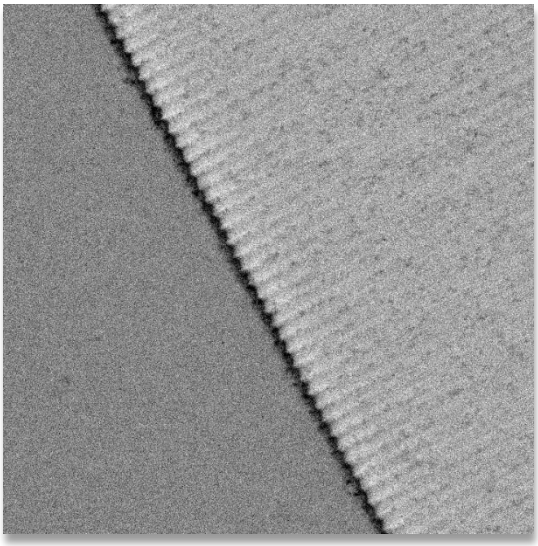	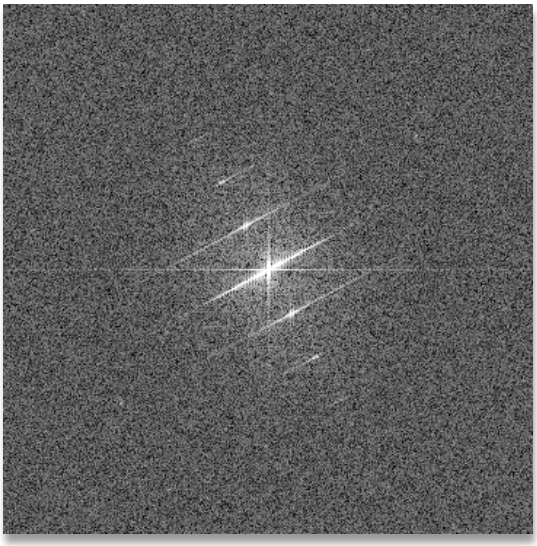
28 e/Å²	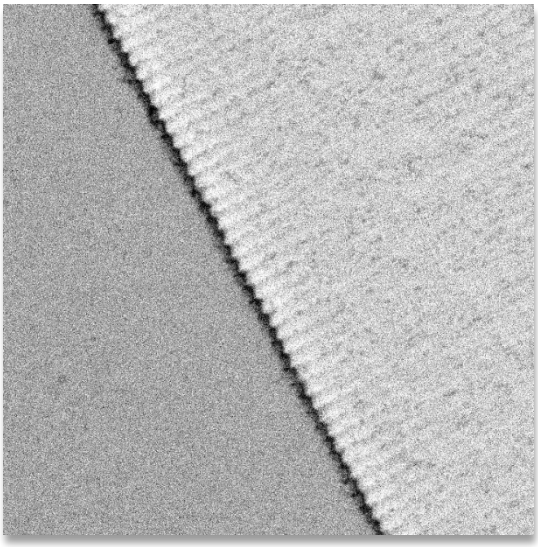	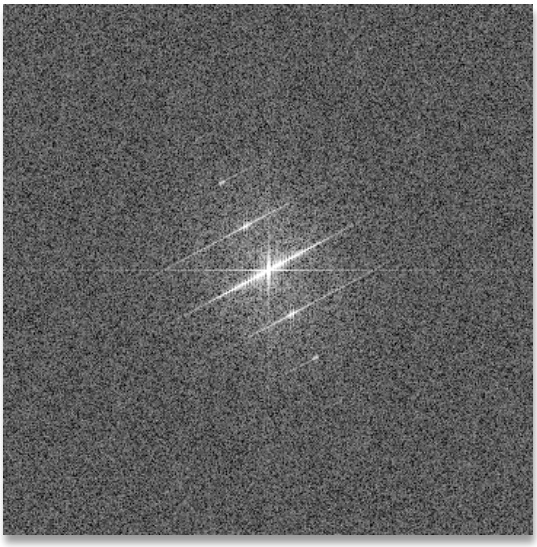
42 e/Å²	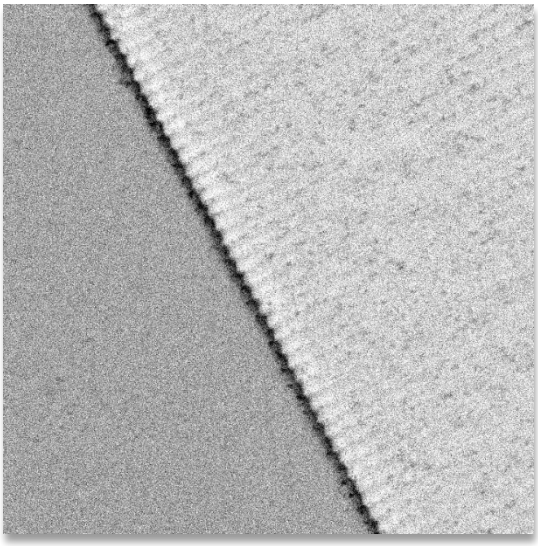	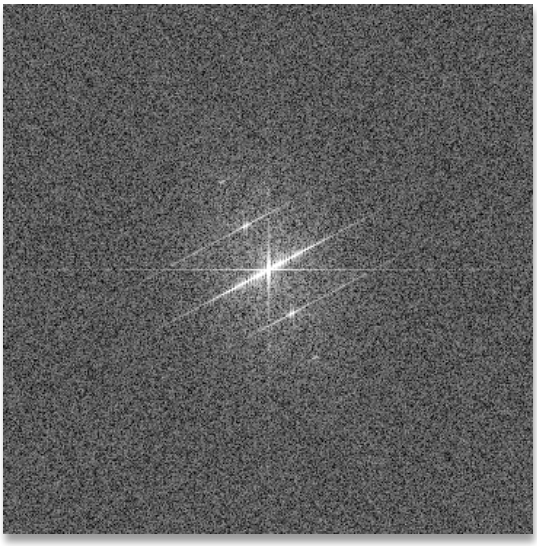

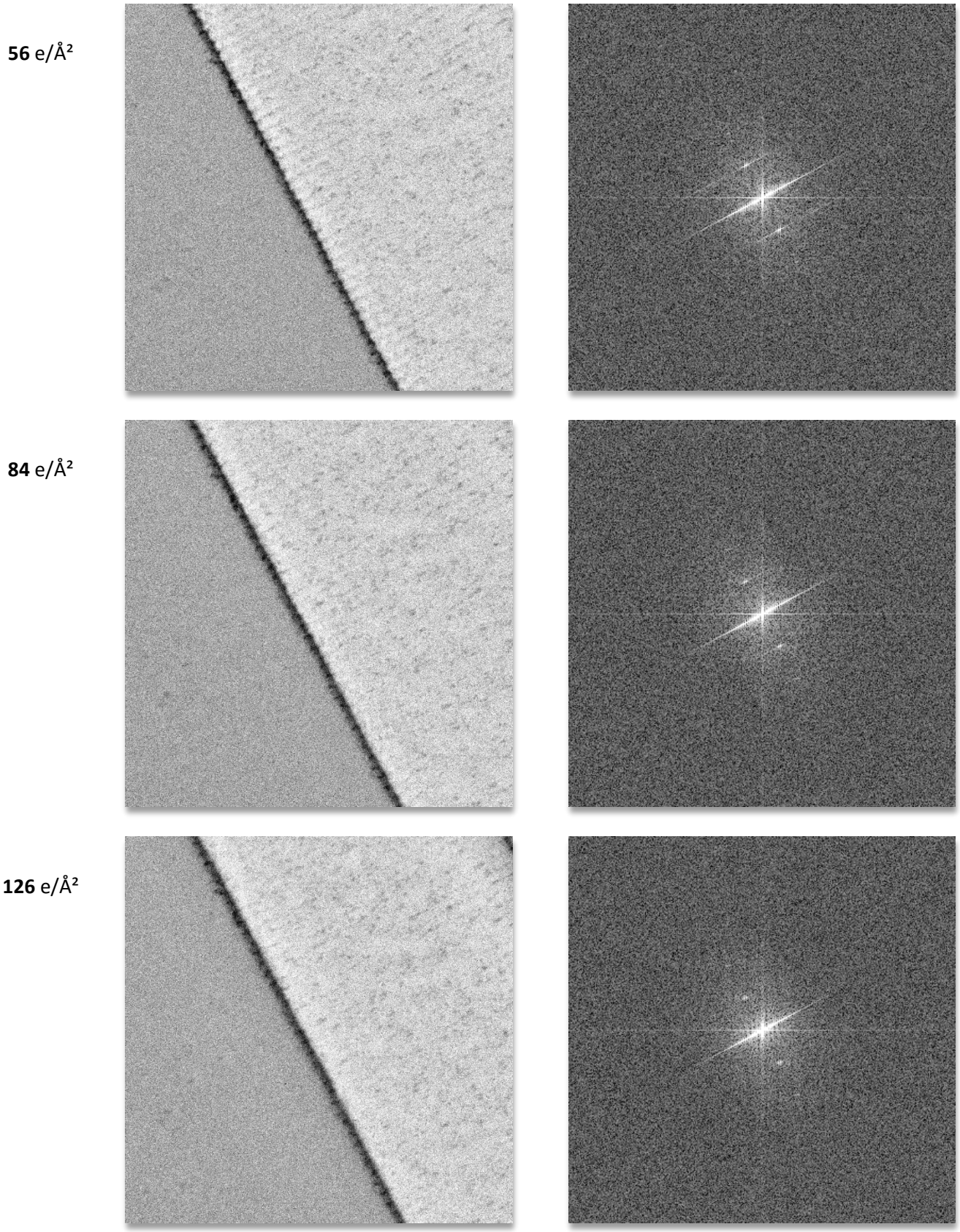

Figure 38. *Radiation sensitivity of vitrified isolated gas vesicles from H. salinarum wild type. A dose series of consecutive 5 s exposures, at a dose rate of 2.8 e/(Å²·s), was used to assess electron-induced structural*

damage to the specimen. Damage is most noticeable by structural decomposition of the regular helical ribs, which are visibly disintegrating at doses ≥ 50 e/Å². The respective power spectra illustrate the extent of the deformation through the loss of information within the layer lines of the 4.6 nm-pitched helix. At 56 e/Å² the third-order diffractions have almost entirely vanished.

4.3.4. Cryo-electron tomography of isolated gas vesicles

Gas vesicles were tomographically recorded in a 300 kV *Titan Krios* (see 3.9) for subsequent 3D reconstruction. Suitable targets for tomography and subtomogram analysis were manually chosen by strict criteria. As a minimum prerequisite, the vesicles had to be visually structurally intact. The average diameter measured around 100 nm for the point mutant, and 120 nm for the larger wild type vesicles, with an allowed tolerance of ± 25 nm. Both factors provided structural consistency and offered the greatest possible area for subtomogram analysis per vesicle. In addition, the longitudinal vesicle axis had to be collimated to the tilt axis of the sample stage within ±10 ° in order to prevent parts of the structure to rotate significantly out of the preset defocus at higher tilt angles. The overview micrograph in *Figure 39* shows an example of a potential tomogram target fulfilling the selection criteria. *Figure 40* elucidates the morphological differences of the I34M point mutant gas vesicles and the wild type gas vesicles.

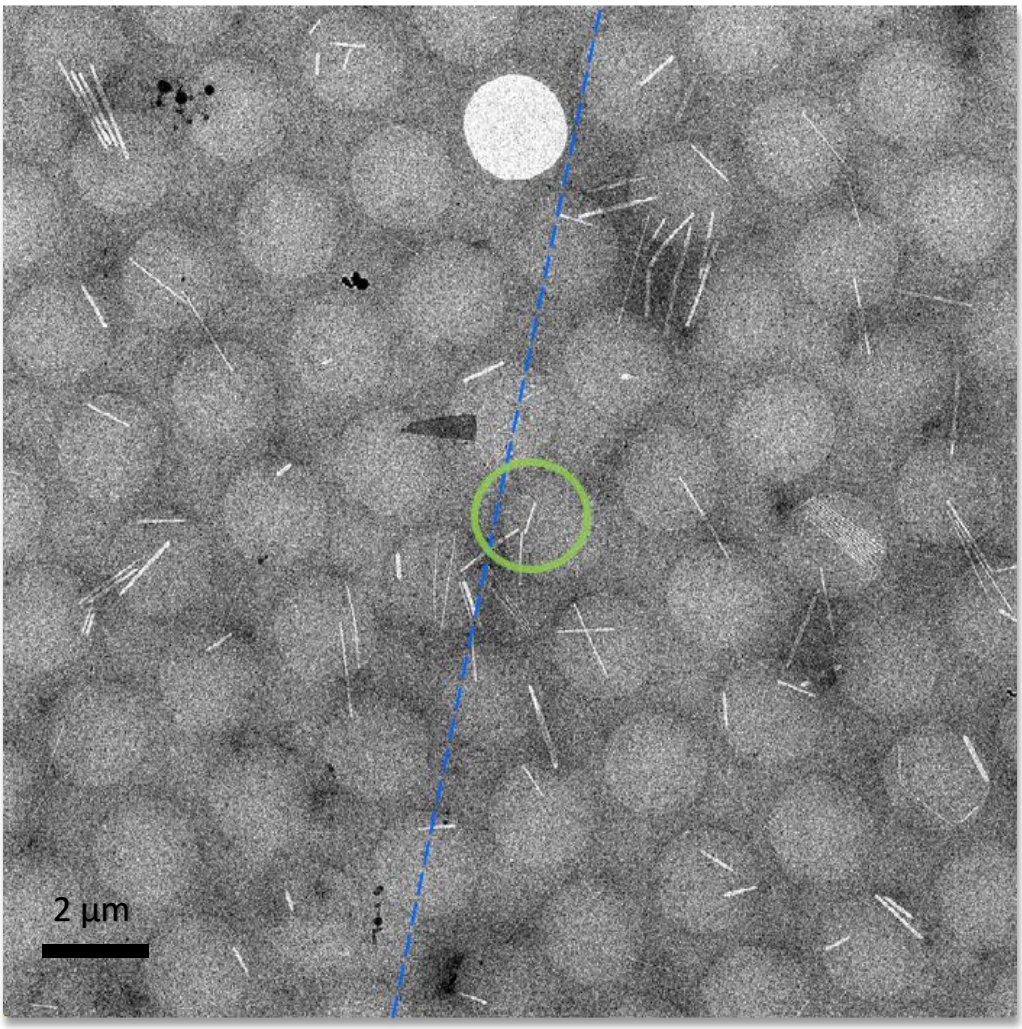

Figure 39. *Example of vitrified, isolated I34M point-mutant vesicles of H. salinarum. The marked region shows a suitable target for tomographic recording. The undamaged, thin vesicle is situated in a hole, covered in thin ice and aligned nearly parallel to the tilt axis (blue broken line).*

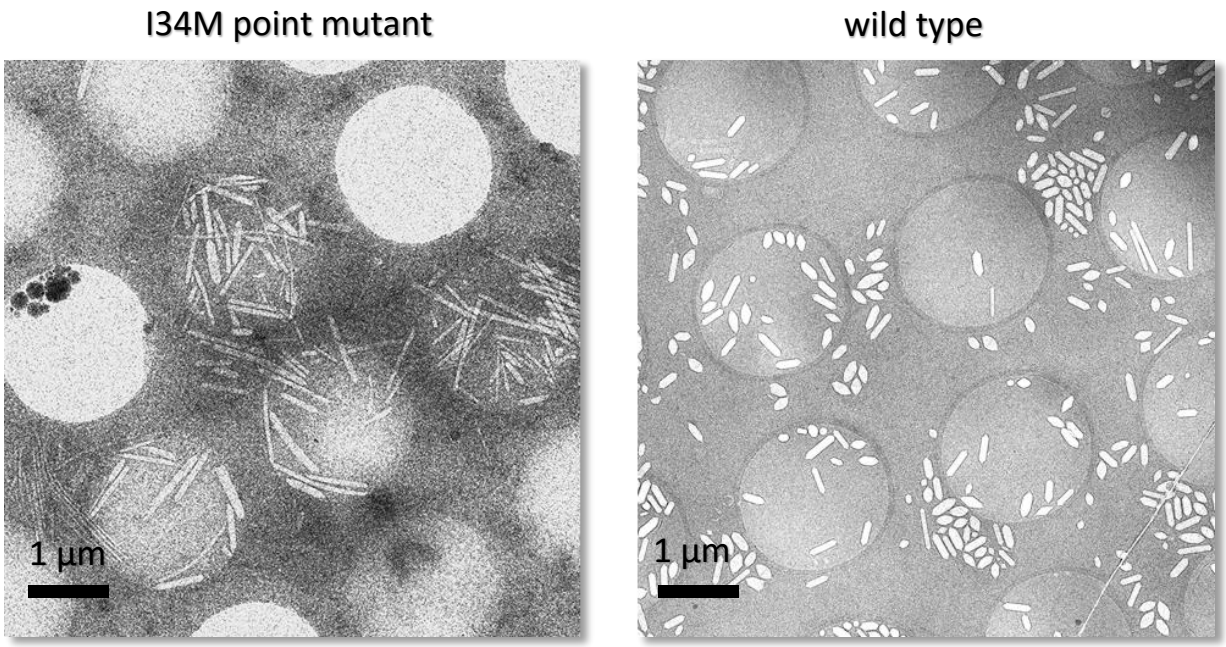

Figure 40. *Overview micrographs of gas vesicles from the I34M point mutant (left) and the wild type (right). The point mutant exclusively contains thin, cylindrical vesicles, whereas the wild type features both, cylindrical and spindle-shaped phenotypes. For purposes of 3D reconstruction, only thin and elongated vesicles were selected.*

Due to the high electron dose sensitivity of the gas vesicles (see 4.3.3), each tomogram was recorded with a total dose of only around 30 – 35 e/Å². As a general guideline, the helical ribs of the gas vesicle, as shown in the long exposure in *Figure 41*, should still be discernible in the individual tilt images.

A total of 49 tomograms suitable for subtomogram analysis (see 4.3.6) were selected. 28 of these originated from wild-type and 21 from I34M point mutant vesicles. It was found that wild type vesicles were overall thicker in diameter and seemed to compress more easily.

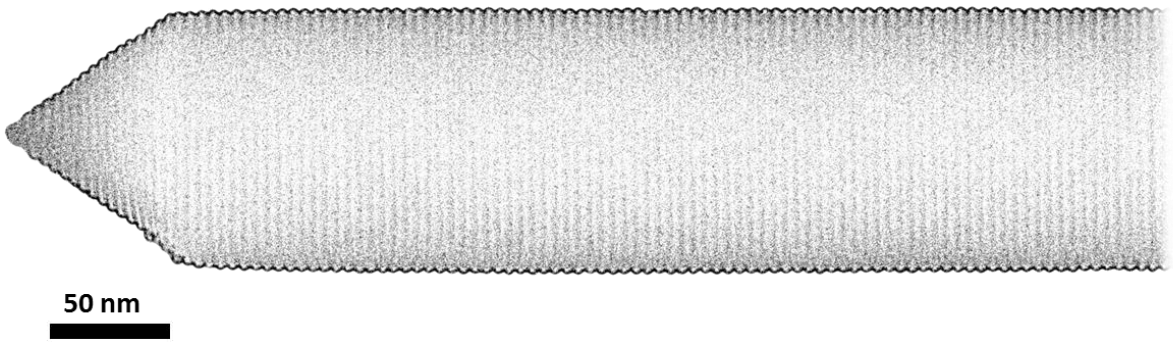

Figure 41. *Subframe-aligned long exposure micrograph (total dose 24 e/Å², 64,000× primary magnification) of a typical cylinder-shaped I34M point mutant gas vesicle. The distinct ribs form a wide helix with a pitch of 4.6 nm.*

4.3.5. Tomographic reconstruction and analysis of the gas vesicle helicity

In order to evaluate the expected helicity of the gas vesicle and determine the regions of regular arrangement of the gas vesicle protein GvpA, each tomogram was correspondingly analyzed. Power spectra show the characteristic first order layer lines originating from the regular repeats of the 4.6 nm rib structure. The central diffraction spots of the layer lines were masked in Fourier space. The frequency information contained within the masks was then Fourier back-transformed into real space. The Fourier-filtered volume exclusively consisted of the ordered helical parts of the gas vesicle with a strict pitch of around 4.6 nm, as illustrated in *Figure 42*. This information was used to select the most regular and thus suitable regions for further processing and subtomogram averaging.

Usually, the gas vesicle tips, as well as a central seam region within the cylinder did not exhibit the well-ordered rib periodicity and were thus excluded from the subtomogram analysis. In these regions, the helical pitch was less consistent and slightly differed from the highly-ordered cylindrical vesicle body sections, as a power spectra comparison of isolated regions revealed (see *Figure 43*).

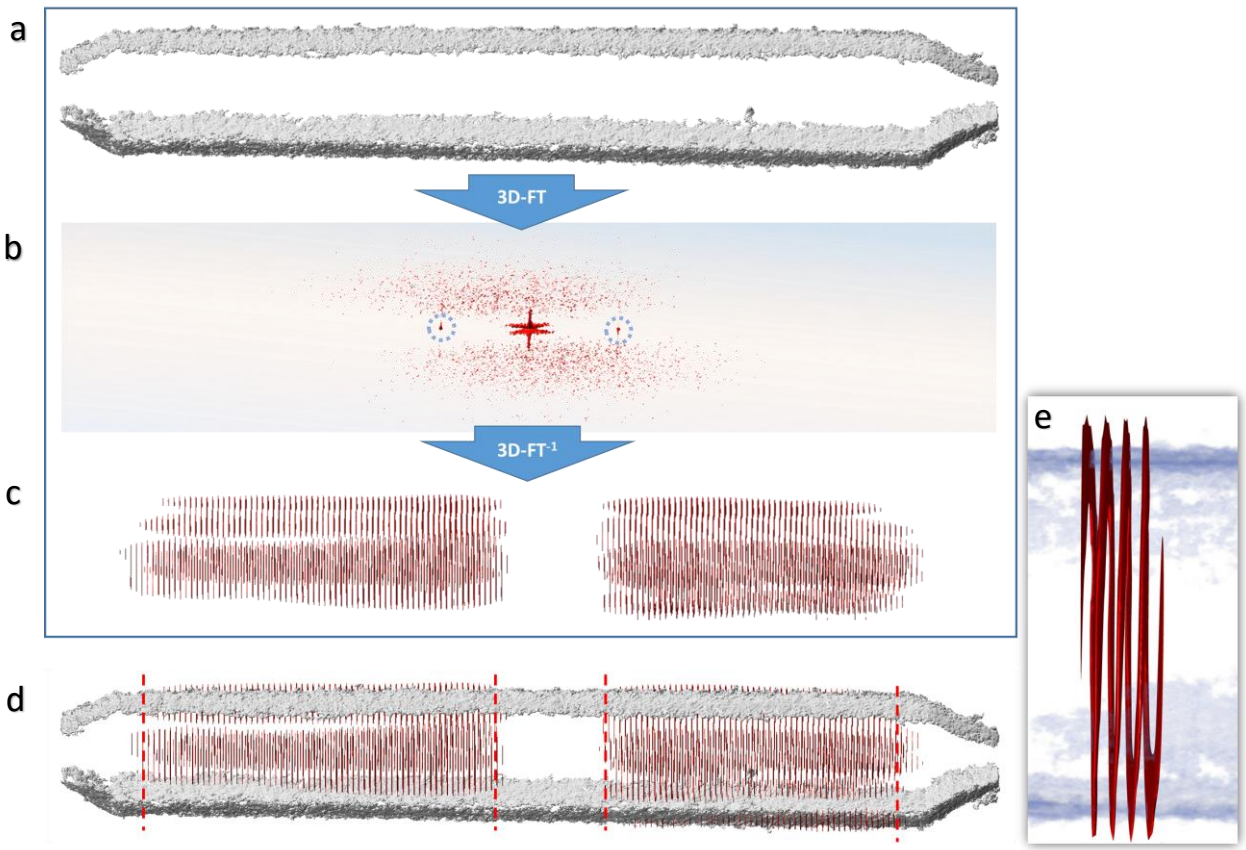

Figure 42. *Visualization of the gas vesicle helicity through Fourier-filtering. A tomographic reconstruction of a gas vesicle (a) was Fourier-transformed. In the power spectrum (b), the repeating 4.6 nm rib produces clearly visible layer lines with a prominent central spot (marked by blue circles). These reflexes were masked and back-transformed to real space coordinates, revealing the regions of strongly regular helical structure within the vesicle (c and d). The enlarged section (e) illustrates the helical arrangements more clearly. Both segments share an identical handedness.*

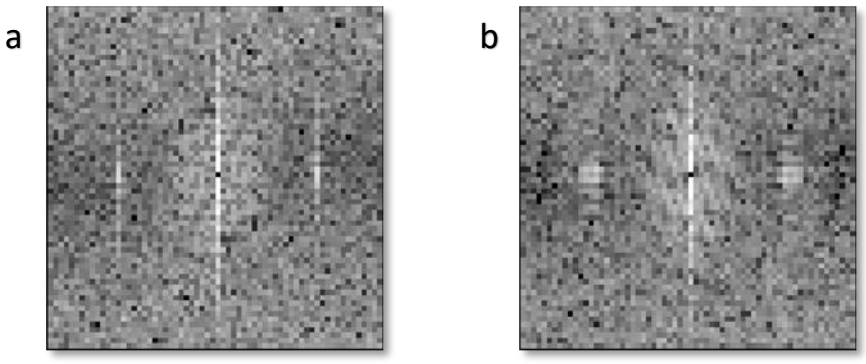

Figure 43. *Power spectra of cubic sections taken from the regular cylindrical vesicle body (a) and from the central seam region (b). The first order diffraction layer lines of the rib structure became considerably less defined in the seam region, suggesting a structurally more diverse pattern.*

4.3.6. Subtomogram analysis of the gas vesicle structure

The subtomogram analysis routine as described in 3.12 had to be modified to address the particular difficulties associated with the very low SNR of individual subunits within the gas vesicle tomograms (see 3.9 and *Figure 44* for comparison). While the 4.6 nm ribs form a visible characteristic pattern, single 8 kDa GvpA subunits within the helical turns are too small to reliably show as distinct features. This prevents the precise localization of single monomers via cross-correlation within the ribs. In addition, the complete absence of available structural references from other sources made it necessary to generate a template *in-situ*. A strategy was pursued to extract a larger initial reference template from a vesicle tomogram for the localization of rib-structure motif repeats in combination with the exploitation of the regular cylindrical geometry of the envelope. The cubic template comprised three helical repeats. High-resolution information, such as the positioning on GvpA, would only become accessible after alignment and a branched classification of the combined particle stack from numerous tomograms. This refinement method was also able to perform in the absence of an *a priori* structural reference and with the extremely low SNR of the small individual subunits.

Before initiation of the subtomogram analysis subroutines, all suitable gas vesicle tomograms were prepared by centering the vesicle motif and rotating its principal axis to run parallel to the Y-axis of the image coordinate system. Next, the centered and axis-aligned vesicles were split into two separate volumes, each containing one of the two regular helical cylinder halves which were previously determined in 4.3.5.

The following subtomogram analysis was performed independently for the two cylinder halves from each tomogram. The program cycle, consisting of constrained template matching, subvolume extraction, initial averaging and fine alignment, was iteratively repeated three times. Finally, a two-step branched multi-reference classification was performed to improve resolution of the subunits.

Both types of gas vesicles, wild type and I34M point mutants, were separately analyzed. In total, 56 vesicle cylinder halves were processed for the wild type and 42 halves for the I34M point mutant.

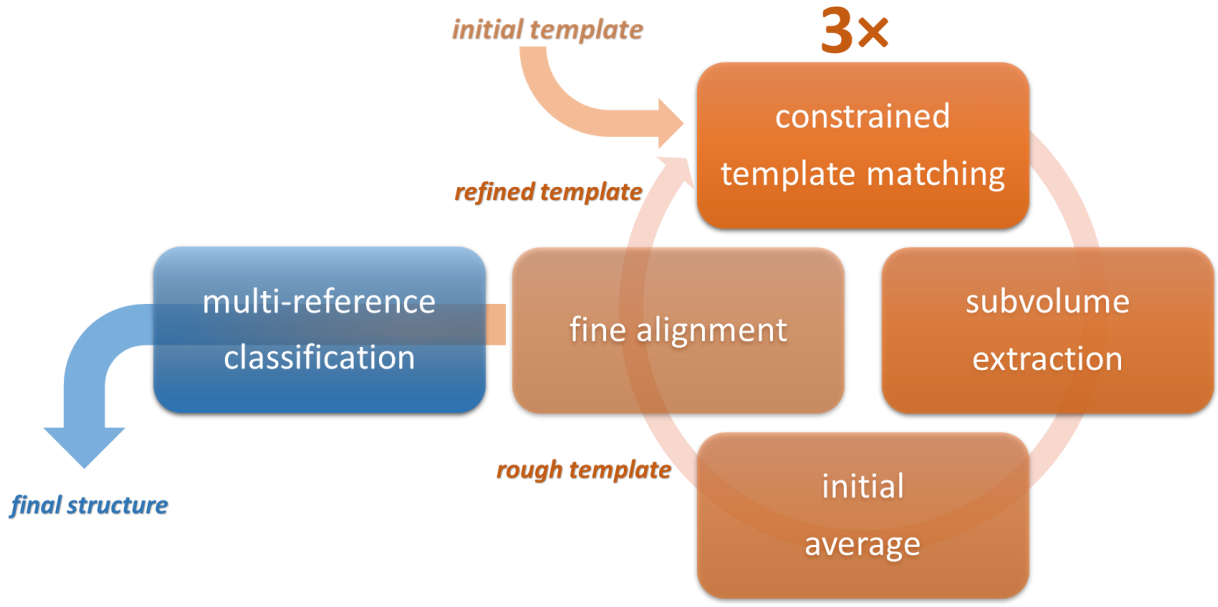

Figure 44. *Adapted subtomogram analysis program flow for the gas vesicles. Clock-wise, from the top: Template matching, constrained to individual vesicle body segments to exploit the cylinder geometry, generated a CCF map. The global maximum of the CCF map was determined and a subvolume extracted at its position. The peak was then eliminated with a spacer mask. After elimination, the process was repeated for the next highest maximum until all particles were extracted. Initial averaging of the particles, which carried approximated angular information from the template matching step, did not resolve molecular details, but provided an intermediate template with higher SNR for subsequent angular and shift refinement. This fine alignment resulted in further improved templates for the next iteration of the program cycle. After three iterations, it supplied the final aligned particle stack for the multi-reference classification.*

4.3.6.1. Constrained template matching

As previously mentioned, an individual subunit would have an insufficient SNR for direct localization. Instead, a much larger template of 14.4 × 14.4 × 14.4 nm (64^3 voxels) was used, that contained multiple subunits and spanned over three helical ribs of the gas vesicle. Furthermore, the geometry of the truncated regular vesicle parts allowed the estimation of the rotational alignment for any particle located along the cylinder envelope. The template matching process made use of this fact by radially separating the cylinder into multiple sections along the principle axis. Each template was rotated to lie approximately tangential to its respective cylinder arc segment. Cross-correlation was then performed in each separate cylinder sub-section with the accordingly pre-rotated search template.

Since no pre-existing structure was available, an initial template was extracted directly from the tomographic volume for the first iteration of the template matching. A cubic template comprising three helical repeats with around ten GvpA monomers each was centered on a rib within a one time-binned vesicle tomogram.

In order to reduce computation time and reduce the occurrence of potential mismatches, cylinder volumes were generated in 3° steps along the vesicle's circumference, separating the envelope into 120 overlapping segments, as demonstrated in *Figure 45*. For each segment, the template was sequentially rotated in 3° steps around the Y-axis. Each template was convolved with the missing wedge pattern [62, 70]. The wedged templates were then cross-correlated with their corresponding cylindrical section of the gas vesicle envelope. Correlation coefficients of all segments were combined to create the global CCF map (see 3.12). This map therefore also contained the rough rotational orientation of the template for each segment along the circumference of the cylinder. Overlapping cylinder regions were merged by prioritizing voxels with the higher cross-correlation score for each position.

After refining angles and shifts for the alignment of the extracted particles (see 4.3.6.4) the template matching process was iteratively repeated with the improved templates, until the precision of the template localization along the cylindrical envelope could not be further improved.

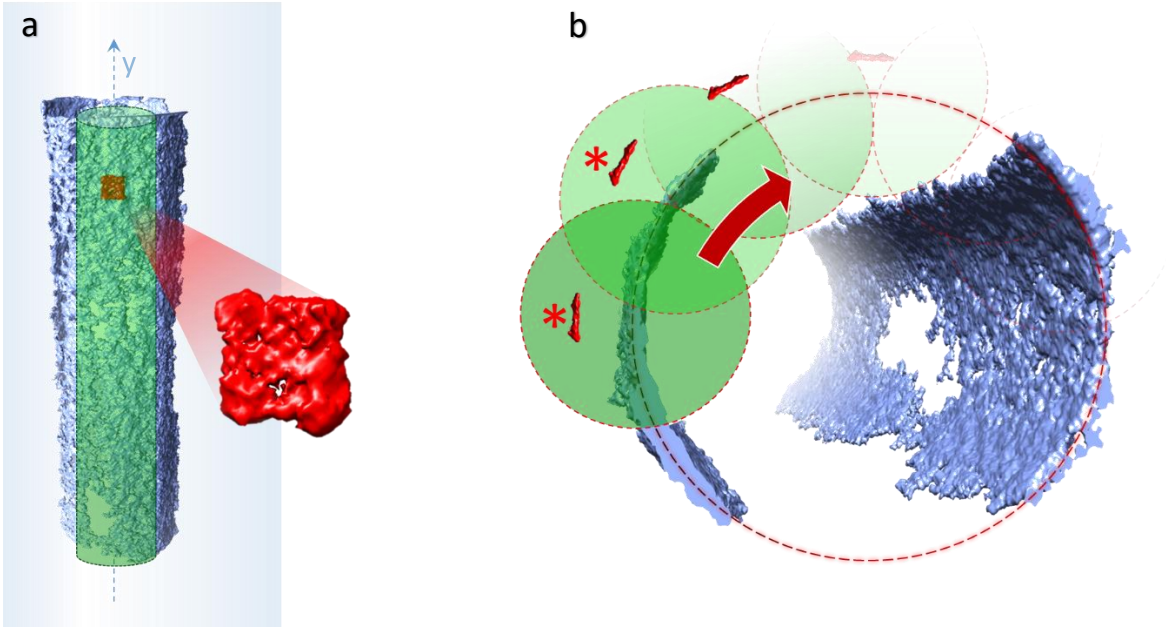

Figure 45. *Schematic representation of the constrained template matching algorithm. For the first iteration, an initial template is extracted (a). The gas vesicle cylinder is separated into multiple sub-regions (b) so that the angular search can be constrained by pre-rotating the template to match the relative rotational orientation for each cylinder segment. The rotated template is then cross-correlated against its pertaining segment.*

4.3.6.2. Subvolume extraction

For the generation of subvolume stacks, the correlation coefficient maxima in the CCF map were determined and particles extracted at each peak position. Since any particles of interest had to lie within the vesicle wall, the topology of the vesicle was utilized to further constrain the cross correlation to the envelope volume and exclude false positive hits. *Figure 46* shows a typical correlation coefficient peak map, overlaid on top of its original tomogram volume.

First, the gas vesicle wall was segmented with *membseg2* [71]. The resulting mask was multiplied with the cross correlation map to eliminate peaks outside of the vesicle wall. Afterwards, the position of the global correlation coefficient maximum was determined, and the entire peak removed from the cross-correlation map. This was done by creating an elimination mask at the center of the peak. The mask size was equivalent to the width of the initial template (see 4.3.6.1) along one helical repeat of 4.6 nm. Within this mask, voxel values were set to -1, the minimal value of the normalized cross correlation function. After the elimination of the first peak, the next highest correlation coefficient maximum was treated in the same way. The process was repeated until all particle positions were determined or the correlation coefficient values fell below a predefined threshold. The peak extraction resulted in a list of coordinates indicating the positions of subvolumes along the gas vesicle envelope.

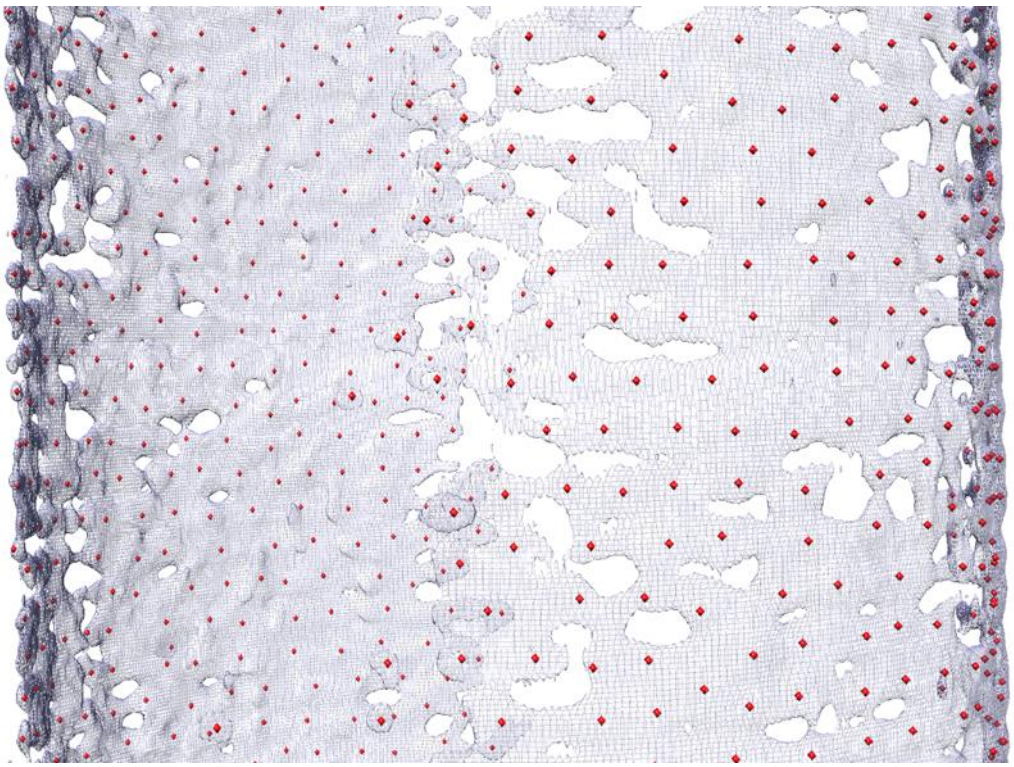

Figure 46. *Correlation coefficient map for peak extraction. Maxima used for the particle localization (red) are superimposed on the tomographic cylindrical vesicle segment (light blue).*

Subtomograms were extracted from the unbinned volume, as illustrated in *Figure 47*. To account for the previous binning factor applied for the template matching, the coordinates retrieved from the peak extraction were scaled up by a factor of two. From these positions along the vesicle envelope, cubic subvolumes of 64^3 voxels, spanning over three ribs with around 12 GvpA monomers each, were boxed out. Subvolume extraction for all cylindrical half segments resulted in a merged stack of around 250,000 subvolumes for the wild type and 280,000 particles for the I34M point mutant.

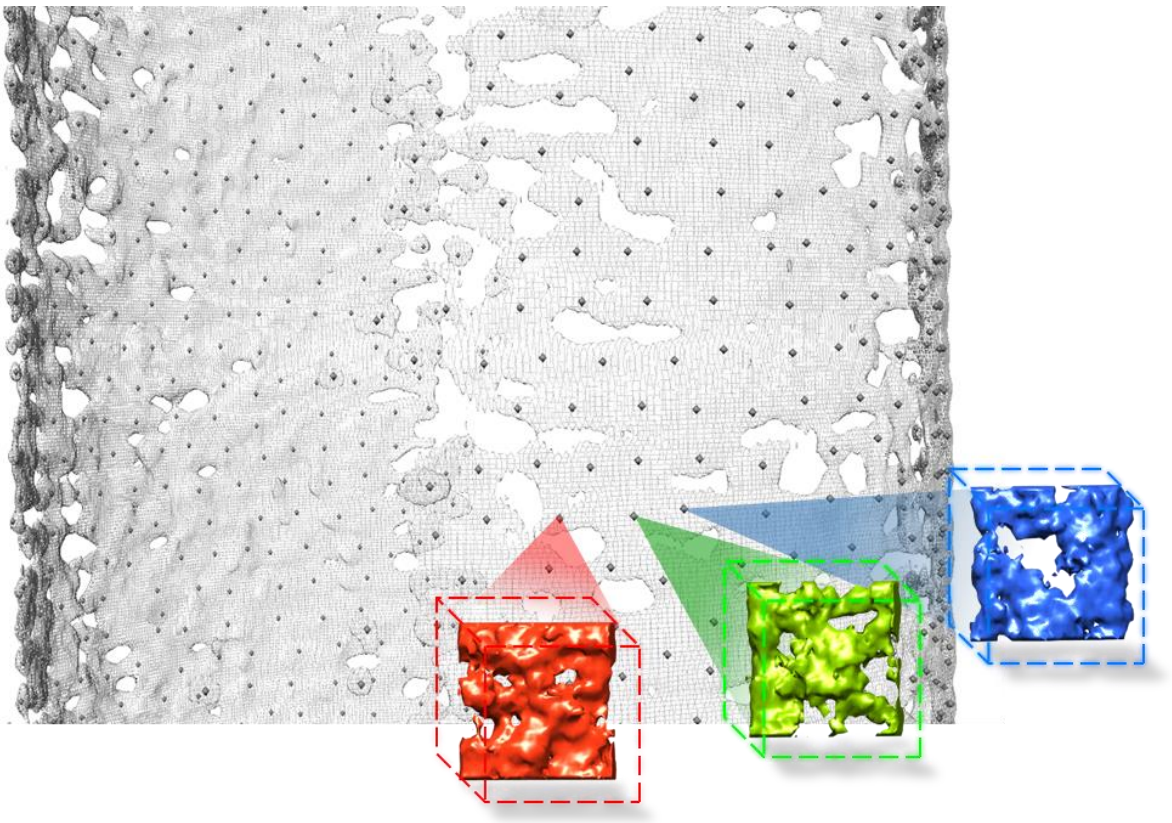

Figure 47. *Extraction of cubic subvolumes to create the final unaligned subvolume stack. The particles were cubic with an edge length of 64 voxels, corresponding to 14.4 nm. This was enough to comprise three helical repeats.*

4.3.6.3. Initial subvolume averaging

Using the rotational orientations provided by the template matching, an initial alignment of the subtomograms was performed. For this purpose, the structures within the stack were re-oriented to correspond to the 0° initial particle template and then averaged.

Aligned and averaged subtomograms of opposed cylindrical vesicle segments clearly showed a directional orientation of the rib-structures (see *Figure 48*). Distinct "hook"-like features at the outer surface were pointing into the direction of the central seam. These hooks were always facing towards the central seam section of the vesicle and were in accordance with the opposite orientation of the helical ribs of the two segmented vesicle halves. The helical handedness, however, remains constant in both regular cylinder sections.

In a few vesicles this seam clearly showed as a slight displacement of around 1 – 2 nm of the opposing envelope halves. In all vesicles analyzed by Fourier-filtering it could be detected as a central region of about 15 – 20 nm in which the highly ordered 4.6 nm helicity of the cylindrical regions was lost (see 4.3.5).

While showing insufficient molecular detail in themselves, the initial averages served as the templates for the multi-reference alignments in the next step.

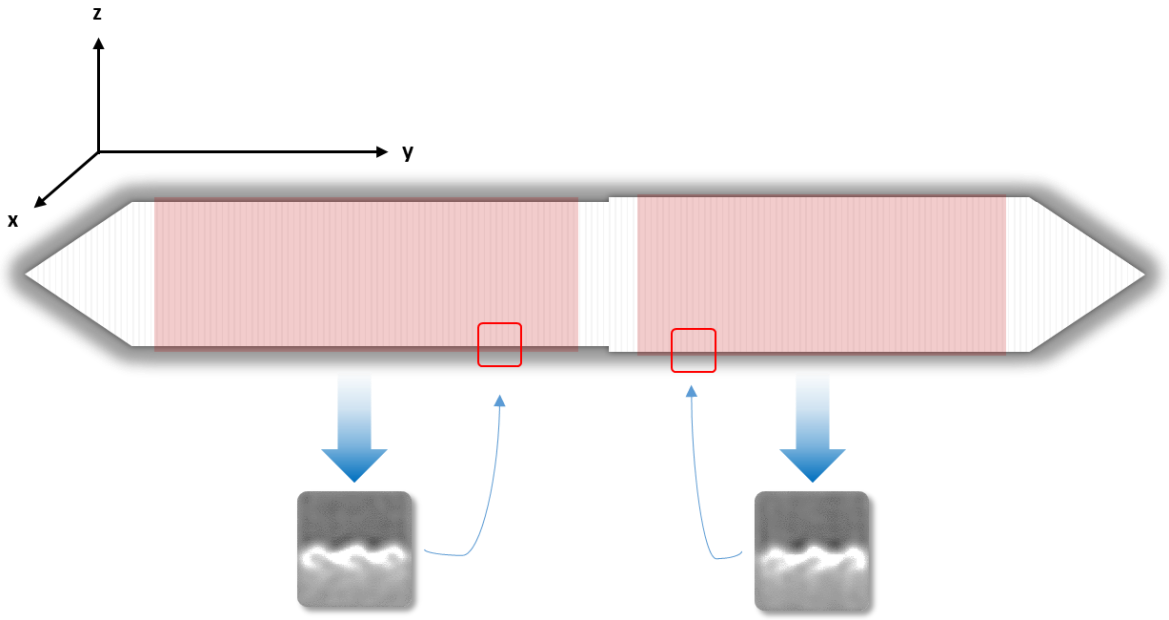

Figure 48. *Initial averaging of the extracted particles reveals hook-like structures on the hydrophilic outer surface of the vesicle. Each 4.6 nm rib seems to possess hook structures on the exterior surface of the envelope. The ribs from one half of the vesicle are rotated by 180° around the Z-axis, relative to those of the other half.*

4.3.6.4. Fine alignment and classification

In order to further improve the precision of subunit localization, shifts and angles were refined in an initial alignment. The average was then in turn used for the next iteration of the template matching. In total, three program cycles (template matching, subvolume extraction, subvolume averaging and fine alignment) were applied. Each cycle slightly improved the precision of the particle localization. After the third iteration, most of the correlation coefficient maxima used for particle extraction were localized along the center of the gas vesicle ribs with a regularly spaced distribution.

As a final refinement step, multi-reference classification was applied to analyze and separate structural differences of subtomograms within the stack. For this purpose, the subtomogram stack was randomly split in n parts. Subtomograms within each partial stack were averaged. This averaged structure served as a class template. Now each individual particle of the whole stack was aligned with the average of each class and assigned to the one with the highest cross-correlation score. This process was iteratively repeated until all particles were steadily assigned to one class. To prevent aligning the template to noise and the entrapment of the alignment optimization in local minima, an adaptive low pass filter was applied to the template. Lastly, constraining the multi-reference alignment to a smaller area weakened the effect of larger-scale structural variance, such as the potential flexibility of protein chains or local mechanical distortions of the vesicle envelope. Therefore, a cylindrical focus mask was used, covering only the center of a single rib within the subtomogram volume, which originally encompassed three ribs. All multi-reference alignment procedures were executed exclusively within this sub-region of the template volume.

For the initial classification step, two classes were generated. This first refinement resolved particle localization errors: For the GvpA point mutant, a smaller subgroup of particles (28 %) was centered on the concave part of the interior rib surface. The majority of particles (72 %) was centered on the convex regions, offset by half a helical pitch (2.3 nm) along the y-axis (see *Figure 49*). Both classes showed defined subunits comprising the ribs, with a smooth interior surface and a rugged outside, with strong hook-like features. In contrast, the wild type showed a particle distribution of 57 % for class 1 and 43 % for class 2, with the same feature separation.

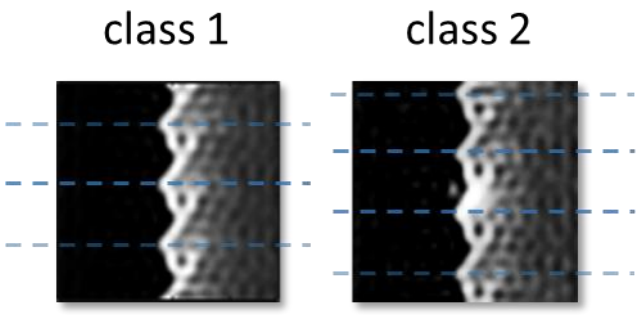

Figure 49. *Side view projections of the first multi-reference classification step averages of all point mutant subtomograms, revealing localization errors. Class 1 consists of particles centered on the region between two ribs, whereas class 2 particles were centered on a single helical rib. The dashed lines indicators are 4.6 nm apart and signify the position of one helical rib.*

Each of the predominant classes from both vesicle types of the first multi-reference alignment step were further refined. Here, a second multi-reference classification generated four classes (*see Figure 50 and Figure 51*) and helped to unravel fine-structural heterogeneity of the extracted subtomograms within the same focus region.

Multi-reference classification was able to significantly improve the resolution of subunits within the template volume. Assuming a protein density of around 1.4 g/cm³, mass-adjusted isosurface renderings of the refined classes revealed a smooth inward-facing surface of regularly spaced columns of 0.7 × 4.3 nm running almost perpendicular to the helical pitch [46]. These columns are spaced about 1.4 nm apart from each other, leaving a gap of about 0.7 nm in between, as shown in *Figure 52*. Two of the final refined classes also portrayed distinct densities on the outward-facing side, which seemed to diagonally connect two columns between two ribs. This is demonstrated in *Figure 53*. The aligned structure averages reached resolutions of around 10 Å for both vesicle types, as determined by gold-standard FSC (see *Figure 54*), in which each dataset was split into two independently refined halves [72]. While this value seems reasonable as the observed small column-like densities are clearly separated, it has to be noted that some regions seem to exhibit strong structural variability. This is particularly true for the outward-facing sides of the envelope and the wild type vesicles in general. The wild type envelope structure was more distorted, and multi-reference classification was unable to clearly resolve the high variance. For molecular docking models, we therefore focused on the more regularly structured I34M point mutant gas vesicles.

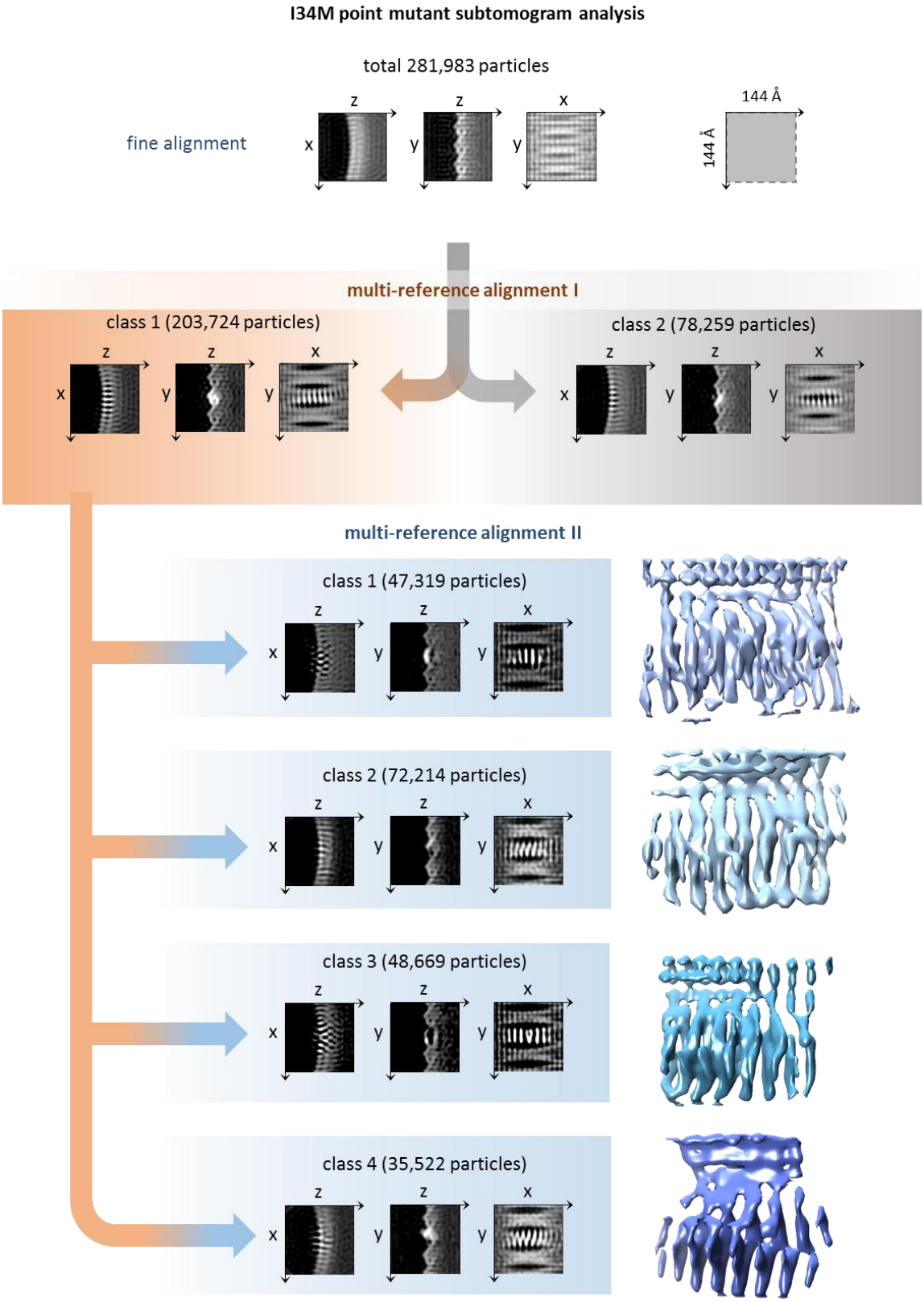

Figure 50. *Subtomogram analysis of the I34M point mutant gas vesicles. The entire stack of 281,983 particles is split in two classes via a multi-reference alignment. One class includes all offset particles from the template localization. The other is refined into four classes, further resolving structural details.*

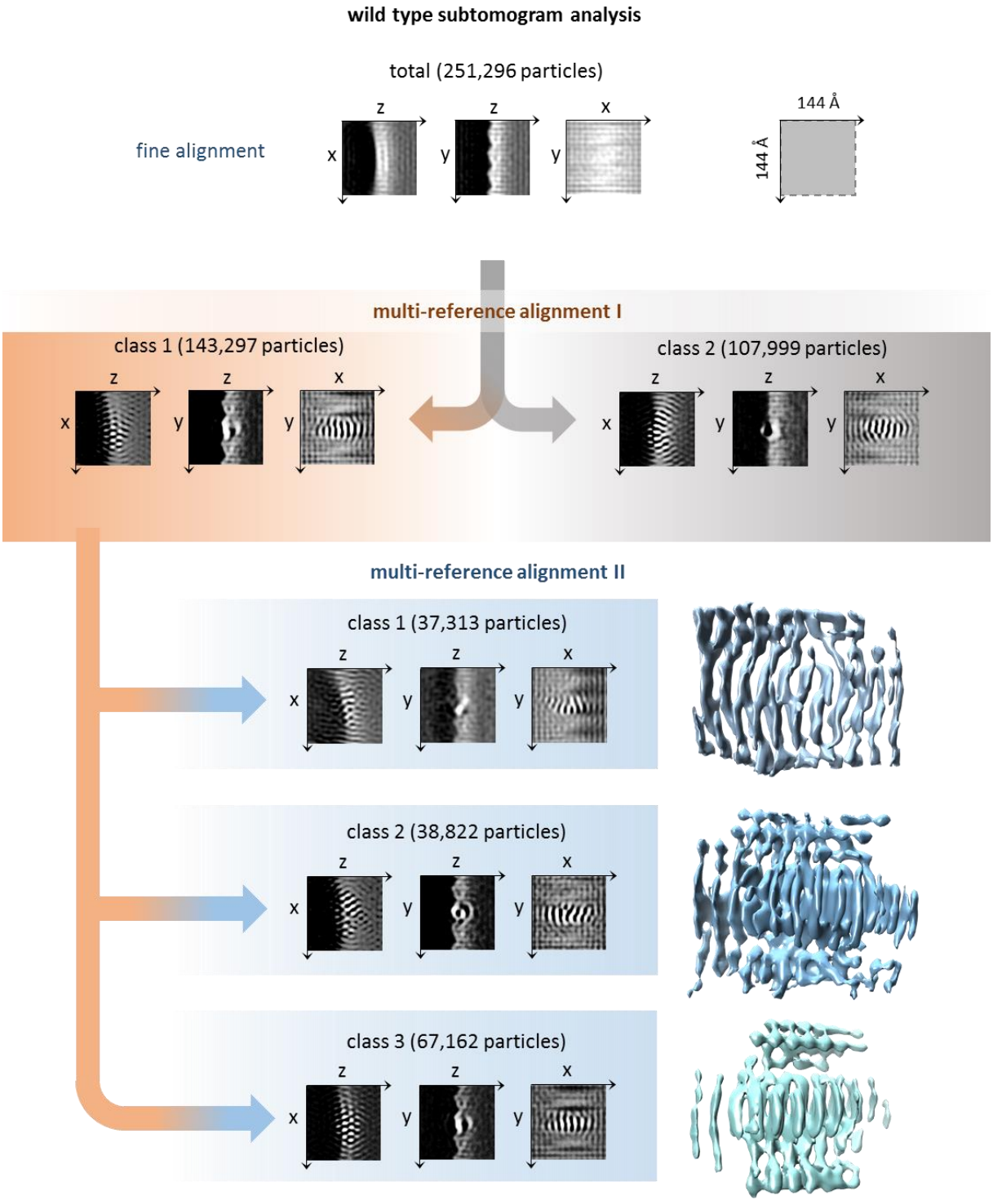

Figure 51. *Subtomogram averaging of the wild type gas vesicles. Here, too, the complete stack of 251,296 particles is separated by classification. Interestingly, the wild type vesicles seem to exhibit an increased structural variability, as indicated by the resulting aligned class averages; they show a much less regular arrangement and densities outside the focus region blur considerably compared to the aligned point mutant averages.*

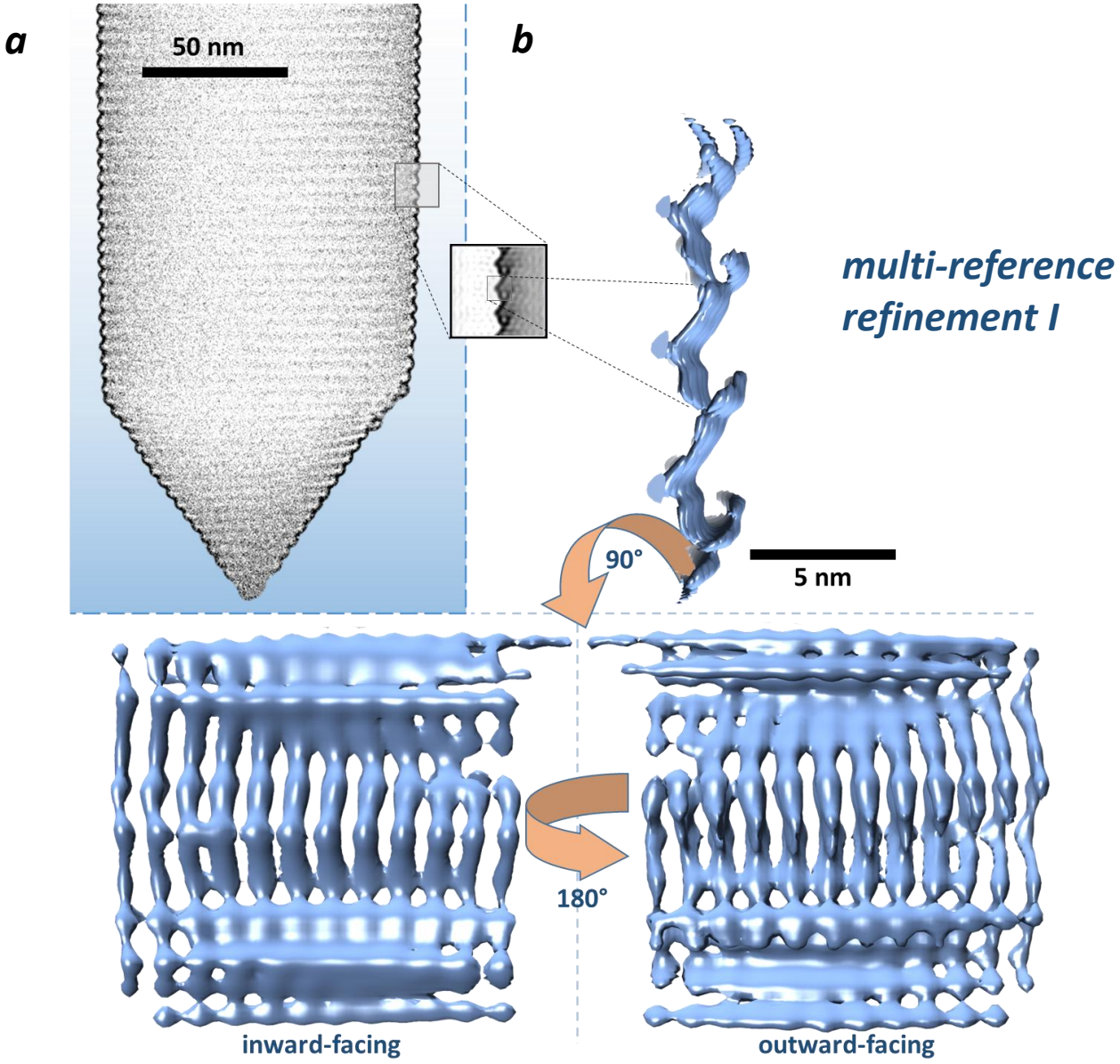

Figure 52. *Long-exposure micrograph of an I34M point mutant gas vesicle showing the extracted, fine-aligned and averaged particle projections in YZ-plane along the wall (a). Hook structures on the outside of the wall are clearly visible. After the first multi-reference classification, mass-adjusted isosurface renderings of the refined class average focusing on a single rib, show separate column-like subunits using UCSF Chimera [73]. These subunits of 0.7 × 4.3 nm run almost perpendicular to the helical pitch. The gaps in between measure around 0.7 nm. The inner surface consists of smooth, concave grooves. The outer surface possesses distinct hooks on each column.*

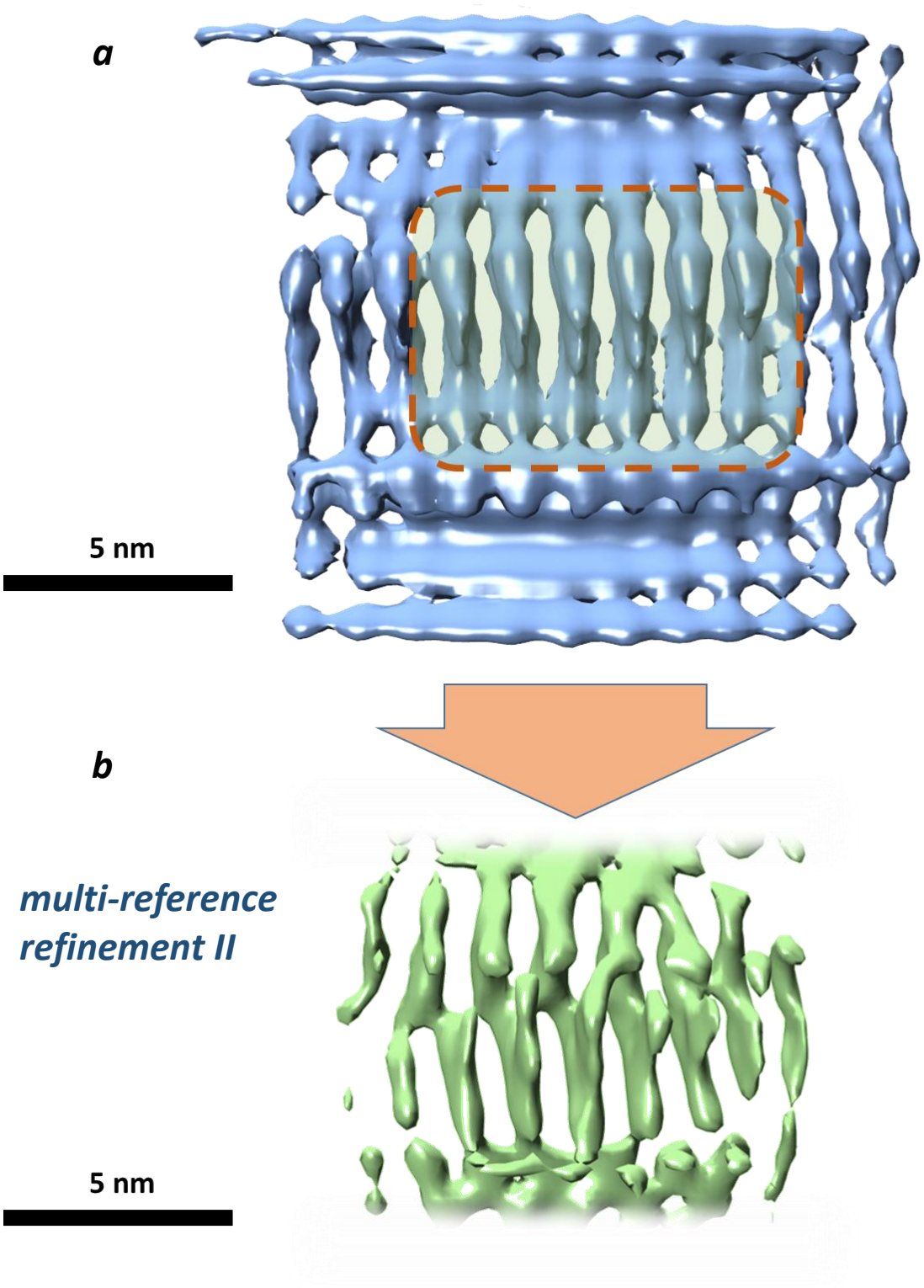

Figure 53. *Mass-adjusted isosurface renderings of first (a) and second (b) multi-reference refined classes in UCSF Chimera [73]. Further refinement, constrained to a cylindrical focus mask region (orange shape) revealed connecting densities between columns on the outward-facing surface, as seen below.*

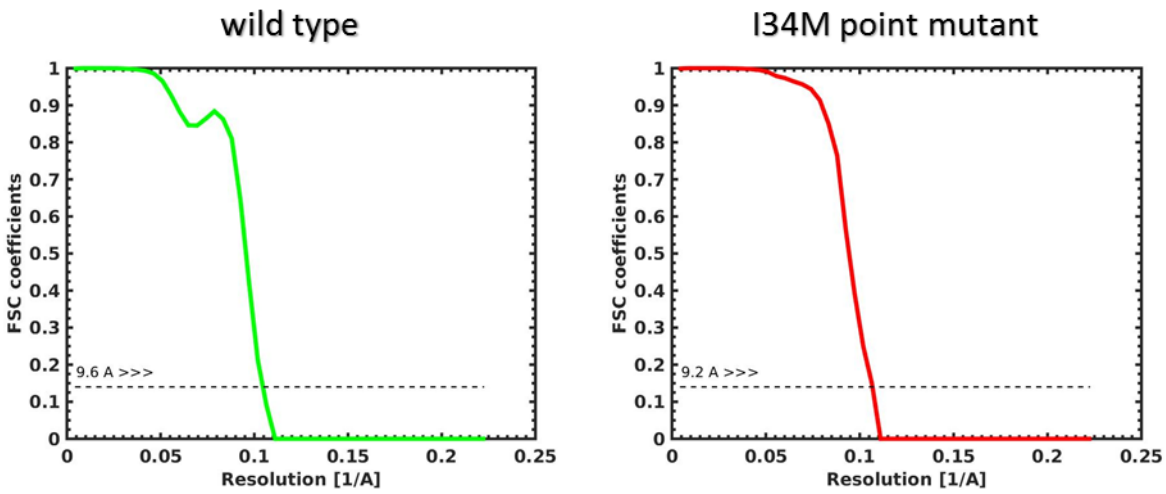

Figure 54. *Gold-standard fourier shell correlation (FSC) curves for the wild type (left, green) and I34M point mutant (right, red) gas vesicle subtomogram averages after their respective final multi-reference classification. The resolution criterion was FSC = 0.143, in accordance with [72].*

In shifting the focus mask by half a helical pitch in the direction of the column-like densities and combining the aligned focus regions, more than a single rib could be resolved (see *Figure 55*).

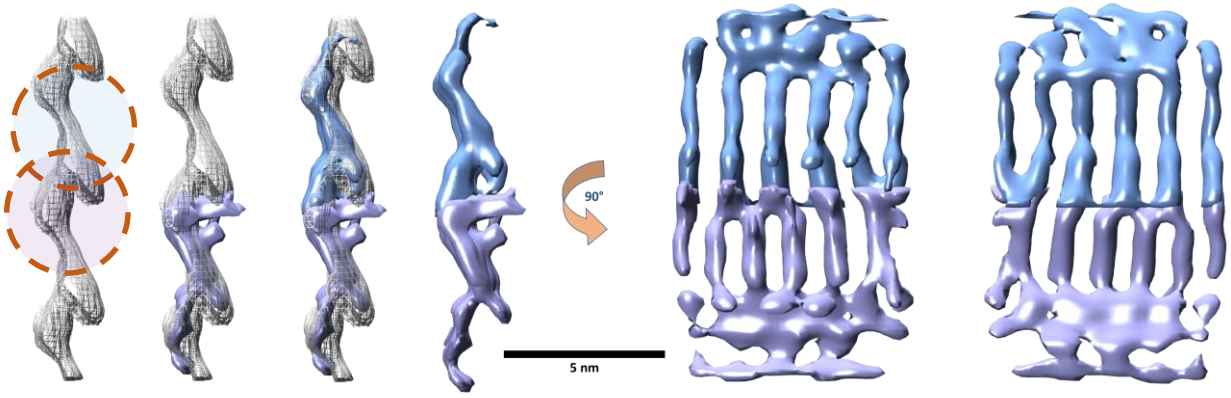

Figure 55. *Refinement and merging of two different focus masks (orange circles) for the final multi-reference classification: One focus mask was positioned between two gas vesicle ribs, resulting in the purple density, the other one was centered on one rib bulge and resolved the blue density. To assist with the alignment of the two structures, the average of the initially aligned subtomograms (grey mesh, see 4.3.6.3) was overlaid; overlapping densities were truncated at the rib-rib interface.*

In parallel, *Relion* 1.4 was used to compare and corroborate the previously determined electron densities by *TOM Toolbox [64, 74]*. The formerly generated coordinates list from the peak extraction

was input to *Relion* to perform an independent particle extraction and align, classify and refine the subtomogram structure via its 3D-classification functions. The program succeeded to resolve the outward-facing envelope regions with better accuracy, showing the backbone of columns possessed an outward-facing, tilted mesh of connecting densities, as shown in *Figure 56*. This was analogous to the densities resolved by *TOM Toolbox*.

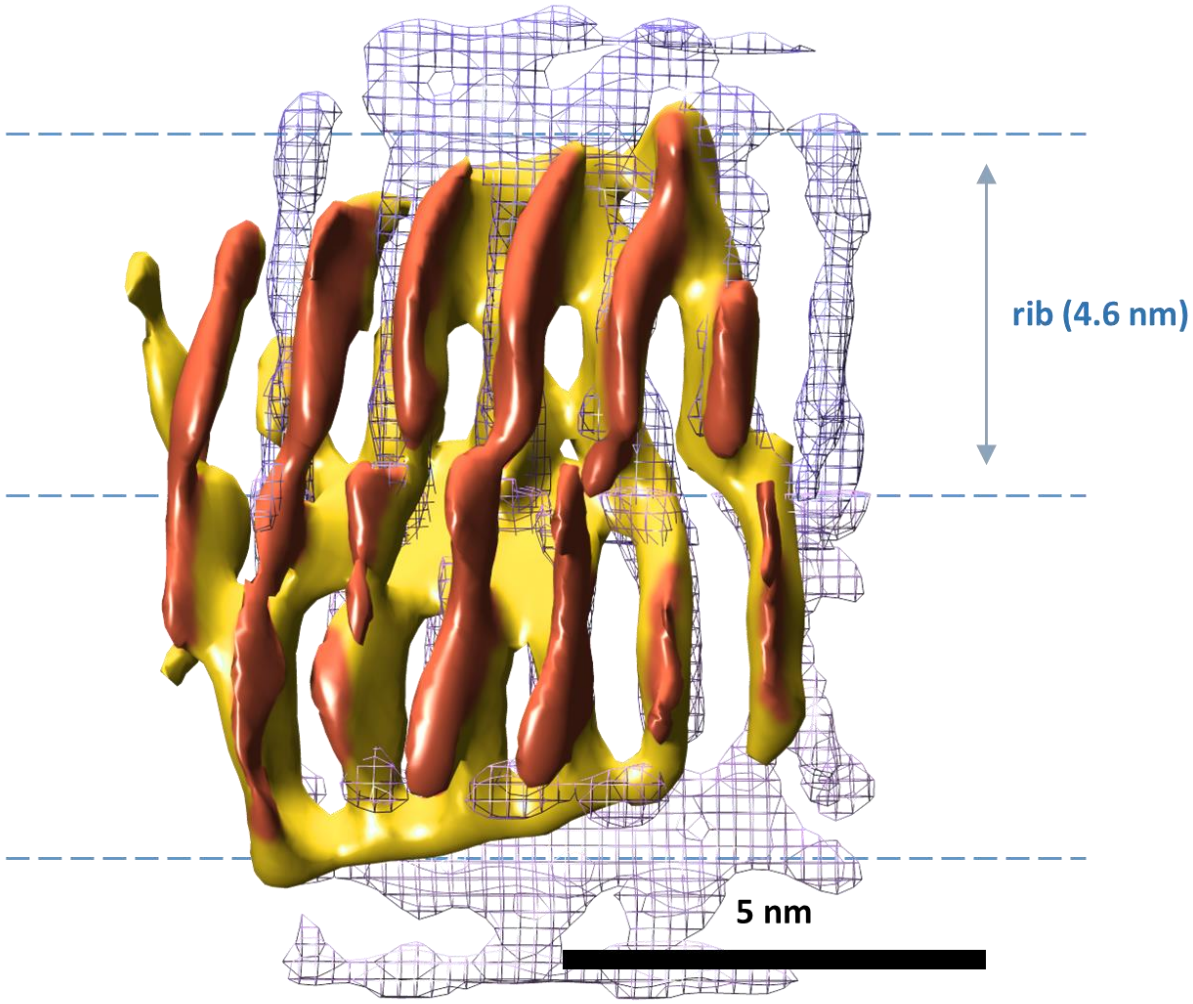

Figure 56. *Exterior-facing surface of the I34M point mutant gas vesicle envelope. The merged TOM toolbox-resolved densities (wireframe) and the Relion-refined structure (yellow and red) are overlayed. Relion was able to better resolve the outward-facing densities (red), that form a mesh of tilted connectors above the interior columns (yellow) [64].*

4.3.7. Docking models of GvpA

Due to the very low sequence similarity of GvpA to other sequenced proteins (see 2.1.2 and [33]), no homology models exist to serve as potential templates for a molecular docking approach with the resolved electron densities of this work. However, three principal model predictions currently exist for the molecular arrangement of GvpA proteins within the gas vesicle wall. All of them generally agree on the secondary folding motif of GvpA (see 2.1.2) and all of them orient the antiparallel hydrophobic β-strands to face the interior of the vesicle. However, the models differ in key points for the tertiary and quaternary structures. Sivertsen *et al*., as well as Bayro *et al*., suggested an amyloid arrangement of β-strands by inequivalent, antiparallel GvpA proteins [40, 75]. This model is based on a simulated air-water-interface and the existence of such an expansive cross-β-structure is supported by solid state NMR evidence of pressure-collapsed gas vesicles from the cyanobacterium *Anabaena flos-aquae*. In this model, neighboring GvpA subunits are tilted by 36° relative to the vesicle's principle axis. They are also slightly offset from one another and form asymmetrically, with the respective center of their β-turn alternating between two neighboring amino acids (see *Figure 57 a*). The positioning of the α-helices as interaction sites between subunits is not further investigated. Ezzeldin *et al*. conducted *ab initio* modeling to simulate the folding of GvpA from *Halobacterium salinarum*. They concluded that the quaternary structure of GvpA is likely arranged in antiparallel, slightly staggered pairs with nearly perpendicular β-strands for each subunit. The α-helices would face outwards and tilt towards neighboring dimers (see *Figure 57 b*).

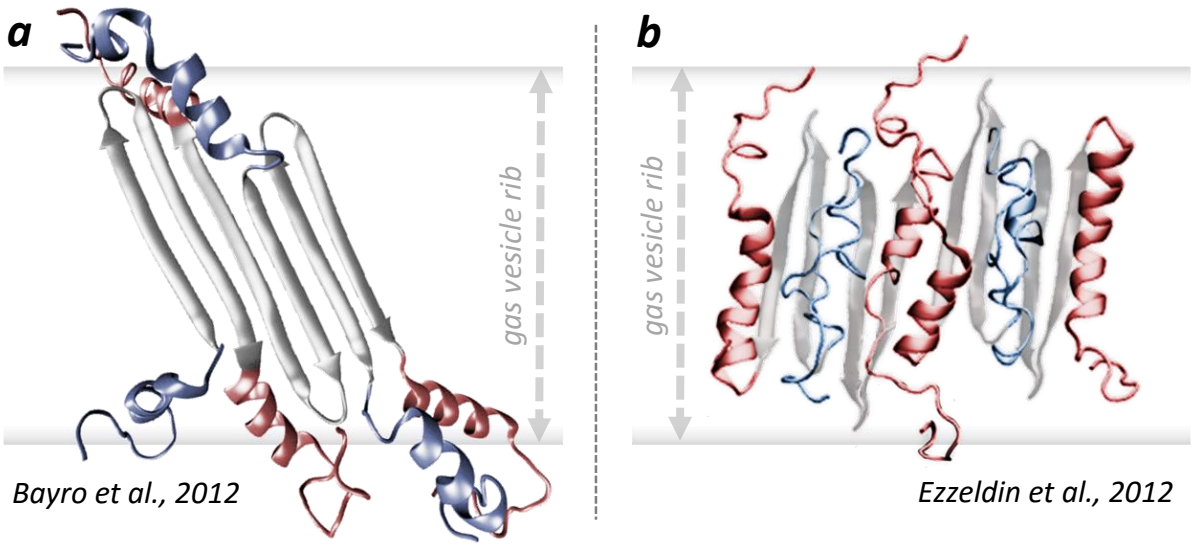

Figure 57. *Structural prediction models of GvpA by Bayro et al. (a) and Ezzeldin et al. (b). The N-terminal α-helix of each GvpA subunit is colored blue, the C-terminal α-helix is colored red. The first structure exhibits an extensive mesh of tilted amyloid fibrils, composed of inequivalent antiparallel dimers, and*

ignores quaternary folding of the α-helices. The latter shows the β-strands as perpendicular columns at the interior gas vesicle surface, made from antiparallel dimers which are covered by tilted α_2-helices that connect between subunits. Images modified from Bayro et al. [40] (a) and Ezzeldin et al. [45] (b).

Neither of these two anti-parallel cross-β-sheet models, however, can explain the observed permeability of the vesicle envelope to molecules much larger than water [36]. They also do not take the topology of the gas vesicle rib structure into account, as both suggest one row of staggered β-strands make up the 4.6 nm pitch, forming a flat surface of continuously repeating subunits. In contrast, Strunk *et al*. propose a model that accounts for the clearly visible zigzag pattern of the ribs, which contain concave and convex half-spaces [33]. Their *de novo* modeling approach is based on the primary sequence of GvpA from *Haloferax volcanii*, which is nearly identical to that of *Halobacterium salinarum*. Here, a symmetric, antiparallel, tilted dimer is presented as the repeating unit cell. Each dimer is tilted around 35° relative to the long axis of the gas vesicle and forms a hydrophobic concave interior cavity with its angled β-strands. This agrees very well with the observed density distribution in the resolved structure of the gas vesicle envelope by subtomogram analysis (see *Figure 58*).

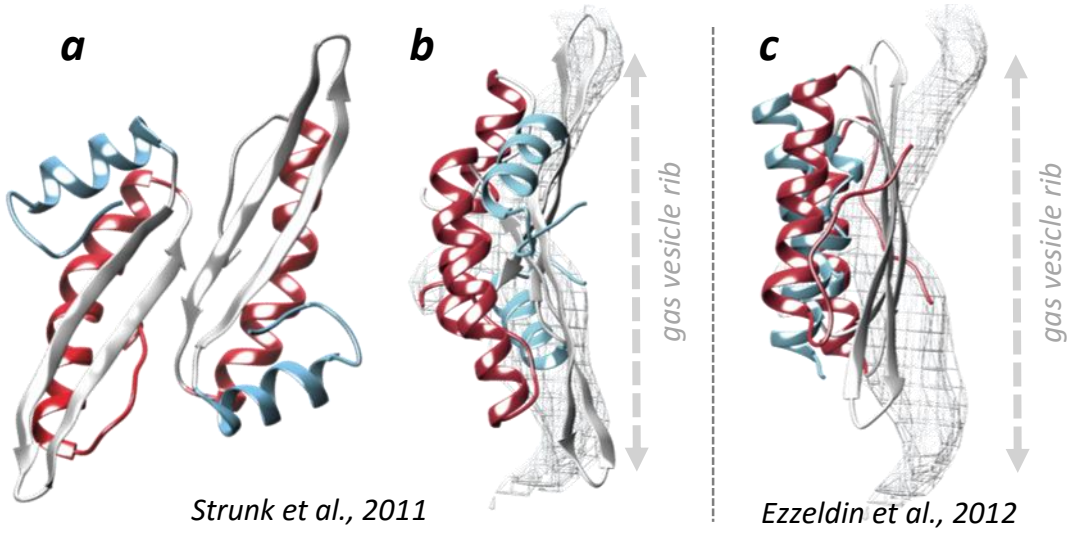

Figure 58. *GvpA dimer model by Strunk et al., in which two GvpA proteins are arranged antiparallel and slightly offset from each other (left side, a). Their α1-helices (blue) and α2-helices (red) stabilize and shield the hydrophobic interior from the exterior polar aqueous environment. The β-strands (grey) form a concave hydrophobic interior surface. If overlaid over the subtomogram analysis-resolved electron density map, the concave half-space fits very well as shown here in side view (b). By comparison, the proposed quaternary GvpA structure by Ezzeldin et al. does not feature any such bulges (c). Modified from Strunk et al. [33] (a and b) and Ezzeldin et al. [45] (c).*

As the GvpA model by Strunk *et al*. accounted for the rib topology and had the best overlap in a preliminary fitting attempt, it was used as a template for a molecular docking approach with the subtomogram analysis-resolved electron densities. Here, the monomeric subunits were shifted and rotated by hand and then fine-aligned via cross-correlation in *UCSF Chimera* [73]. Adjustments of the orientations of the α-helices were made to occupy densities in their direct vicinity. *Figure 59* shows the resulting docking model, in which two directionally opposed rows of GvpA monomers make up the helical rib. One row is slightly staggered and forms an overhanging density, corresponding to the observed hook, above the second row of subunits. All β-strands run nearly perpendicular to the principal vesicle axis and make up the highly regular column-shaped rib backbone. The concave interior surface of such a rib is exclusively made up of a hydrophobic network of anti-parallel β-strands which form separated columns. These columns are about 0.7 nm apart and would allow for the free diffusion of molecules to the interior space. Here, it is likely that nucleation of polar substances is prevented due to the smooth, extremely hydrophobic interior surface. The GvpA α-helices form an external hydrophilic mesh. Each subunit's C-terminal α_2-helix covers its β-strand, while the α_1-helix forms tilted connections between the ribs. Between the ribs the GvpA units interlock slightly, assuming a zip locker-like formation pattern. In this region, the N-terminal α_1-helix of each monomer tilts away and interacts with neighboring subunits along the rib-rib-interface, effectively fusing the ribs together. This is in agreement with the observed diagonal electron densities on the outward-facing side of the gas vesicle envelope previously shown in *Figure 53* and *Figure 54*, and is further illustrated in *Figure 60*.

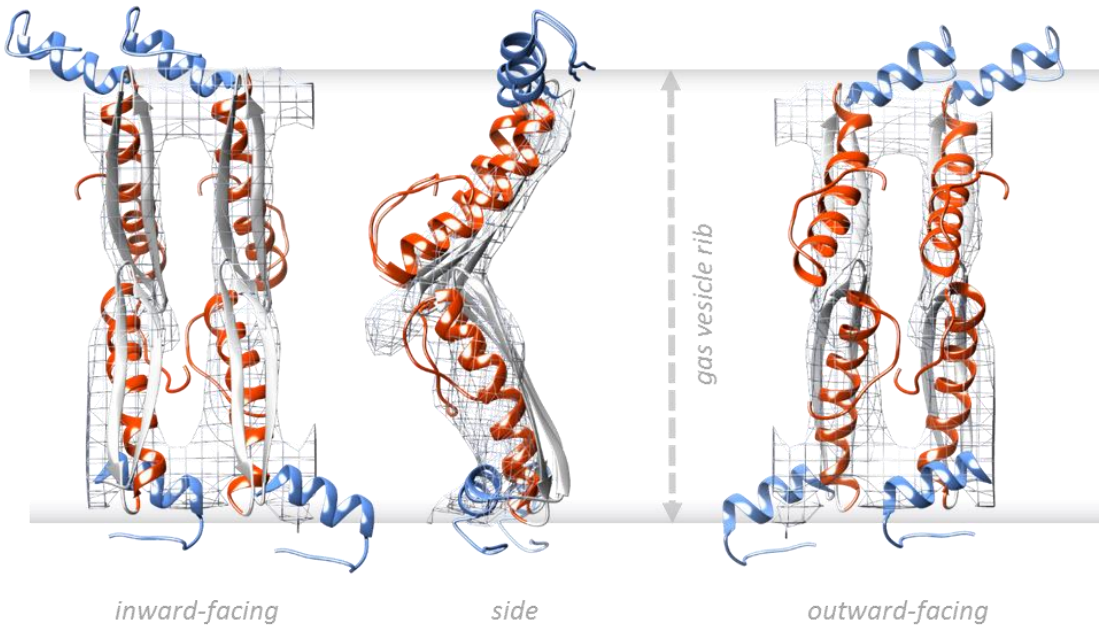

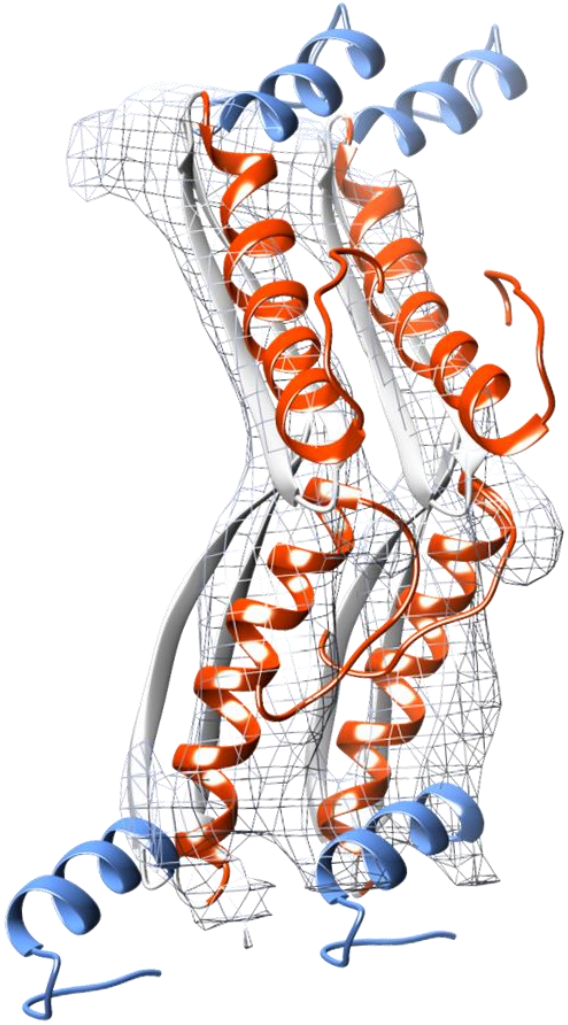

Figure 59. *Molecular docking approach of the proposed GvpA model by Strunk et al. into the electron density map resolved by subtomogram analysis. The ß-strands form regularly-spaced columns, approximately perpendicular to the rib's helical pitch, leaving larger gaps in between.*

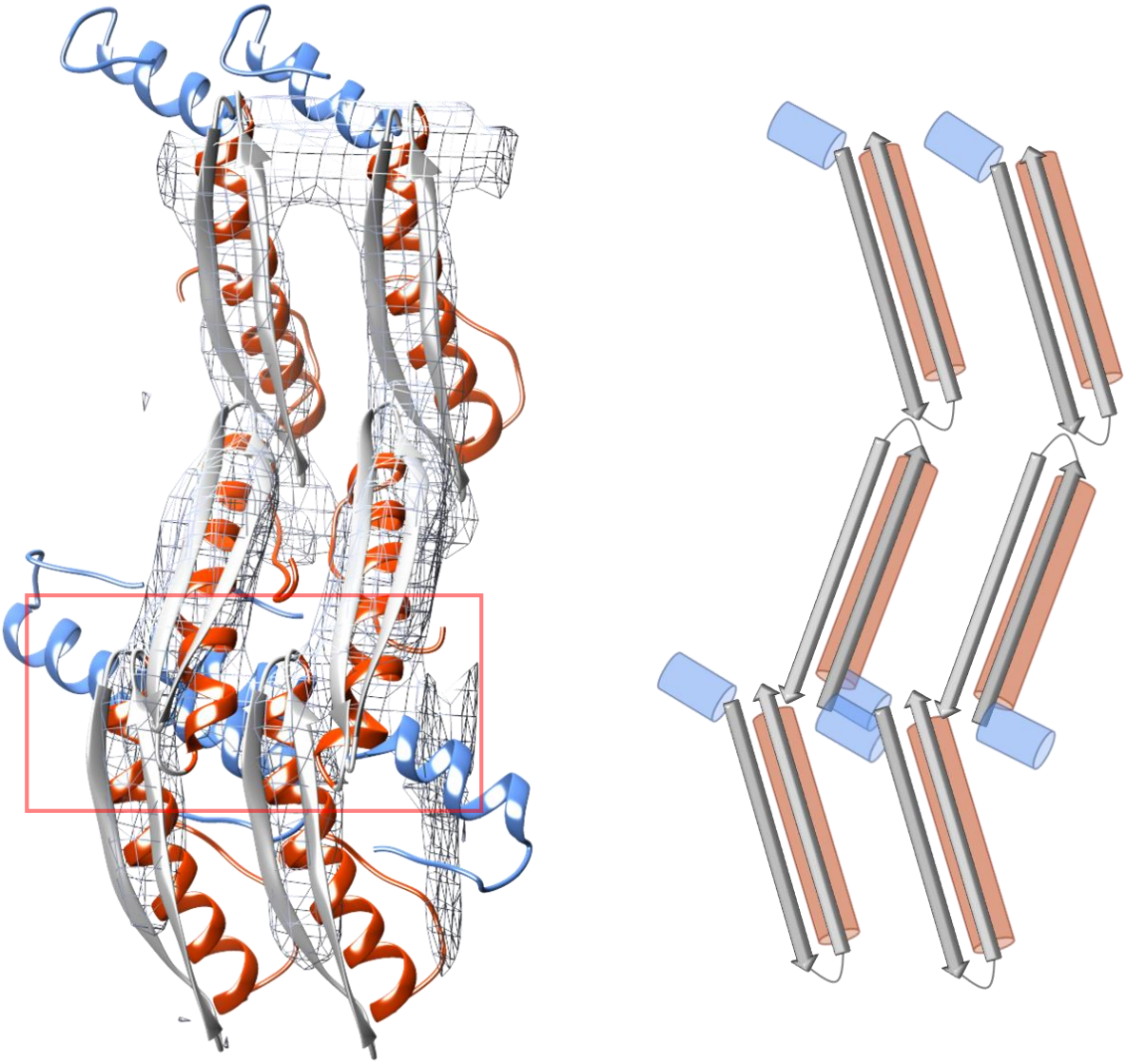

inward-facing *inward-facing (schematic)*

Figure 60. *Docking model with three rows of GvpA subunits over 1½ ribs (left side) and corresponding schematic illustration (right side). At the rib-interface (red box) the monomers are interlocking in a zip locker-like motif and the N-terminal α_1-helices (blue) form diagonal connections between subunits.*

5. Discussion

5.1. Cryo-electron tomography of cells under hypersaline sample conditions

The intracellular components of halophilic extremophiles such as *Halobacterium salinarum* were so far inaccessible to cryo-electron tomography in an *in vivo*-like state, due to the cells' dependence on high molar concentrations of salt. In order to counter the significant attenuation of contrast and SNR, state of the art imaging equipment was one prerequisite: CMOS-based direct electron detection and the Volta phase plate helped to decidedly boost image quality and allow for high resolution imaging with enhanced contrast and SNR at near focus levels. However, this alone would still be insufficient for full cell tomography of halophilic cells in close-to-native medium conditions. Therefore, several experimental sample optimization steps had to be undertaken, in order to strike a balance between hypersalinity and compatibility for transmission electron microscopy.

The most direct approach to increasing the SNR for TEM imaging was to lower the overall salt concentrations: A decrease of medium-solubilized NaCl would automatically incur a decrease of intracellular KCl (see 2.1), at the risk of inducing cell lysis. In light microscopic observations, *H. salinarum* seemed to immediately suffer damage and eventually lyse in salt concentrations lower than 2.5 – 2.0 M NaCl. However, transmission electron microscopy revealed deformations of the cells much earlier, at salt concentrations below 3.5 M NaCl. Morphological damage, caused by changes in osmotic pressure or through mechanical compression, usually showed at the pole regions first, evidently disintegrating the intricate intracellular polar cap structures. Salt tolerance observations made via cryo-EM are in agreement with the evaluation of growth curves of cell cultures raised in full liquid culture medium (FLCM) at different NaCl concentrations. Here, 3.5 M NaCl had a negligible effect on the doubling rate, whereas 3.0 M NaCl caused a slight drop in absolute cell density and cells would barely grow at all in 2.5 M NaCl. This finding is in good agreement with studies conducted by Zeng *et al*. [76]. Imaging of intracellular components at 3.5 M NaCl was still difficult. A gentle dialysis of cells grown in FLCM at these salt concentrations down to 3.0 M NaCl presented a feasible compromise: Those cells maintained their morphologically integrity for the duration of several hours, which was more than enough time to vitrify the sample.

Artificial selection for the most motile cells during swarm agar motility assays lead to a notable increase of bipolarly flagellated cells during the late exponential growth phase. This was a substantial step to increase the likelihood of finding flagellated cells in close alignment to the orientation of the tilt axis for tomographic recording.

The improvement of the vitrification procedure posed another essential prerequisite to achieve higher success rates at creating samples suitable for high salt cell tomography. Initially, manual sample

preparation was performed under a fume hood, without temperature or humidity control and lead to widely erratic results. Utilization of the *Vitrobot* held the advantage to exert systematic control over such environmental conditions, as well as specific blotting parameters. However, despite extensive attempts made to optimize the vitrification process, results remained inconsistent. The cell surface is covered with sulfated glycoproteins and exhibits extreme hydrophilicity. Inorganic salts increase the surface tension. At room temperature and atmospheric pressure, an aqueous solution of 3.0 M NaCl also exhibits a 34 % increase in viscosity compared to pure water [77]. As a consequence, arbitrarily forming local cell aggregations might temporarily retain the saline medium, which results in the observed erratic blotting behavior. Moreover, the *Vitrobot* did not allow for complete experimental consistency due to slight mechanical deviations caused by infrequent repairs and routine maintenance as a consequence of its multi-user setup. The sample vitrification step was identified as the bottleneck for the creation of high quality samples. Further and more extensive experimentation is required to achieve higher consistency and reproducibility of EM-grids that feature a mostly homogenous cell monolayer. Therefore, a wider variety of technically reproducible *Vitrobot* parameters should be screened, such as temperature and humidity conditions, as well as blotting strengths in combination with different sample drain times.

Finally, it was necessary to address the effects the natural thickness of the prokaryotes would bring. Ordinarily, a sample thickness of up to 500 nm is still deemed acceptable for high resolution imaging [78]. However, due to the hypersaline environment, and the intracellular accumulation of KCl within halobacteria in particular, it is desirable to fall well below this value, if possible. This presents a conundrum: On the one hand, the vitreous saline ice needed to be as thin as possible to allow imaging at acceptable SNR levels. On the other hand, ice thinner than 500 nm would compress the cells and disrupt the fragile intracellular polar cap structures. Here, FIB milling offered a solution by thinning a wide area of the grid post-vitrification, which would potentially contain flagellated, uncompressed cells towards the edge of the milled wedge pattern. These would be very suitable for high resolution tomography, in spite of high salt concentrations. However, the FIB milling procedure, while unavoidable, further reduced the throughput rate of high quality samples by the introduction of contamination and/or deformation of the copper grids during clipping and transfer in and out of the system. Contamination could often only be detected via subsequent TEM examination, making quality control time-consuming. This could simply be counteracted by an increased throughput of samples.

In conclusion, intracellular imaging of hypersaline samples becomes viable with the sample optimization steps described in this work, as demonstrated in chapters 4.1.4 and 4.1.5. While the low success rate for the creation of suitable samples hampered reliable structural imaging of halobacterial cell poles, an overall higher sample throughput would increase the probability to obtain the desired

cryo-electron tomography motif. Future successful imaging of the intracellular halobacterial motility apparatus will therefore be highly dependent on the optimization of the cell vitrification step.

5.2. IgY labeling of the flagellar growth site

Archaeal flagella and bacterial flagella are distinctly different [20]. Amongst other factors, they are morphologically set apart by their differing diameters. With around 10 nm, archaeal flagella are only half as thick as their bacterial counterparts [10]. Moreover, it has been shown that they lack an inner channel that would route flagellin building blocks to a distal growth site, which is the case in bacteria [12, 16]. However, no experiments for the precise localization of the flagellar growth site in archaea have so far been successfully conducted. The immunolabeling of halobacterial flagella described in this work constitutes a first approach for the detection of this region.

The main challenge consisted in the production of polyclonal anti-flagellin antibodies that could bind with sufficient affinity under hypersaline conditions. A substantial amount of antibodies had to be expended on ELISA binding screening tests. Therefore, IgY was the antibody of choice, as it can be isolated from chicken egg yolk in high concentrations [54]. The FITC-conjugated IgY antibodies bound to the halobacterial surface under native, hypersaline conditions in FLCM. Supporting cryo-EM imaging with gold marker-conjugated donkey-anti-IgY labeling antibodies suggested that flagella were also recognized. However, the emitted FITC signal from Fla-bound IgY must have been overshadowed by the much stronger fluorescence signal of the cell surface-bound antibodies. Due to this effect, the distinct labeling of the flagellar growth site was not possible. The high cross-reactivity of anti-Fla IgY with the cell surface is very likely an effect of the similarities in the glycosylation pattern between the halobacterial S-layer and the flagella [79, 80]. A more efficient approach to the localization of the halobacterial flagellar growth site would be to raise monoclonal antibodies, which specifically recognize epitopes exclusive to the flagellin surface.

A second difficulty arose through the inhibition of cell motility due to the relatively high molecular weight and size of the full-chain immunoglobulins [81] [82]. Under the light microscope, it was observed that the cells were severely encumbered and often completely immobilized by IgY. In order to reduce this effect, only the IgY Fab fragments should be used to repeat the FITC labeling assay. Fab fragments can be retrieved via papain digestion and subsequent purification of the fragments; detailed protocols by Porter [83] and Akita *et al.* [84] are available. Another alternative would be the use of single-domain antibody fragments (*Nanobodies*®), which are significantly lighter without compromising their specificity [85].

5.3. The structure of the gas vesicle and the molecular arrangement of GvpA

In general, the gas vesicle can be divided into three regions of defined structural regularity: The characteristic spindle tips, the cylindrical body regions with clear 4.6 nm helical rib pattern, and the middle seam section. Fourier-filtering reveals an attenuation of the 4.6 nm periodicity along the seam, indicating local structural inhomogeneity. Notably, subunits from one half of the vesicle cylinder are diametrically opposed to that of the other half. The distinct hooks of each subunit, as resolved by subtomogram analysis, are always facing the center seam section, while the overall helical handedness remains unchanged. This center seam might likely constitute the growth site of the gas vesicle. The overwhelming majority of the envelope exclusively consists of the small 8.3 kDa protein GvpA. Analyses of unwashed halobacterial wild type gas vesicles by LC-MS revealed an absorption peak for GvpA and a minor absorption peak of potential GvpC. Besides GvpC, which attaches to the outside of the envelope for structural support, so far no other proteins have been detected to play a structural role [34, 86]. However, two more proteins essential to gas vesicle morphogenesis, GvpJ and GvpM, do possess sequence similarities to the N-terminal α_1-helix of GvpA [28]. Point mutation studies on GvpA, conducted by Strunk *et al*., proved the importance of the small α-helix, and in 2012 Pfeifer surmised this to be the main interaction site between vesicle ribs [28, 33]. It is plausible that GvpJ and GvpM might play a structural role in the formation of at least sub-regions of the gas vesicle envelope, or act as initial polymerization components. However, mass spectrometry of solvated gas vesicles could not detect masses related to these two proteins, so if they do constitute envelope building blocks they are likely to appear in very low, sub-stoichiometric concentrations. In this context, a more detailed study of the areas around the middle seam section and the spindle tips is of particular interest. Here, local concentrations of so far unknown structural proteins could be responsible for the change in rib helicity and vesicle shape. One such approach would entail the localization of GvpA by cross-correlating a high resolution electron density map of the protein with these isolated regions. A similarity rating of GvpA-like densities could then potentially reveal any direct structural involvement of further Gvp proteins. A high resolution density map of GvpA was made available through the subtomogram analysis of regular gas vesicle cylinder sections in the context of this work.

The study of halobacterial gas vesicles' molecular structure by cryo-electron tomography was challenging primarily for two reasons: The extraordinarily low dose tolerance and the very small size of the monomeric subunit comprising its envelope.

The vesicle fine-structure started to visibly disintegrate at dose ranges of > 40 e/Å², less than half of the ordinarily applied dose for biological specimens [87]. It was previously observed by Bartesaghi *et al*., that the negatively charged amino acids Asp and Glu seem particularly sensitive to electron radiation [88]. The small N-terminal α-helix of GvpA is rich in Asp, while the longer C-terminal α-helix

features many Glu residues, presumably as part of the halobacterial proteome adaption to hypersaline conditions (see 2.1). These regions, likely responsible for creating the interconnecting mesh on the outward-facing side of the gas vesicle envelope, as shown in the molecular docking models (see 4.3.7), would therefore be particularly sensitive to electron irradiation. Another possibility for this phenomenon might be the accumulation of liquid oxygen, derived from air trapped inside the vesicle, at the time of vitrification. Walsby showed that vesicles usually contain environmental air, which ordinarily possesses a partial O_2 pressure of around 21 % [32]. With a boiling point of -183 °C, 13 degrees above that of N_2, molecular oxygen would condense earlier than nitrogen and adhere to the surface of the vesicle. Electron beam interactions could easily excite the O_2 molecules into singlet oxygen, superoxide, nascent oxygen or other reactive oxygen species (ROS). ROS would immediately react with either the proximal proteins of the gas vesicle envelope or their hydrate shells, thus destroying their pristine structural integrity directly or in a reaction cascade. To remedy this effect, gas exchange in isolated gas vesicles and subsequent vitrification of the sample would have to be performed under pure nitrogen atmosphere, which was not possible at the time. It would require the *Vitrobot* to be placed inside an anaerobic tent, which impedes necessary user operations, or a significant re-design of the machine, featuring a sealed vitrification chamber. The method of choice to address the gas vesicle radiation sensitivity was to limit electron-induced damage by recording tomograms at very low total dose ranges. Power spectra of the recorded dose series revealed attenuation of the third order diffractions of the repeating 4.6 nm gas vesicle rib pattern, at doses as low as ~ 30 e/Å². The third order diffraction corresponds to a resolution of around 1.5 nm and its total radiolysis-induced annihilation would therefore pose a major resolution-limiting constraint. However, the pattern persisted up to around 50 e/Å² and subtomogram averaging in combination with a classification method were thought to resolve additional beam-induced structural heterogeneity. Therefore, a compromise between electron dose and sufficient SNR was thought to have been met at total doses of around 30 – 35 e/Å² per tilt series. The utilization of the novel Volta phase plate in combination with a direct electron detector posed important prerequisites to generate sufficient contrast and SNR for each individual tilt.

The nanometer-scaled size of the monomeric subunit posed another challenge, which was addressed by subtomogram analysis and a strong focus on multi-reference alignment and classification. Subtomogram analysis revealed the ribs to consist of a row of columns running perpendicular to the principal rib axis. Each column measures 0.7 nm in diameter, which corresponds very well to the width of a GvpA monomer's predicted antiparallel β-strands [33, 40, 41, 45]. The columns assume a staggered formation at the rib-rib interface. Between columns, gaps of 0.7 nm account for the reportedly observed diffusion of larger molecules into the vesicle volume, such as the 0.63 nm large octafluorocyclobutane, as described by Walsby *et al*. [36]. Therefore, quite counterintuitively, the gas

vesicle does not resemble a sealed-off “balloon”, but rather a selectively permeable proteinaceous mesh. Molecules seem quite able to diffuse in and out; however, the vesicle interior is presumed to be extremely hydrophobic, offering no nucleation sites for polar liquids such as water.

Analysis of the wild type subtomograms displayed a greater degree of structural heterogeneity compared to the point mutant. While in both cases only apparently regular cylindrical vesicles were chosen for tomographic recording, the wild type vesicles frequently exhibited local deformations and were partially compressed. This can be attributed to the overall larger diameter of the vesicles in combination with the harsh blotting conditions before vitrification. The average diameter of all recorded wild type vesicles was measured to be 126 ± 18 nm, in comparison to the point mutant with 99 ± 19 nm. The deformation of the wild type vesicles and the added diversity of potentially disordered GvpC-bound wall segments might very well have contributed to a greater motif diversity in the subtomogram stack, which would have been difficult to resolve in distinct sub-classes. Subtomogram analysis therefore primarily focused on the I34M point mutant gas vesicle, which resulted in a high resolution electron density map of a small envelope patch at around 10 Å. These patches contained several GvpA building blocks and were either centered on a single rib, or focused on the rib-rib-interface, which served as a framework for a molecular docking approach.

Unambiguous molecular docking of GvpA is currently not possible for two reasons. On the one hand, secondary folding motifs, such as α-helical and β-strand regions, cannot be resolved at the current electron density map resolution. On the other hand, none of three existing computational predictions is able to provide a comprehensive model, which incorporated all so far observed experimentally determined characteristics of the gas vesicle. Nevertheless, comparisons with the established prediction models shed some light on the secondary and quaternary structural organization of GvpA. It is beyond any doubt that subunits must be arranged in a way that creates an amphiphilic envelope. The interior of this wall therefore must consist of a smooth surface of β-strands, while the exterior is shielded by a mesh of hydrophilic α-helixes. While the model by Bayro *et al*. ties together almost all so far observed properties of the molecular architecture of the gas vesicle, it does not account for the arrangement of α-helixes within the quaternary structure of GvpA. Furthermore, the continuous, flat cross-β-sheet cannot provide an explanation for the observed concave interior surface of the ribs nor the fact that even larger molecules are freely able to permeate the gas vesicle wall. Ezzeldin *et al*. propose a model that agrees well with the perpendicularity of the columns in the electron densities as presented in chapter 4.3.6.4. In addition, the outward-facing α-helices of this model would correspond to the diagonally connecting mesh at the external surface of the gas vesicle envelope. The alternating, antiparallel dimers create a dense mesh of anti-parallel β-sheets, and thus this proposal neglects the same observations as the aforementioned model. The prediction model created by Strunk *et al*. also portrays antiparallel, tilted GvpA dimers to form the vesicle helix. It is, however, the only approach to

also account for the three-dimensional bulging of the gas vesicle ribs [33]. Its tilted β-strands do not agree with the close to perpendicular electron densities, which were resolved by subtomogram analysis in this work. Nevertheless, they do form a distinct cavity for the interior rib half-space, which resulted in the best initial overlap with the obtained tomographic electron density.

In contrast, the highly regular spacing of the observed electron densities resolved in the subtomogram analysis of the gas vesicle wall make it difficult to support a strictly separated, antiparallel dimeric arrangement of GvpA distributed over separated columns. As shown in a molecular docking approach, these columns possibly consist of anti-parallel β-strands of two rows of individual GvpA proteins that are facing each other with their β-turns. They would thus create a sieve-like amphiphilic mesh that explains both, the topology of the ribs, as well as the prevention of water accumulation in the interior of the gas vesicle, as the interior would be highly hydrophobic and absent of polar nucleation sites (see *Figure 60*). In this case, the partial gas pressure of the surrounding liquid would automatically regulate the concentration of gas molecules within the vesicle body.

Between ribs, some multi-reference-refined classes showed tilted densities at the envelope exterior, diagonally connecting the column backbone. This is corroborated by the densities retrieved through an independent structural refinement approach via *Relion* 1.4 [64, 74]. These densities suggest the presence of extensive protein chain interactions on the outside of the gas vesicle envelope, formed by the hydrophilic α-helical parts of GvpA. Contrary to current models, the structural integrity of the gas vesicle might therefore not rest on extensive cross-β-sheet interactions, but rather interconnecting α-helices that fuse the ribs together. The long, C-terminal α_2-helix is primarily shielding the β-strands along one rib and enables the solubilization of the vesicle within the hypersaline cytosol of *H. salinarum*, according to its “salt-in” proteome adaption (see 2.1). The N-terminal α_1-helix is then responsible for the rib-rib interactions, linking subunits diagonally. Point mutant experiments conducted by Strunk *et al*., which emphasize the essential contribution of both GvpA α-helices to gas vesicle biosynthesis, strongly support this hypothesis. Even single point mutations in these regions frequently resulted in gas vesicle negative transformants [33]. Furthermore, the formed connection is tilted and might account for the diagonal connectors found between two ribs in the refined electron densities (compare *Figure 53* and *Figure 56* in chapter 4.3.6.4), as well as the 36° tilted structural elements observed in X-ray diffraction and AFM experiments [41, 42].

Lastly, in this model, the hook regions on the exterior surface of the gas vesicle (see *Figure 59*) are formed by one row of GvpA slightly overlapping the other row along a single rib. These hook structures could potentially serve as interaction sites for the structural support protein GvpC. However, the I34M point mutant vesicles did not contain any GvpC at all and no clear additional density could be observed at the outer wall of wild type vesicles so far. The molecular ratio of GvpC to GvpA is around 1:25, and

the overall molecular diameter of the larger GvpC is unknown [86]. In this context, a re-evaluation of the wild type subtomogram analysis with a much larger search template might potentially reveal the localization of GvpC along the vesicle envelope.

In conclusion, individual GvpA subunits could be resolved to around 10 Å by subtomogram analysis. With this, the probable quaternary structural arrangement of GvpA comprising the gas vesicle envelope could be further elucidated in a model docking approach. A hypothesis could be made as to why gas vesicles are particularly radiation sensitive, as well as able to retain gas and exclude polar liquids. However, the seemingly high structural variance in particular at the exterior surface of the vesicle wall prevented the obtainment of density maps at higher resolution. The unresolvable heterogeneity might be an effect of electron-induced damage to the fine structure or a naturally occurring flexibility of the outward-facing amino acid residues. In order to address this circumstance, a much larger dataset, recorded at even lower doses, would be required. The resulting large stack of subtomograms would be suitable to conduct a considerably more extensive multi-reference classification. In turn, this should reduce the amount of variance within single classes and better resolve the exact arrangement of the α-helical mesh along the envelope's outside surface. Resolutions of 6 – 4 Å would be required in order to accurately identify individual β-strands within one GvpA monomer, as well as α-helical loop regions. This would allow for a significantly more precise docking model. Finally, a subtomogram analysis-refined GvpA structure could serve as the template for further subtomogram analyses of both the conical vesicle tips and the center fault site. This should reveal the relative positioning of subunits within these regions, which is currently not known. Furthermore, the study of young spindle-shaped vesicles in an early growth stage by single particle or subtomogram analysis could yield high-resolution densities of the spindle tips and perhaps unveil first insights into the growth mechanism of the gas vesicle.

6. Acknowledgements

I owe my most profound gratitude to the people who have made my time at the Max Planck Institute a truly amazing experience; those who supported me with their advice, their wit, and their friendship.

First and foremost, I would like to thank my supervisor Harald Engelhardt for his excellent guidance throughout this project and the many inspiring discussions we shared. Without him this ambitious project could not have taken shape. Many thanks, of course, to Wolfgang Baumeister for allowing me to work in his department and providing a most impressive microscope infrastructure to work with. Thanks also to Jürgen Plitzko for very successfully managing, maintaining and expanding this infrastructure while always being enormously kind and helpful. I hereby promise to henceforth refrain from calling his cell phone at 2:30 AM.

Furthermore, my gratefulness goes to our collaborator Felicitas Pfeifer and her group at the Technical University of Darmstadt for the gas vesicle point mutant samples, as well as the very friendly and productive get-togethers we had. I also owe sincere gratitude and my utmost respect to Florian Beck. His dedication and hard work made the data processing for the gas vesicle subtomogram analysis possible. May his rich sociolect – cultivated over countless years, Ignaz – live on. My deepest thanks go to Miroslava Schaffer for her extraordinary support at the FIB, for great conversations, and for her friendship. Next time I will bring less recalcitrant samples, promised. Martin Lawrence I would like to thank for his advice and his friendship. He helped me to regain a clear head when I was lost in the details and gave me the occasional confidence boost when I needed it. To Radostin Danev I owe heartfelt thanks for being a mentor and, above all, a very good friend. I am looking forward to what the future will bring. Let us share many good debates on astronomy, gaming and politics. 頑張って！

Many thanks also to “my” interns, Paul Weyh, Alexandra Grigore, Raphael Roccor, Christoph Blossey and Phillip Daniel-Ivad, who supported me in this work and with whom I shared many insights and fruitful discussions. To Günter Pfeifer, Oana Mihalache I say thank you for their helpfulness, their kindness and for teaching me the practical basics of microscopy and TEM sample preparation. Thanks to Jan Lubieniecki for his aid with the laboratory work and the cell culturing when I was completely swamped. Thanks to Peter Herzig, who showed me the inner workings of the *Polara* and the *Titan*, was always around for a good conversation, and enthusiastic to provide help with all kinds of technical issues.

Special thanks to Inga Wolf for her assistance with any EDP-related issues and, above all, for frequently taking care of the department’s social matters (which bridge trolls like me all too often shamefully neglect!). Birgit Book I warmly thank for the outstanding support with all kinds of bureaucratic matters and her ceaseless help during my “crunch time” period.

Thanks to Iron Maiden *et al*. for accompanying my writing sessions with their magnificent music. \m/

Victoria Sanchez, Lissy Weyher, and Nagarjuna Nagaraj I thank for their support with the mass spectrometry analysis, their marvelous motivation, and their helpful advice.

Cheers, of course, to my friends and colleagues at the MPI, Sahradha Albert, Jan Arnold, Shoh Asano, Antje Aufderheide, Ben Engel, Yoshiyuki Fukuda, Thomas Hoffmann, Agnes Hubert, Maryam Khoshouei, Zdravko Kochovski, Tim and Ulrike Laugks, Ganesh Pathare, Stefan Pfeffer, Nikolas Schrod, Andreas Schweitzer, Pia Unverdorben, Marc Wehmer, Luca Zinzula, and so many more. They made my time here tremendously enjoyable; I wish them all the best for the future!

I wish to thank my parents, Claus and Petra, for their ceaseless support of my academic education and my brother Markus, who earned my admiration for his accomplishments long before this work was started. May his ambition and his skeletal joints last forever.

A wholehearted “Dankeschön” to Elisabeth and Wilhelm Werberger, my landlords, who provided me with a reinvigorating refuge; a place where I could study – and indulge myself in serene escapism.

Lastly, my thanks and my love to my wonderful wife, Camila. I still sometimes struggle to comprehend the likelihood of our relationship. You transformed me from a grumpy loner into a happy, confident introvert. You give me more strength than you imagine. It is my lifelong goal to make you happy.

7. References

[1] Dyall-Smith, M. (2009) The Halohandbook - Protocols for haloarchaeal genetics, http://www.haloarchaea.com/resources/halohandbook/index.html

[2] Ng, W. V., and Kennedy, S. P., and Mahairas, G. G., *et al.* (2000) Genome sequence of Halobacterium species NRC-1, *Proc Natl Acad Sci U S A 97* (22): 12176-12181.

[3] Oren, A. (1991) Anaerobic growth of halophilic archaeobacteria by reduction of fumarate, *Microbiology 137* (6): 1387-1390.

[4] Müller, J. A., and DasSarma, S. (2005) Genomic analysis of anaerobic respiration in the archaeon Halobacterium sp. strain NRC-1: dimethyl sulfoxide and trimethylamine N-oxide as terminal electron acceptors, *J Bacteriol 187* (5): 1659-1667.

[5] Ruepp, A., and Soppa, J. (1996) Fermentative arginine degradation in Halobacterium salinarium (formerly Halobacterium halobium): genes, gene products, and transcripts of the arcRACB gene cluster, *J Bacteriol 178* (16): 4942-4947.

[6] Galinski, E. A. (1993) Compatible solutes of halophilic eubacteria: molecular principles, water-solute interaction, stress protection, *Experientia 49* (6-7): 487-496.

[7] Eisenberg, H., and Mevarech, M., and Zaccai, G. (1992) Biochemical, structural, and molecular genetic aspects of halophilism, *Adv Protein Chem 43*: 1-62.

[8] Pfeifer, F. (2015) Haloarchaea and the formation of gas vesicles, *Life (Basel) 5* (1): 385-402.

[9] Wagner, G., and Hartmann, R., and Oesterhelt, D. (1978) Potassium uniport and ATP synthesis in Halobacterium halobium, *Eur J Biochem 89* (1): 169-179.

[10] Jarrell, K. F., and Bayley, D. P., and Kostyukova, A. S. (1996) The archaeal flagellum: a unique motility structure, *J Bacteriol 178* (17): 5057-5064.

[11] Ng, S. Y., and Chaban, B., and Jarrell, K. F. (2006) Archaeal flagella, bacterial flagella and type IV pili: a comparison of genes and posttranslational modifications, *J Mol Microbiol Biotechnol 11* (3-5): 167-191.

[12] Trachtenberg, S., and Cohen-Krausz, S. (2006) The archaeabacterial flagellar filament: a bacterial propeller with a pilus-like structure, *J Mol Microbiol Biotechnol 11* (3-5): 208-220.

[13] Alam, M., and Oesterhelt, D. (1984) Morphology, function and isolation of halobacterial flagella, *J Mol Biol 176* (4): 459-475.

[14] Wieland, F., and Paul, G., and Sumper, M. (1985) Halobacterial flagellins are sulfated glycoproteins, *J Biol Chem 260* (28): 15180-15185.

[15] Wieland, F. (1988) Structure and biosynthesis of prokaryotic glycoproteins, *Biochimie 70* (11): 1493-1504.

[16] Yonekura, K., and Maki-Yonekura, S., and Namba, K. (2003) Complete atomic model of the bacterial flagellar filament by electron cryomicroscopy, *Nature 424* (6949): 643-650.

[17] Faguy, D. M., and Koval, S. F., and Jarrell, K. F. (1994) Physical characterization of the flagella and flagellins from Methanospirillum hungatei, *J Bacteriol 176* (24): 7491-7498.

[18] Mattick, J. S. (2002) Type IV pili and twitching motility, *Annu Rev Microbiol 56*: 289-314.

[19] Streif, S., and Staudinger, W. F., and Marwan, W*., et al.* (2008) Flagellar rotation in the archaeon Halobacterium salinarum depends on ATP, *J Mol Biol 384* (1): 1-8.

[20] Albers, S. V., and Jarrell, K. F. (2015) The archaellum: how Archaea swim, *Front Microbiol 6*: 23.

[21] Marwan, W., and Alam, M., and Oesterhelt, D. (1991) Rotation and switching of the flagellar motor assembly in Halobacterium halobium, *J Bacteriol 173* (6): 1971-1977.

[22] Hildebrand, E., and Schimz, A. (1990) The lifetime of photosensory signals in Halobacterium halobium and its dependence on protein methylation, *Biochim Biophys Acta 1052* (1): 96-105.

[23] Schlesner, M., and Miller, A., and Streif, S*., et al.* (2009) Identification of Archaea-specific chemotaxis proteins which interact with the flagellar apparatus, *BMC Microbiol 9*: 56.

[24] Beznosov, S. N., and Piatibratov, M. G., and Fedorov, O. V. (2007) [Multicomponent nature of Halobacterium salinarum flagella], *Mikrobiologiia 76* (4): 494-501.

[25] Kalmokoff, M. L., and Jarrell, K. F., and Koval, S. F. (1988) Isolation of flagella from the archaebacterium Methanococcus voltae by phase separation with Triton X-114, *J Bacteriol 170* (4): 1752-1758.

[26] Kupper, J., and Marwan, W., and Typke, D*., et al.* (1994) The flagellar bundle of Halobacterium salinarium is inserted into a distinct polar cap structure, *J Bacteriol 176* (16): 5184-5187.

[27] Kireev, II, and Novikova, T. M., and Sheval, E. V*., et al.* (2006) [Structure of the intracellular part of the motility apparatus of halobacteria], *Mikrobiologiia 75* (3): 364-370.

[28] Pfeifer, F. (2012) Distribution, formation and regulation of gas vesicles, *Nat Rev Microbiol 10* (10): 705-715.

[29] Walsby, A. E. (1977) The Gas Vacuoles of Blue-Green Algae *Sci Am 237* (2): 90-97.

[30] Walker, J. E., and Hayes, P. K., and Gjerde, J*., et al.* (1984) Homology of Gas Vesicle Proteins in Cyanobacteria and Halobacteria, *Microbiology 130* (10): 2709-2715.

[31] Griffiths, A. E., and Walsby, A. E., and Hayes, P. K. (1992) The homologies of gas vesicle proteins, *J Gen Microbiol 138* (6): 1243-1250.

[32] Walsby, A. E. (1994) Gas vesicles, *Microbiol Rev 58* (1): 94-144.

[33] Strunk, T., and Hamacher, K., and Hoffgaard, F*., et al.* (2011) Structural model of the gas vesicle protein GvpA and analysis of GvpA mutants in vivo, *Mol Microbiol 81* (1): 56-68.

[34] Hayes, P. K., and Buchholz, B., and Walsby, A. E. (1992) Gas vesicles are strengthened by the outer-surface protein, GvpC, *Arch Microbiol 157* (3): 229-234.

[35] Dunton, P. G., and Mawby, W. J., and Shaw, V. A., *et al.* (2006) Analysis of tryptic digests indicates regions of GvpC that bind to gas vesicles of Anabaena flos-aquae, *Microbiology 152* (Pt 6): 1661-1669.

[36] Walsby, A. E. (1982) Permeability of Gas Vesicles to Perfluorocyclobutane, *Microbiology 128* (8): 1679-1684.

[37] Fanourgakis, G. S., and Xantheas, S. S. (2006) The bend angle of water in ice Ih and liquid water: The significance of implementing the nonlinear monomer dipole moment surface in classical interaction potentials, *J Chem Phys 124* (17): 174504.

[38] Maréchal, Y. (2007) *The Hydrogen Bond and the Water Molecule*, Elsevier, Amsterdam.

[39] Jones, D. D., and Jost, M. (1971) Characterization of the protein from gas-vacuole membranes of the blue-green alga, Microcystis aeruginosa, *Planta 100* (4): 277-287.

[40] Bayro, M. J., and Daviso, E., and Belenky, M., *et al.* (2012) An amyloid organelle, solid-state NMR evidence for cross-beta assembly of gas vesicles, *J Biol Chem 287* (5): 3479-3484.

[41] Blaurock, A. E., and Walsby, A. E. (1976) Crystalline structure of the gas vesicle wall from Anabaena flos-aquae, *J Mol Biol 105* (2): 183-199.

[42] McMaster, T. J., and Miles, M. J., and Walsby, A. E. (1996) Direct observation of protein secondary structure in gas vesicles by atomic force microscopy, *Biophys J 70* (5): 2432-2436.

[43] Belenky, M., and Meyers, R., and Herzfeld, J. (2004) Subunit structure of gas vesicles: a MALDI-TOF mass spectrometry study, *Biophys J 86* (1): 499-505.

[44] Jones, D. T. (1999) Protein secondary structure prediction based on position-specific scoring matrices, *J Mol Biol 292* (2): 195-202.

[45] Ezzeldin, H. M., and Klauda, J. B., and Solares, S. D. (2012) Modeling of the major gas vesicle protein, GvpA: from protein sequence to vesicle wall structure, *J Struct Biol 179* (1): 18-28.

[46] Fischer, H., and Polikarpov, I., and Craievich, A. F. (2004) Average protein density is a molecular-weight-dependent function, *Protein Sci 13* (10): 2825-2828.

[47] FEI. (2015) Falcon II Direct Electron Detector, http://www.fei.com/accessories/falcon-II/

[48] Danev, R., and Buijsse, B., and Khoshouei, M., *et al.* (2014) Volta potential phase plate for in-focus phase contrast transmission electron microscopy, *Proc Natl Acad Sci U S A 111* (44): 15635-15640.

[49] Fukuda, Y., and Laugks, U., and Lucic, V., *et al.* (2015) Electron cryotomography of vitrified cells with a Volta phase plate, *J Struct Biol 190* (2): 143-154.

[50] Cho, H.-J., and Hyun, J.-K., and Kim, J.-G., *et al.* (2013) Measurement of ice thickness on vitreous ice embedded cryo-EM grids: investigation of optimizing condition for visualizing macromolecules, *Journal of Analytical Science and Technology 4* (1): 7.

[51] Schaffer, M., and Engel, B. D., and Laugks, T., *et al.* (2015) Cryo-focused Ion Beam Sample Preparation for Imaging Vitreous Cells by Cryo-electron Tomography, *Bio-protocol 5* (17): e1575.

[52] Fukuda, Y., and Schrod, N., and Schaffer, M., *et al.* (2014) Coordinate transformation based cryo-correlative methods for electron tomography and focused ion beam milling, *Ultramicroscopy 143*: 15-23.

[53] Mastronarde, D. N. (2005) Automated electron microscope tomography using robust prediction of specimen movements, *J Struct Biol 152* (1): 36-51.

[54] Pauly, D., and Chacana, P. A., and Calzado, E. G., *et al.* (2011) IgY technology: extraction of chicken antibodies from egg yolk by polyethylene glycol (PEG) precipitation, *J Vis Exp* (51).

[55] Parker, C. E., and Mocanu, V., and Mocanu, M., *et al.* (2010) Mass Spectrometry for Post-Translational Modifications, In *Neuroproteomics* (Alzate, O., Ed.), Boca Raton (FL).

[56] Reinhold, B. B., and Reinhold, V. N. (1992) Electrospray ionization mass spectrometry: Deconvolution by an Entropy-Based algorithm, *J Am Soc Mass Spectrom 3* (3): 207-215.

[57] Nickell, S., and Förster, F., and Linaroudis, A., *et al.* (2005) TOM software toolbox: acquisition and analysis for electron tomography, *J Struct Biol 149* (3): 227-234.

[58] Frank, J. (1992) *Electron Tomography*, Springer US.

[59] Crowther, R. A., and DeRosier, D. J., and Klug, A. (1970) The Reconstruction of a Three-Dimensional Structure from Projections and its Application to Electron Microscopy, *Proc. R. Soc. Lond. A 317* (1530): 319-340.

[60] Kremer, J. R., and Mastronarde, D. N., and McIntosh, J. R. (1996) Computer visualization of three-dimensional image data using IMOD, *J Struct Biol 116* (1): 71-76.

[61] Förster, F., and Han, B. G., and Beck, M. (2010) Visual proteomics, *Methods Enzymol 483*: 215-243.

[62] Förster, F., and Medalia, O., and Zauberman, N., *et al.* (2005) Retrovirus envelope protein complex structure in situ studied by cryo-electron tomography, *Proc Natl Acad Sci U S A 102* (13): 4729-4734.

[63] Scheres, S. H., and Valle, M., and Nunez, R., *et al.* (2005) Maximum-likelihood multi-reference refinement for electron microscopy images, *J Mol Biol 348* (1): 139-149.

[64] Scheres, S. H. (2012) RELION: implementation of a Bayesian approach to cryo-EM structure determination, *J Struct Biol 180* (3): 519-530.

[65] Kessel, M., and Buhle, E. L., Jr., and Cohen, S., *et al.* (1988) The cell wall structure of a magnesium-dependent halobacterium, Halobacterium volcanii CD-2, from the Dead Sea, *J Ultrastruct Mol Struct Res 100* (1): 94-106.

[66] Eichler, J., and Abu-Qarn, M., and Konrad, Z.*, et al.* (2010) The Cell Envelopes of Haloarchaea: Staying in Shape in a World of Salt, In *Prokaryotic Cell Wall Compounds* (König, H., Claus, H., and Varma, A., Eds.), pp 253-270, Springer Berlin Heidelberg.

[67] Frottin, F., and Martinez, A., and Peynot, P.*, et al.* (2006) The proteomics of N-terminal methionine cleavage, *Mol Cell Proteomics 5* (12): 2336-2349.

[68] Offner, S., and Ziese, U., and Wanner, G.*, et al.* (1998) Structural characteristics of halobacterial gas vesicles, *Microbiology 144* (5): 1331-1342.

[69] Weyland, M., and Midgley, P. A. (2004) Electron tomography, *Materials Today 7* (12): 32-40.

[70] Bartesaghi, A., and Sprechmann, P., and Liu, J.*, et al.* (2008) Classification and 3D averaging with missing wedge correction in biological electron tomography, *J Struct Biol 162* (3): 436-450.

[71] Martinez-Sanchez, A., and Garcia, I., and Asano, S.*, et al.* (2014) Robust membrane detection based on tensor voting for electron tomography, *J Struct Biol 186* (1): 49-61.

[72] Scheres, S. H., and Chen, S. (2012) Prevention of overfitting in cryo-EM structure determination, *Nat Methods 9* (9): 853-854.

[73] Pettersen, E. F., and Goddard, T. D., and Huang, C. C.*, et al.* (2004) UCSF Chimera--a visualization system for exploratory research and analysis, *J Comput Chem 25* (13): 1605-1612.

[74] Scheres, S. H. (2012) A Bayesian view on cryo-EM structure determination, *J Mol Biol 415* (2): 406-418.

[75] Sivertsen, A. C., and Bayro, M. J., and Belenky, M.*, et al.* (2010) Solid-state NMR characterization of gas vesicle structure, *Biophys J 99* (6): 1932-1939.

[76] Zeng, C., and Zhu, J. C., and Liu, Y.*, et al.* (2006) Investigation of the influence of NaCl concentration on Halobacterium salinarum growth, *J Therm Anal Calorim 84* (3): 625-630.

[77] Kestin, J., and Khalifa, H. E., and Correia, R. J. (1981) Tables of the dynamic and kinematic viscosity of aqueous NaCl solutions in the temperature range 20–150 °C and the pressure range 0.1–35 MPa, *Journal of Physical and Chemical Reference Data 10* (1): 71-88.

[78] Baumeister, W. (2002) Electron tomography: towards visualizing the molecular organization of the cytoplasm, *Curr Opin Struct Biol 12* (5): 679-684.

[79] Sumper, M. (1987) Halobacterial glycoprotein biosynthesis, *Biochim Biophys Acta 906* (1): 69-79.

[80] Cohen-Krausz, S., and Trachtenberg, S. (2002) The structure of the archeabacterial flagellar filament of the extreme halophile Halobacterium salinarum R1M1 and its relation to eubacterial flagellar filaments and type IV pili, *J Mol Biol 321* (3): 383-395.

[81] Noll, F., and Lutsch, G., and Bielka, H. (1982) Structure of IgG and IgY molecules in ribosome-antibody complexes as studied by electron microscopy, *Immunol Lett 4* (3): 117-123.

[82] Sun, S., and Mo, W., and Ji, Y.*, et al.* (2001) Preparation and mass spectrometric study of egg yolk antibody (IgY) against rabies virus, *Rapid Commun Mass Spectrom 15* (9): 708-712.

[83] Porter, R. R. (1959) The hydrolysis of rabbit y-globulin and antibodies with crystalline papain, *Biochem J 73*: 119-126.

[84] Akita, E. M., and Nakai, S. (1993) Production and purification of Fab' fragments from chicken egg yolk immunoglobulin Y (IgY), *J Immunol Methods 162* (2): 155-164.

[85] Harmsen, M. M., and De Haard, H. J. (2007) Properties, production, and applications of camelid single-domain antibody fragments, *Appl Microbiol Biotechnol 77* (1): 13-22.

[86] Buchholz, B. E., and Hayes, P. K., and Walsby, A. E. (1993) The distribution of the outer gas vesicle protein, GvpC, on the Anabaena gas vesicle, and its ratio to GvpA, *J Gen Microbiol 139* (10): 2353-2363.

[87] Comolli, L. R., and Downing, K. H. (2005) Dose tolerance at helium and nitrogen temperatures for whole cell electron tomography, *J Struct Biol 152* (3): 149-156.

[88] Bartesaghi, A., and Matthies, D., and Banerjee, S.*, et al.* (2014) Structure of beta-galactosidase at 3.2-A resolution obtained by cryo-electron microscopy, *Proc Natl Acad Sci U S A 111* (32): 11709-11714.